UNDERSTANDING LOSSES IN HALIDE PEROVSKITE THIN FILMS

Front cover: wide-field photoluminescence experiment and unveiled $CH_3NH_3PbBr_3$ true grains with amorphous boundaries.
Back cover: Kikuchi patterns of $CH_3NH_3PbI_3$; a first successful step ever toward mapping the true grains (back cover).

Ph.D. thesis University of Amsterdam, Mei 2018
Understanding losses in halide perovskite thin films
Gede Widia Pratama Adhyaksa

ISBN 978-94-92323-20-0

A digital version of this thesis can be downloaded from http://www.amolf.nl.

UNDERSTANDING LOSSES IN HALIDE PEROVSKITE THIN FILMS

ACADEMISCH PROEFSCHRIFT

ter verkrijging van de graad van doctor
aan de Universiteit van Amsterdam
op gezag van de Rector Magnificus
prof. dr. K. I. J. Maex
ten overstaan van een door het college voor promoties
ingestelde commissie,
in het openbaar te verdedigen in de Agnietenkapel
op dinsdag 22 mei 2018, te 10:00 uur

door

Gede Widia Pratama Adhyaksa

geboren te Denpasar, Indonesië

Promotor:	prof. dr. E. C. Garnett	(Universiteit van Amsterdam)
Copromotor:	prof. dr. A. Polman	(Universiteit van Amsterdam)
Overige leden:	prof. dr. R. A. J. Janssen	(Technische Universiteit Eindhoven)
	prof. dr. L. J. A. Koster	(Rijksuniversiteit Groningen)
	prof. dr. M. S. Golden	(Universiteit van Amsterdam)
	prof. dr. W. C. Sinke	(Universiteit van Amsterdam)
	dr. R. M. Williams	(Universiteit van Amsterdam)

Faculteit der Natuurwetenschappen, Wiskunde en Informatica

The work described in this thesis is part of the research program of the
Nederlandse Organisatie voor Wetenschappelijk Onderzoek (NWO)
and is financially supported mainly by the
European Research Council (ERC) under the European Union's Seventh Framework
Programme (EP/2007-2013)/ERC Grant 337328 "NanoEnabledPV,
and partly by an Industrial Partnership Programme between FOM and Phillips, and
additionally by TKI Urban Energy, "COMPASS" Project (TEID215022).

This work was carried out at the
Center for Nanophotonics, AMOLF,
Science Park 104, 1098 XG Amsterdam, The Netherlands,
where a limited number of copies of this dissertation are available.

Contents

1

Introduction and General Principles

Advances in thin-film semiconductor technology will find applications in highly efficient and low-cost photovoltaics. Hybrid-halide perovskites have emerged over the unprecedented timeframe of the last 6 years as a promising class of materials for such applications. Most notably, their solar cells have achieved power conversion efficiencies above 20 % in the laboratory basis, even though many fundamental questions still remain unanswered. Therefore for the halide perovskite thin-films to have an impact beyond the laboratory requires a systematic understanding and eliminating sources of losses. This chapter starts with the most important properties of halide perovskite thin-films in comparison with other photovoltaic semiconductors as well as some unanswered questions regarding the properties. Next, we discuss material imperfections as the sources of losses, and describing the methodology used in this thesis to identify and eliminate those losses. Finally, we provide description and important findings in each chapter to outline the overall motivation covering this thesis.

1.1 Halide perovskite thin-films

The dramatic rise of halide perovskites in photovoltiacs has caught the attention of scientists across many fields, and the initial hype has been followed by investigation of perovksite's structural, optical, and electrical properties. Perovskites offer a combination of the characteristics of inorganic and organic semiconductors: the

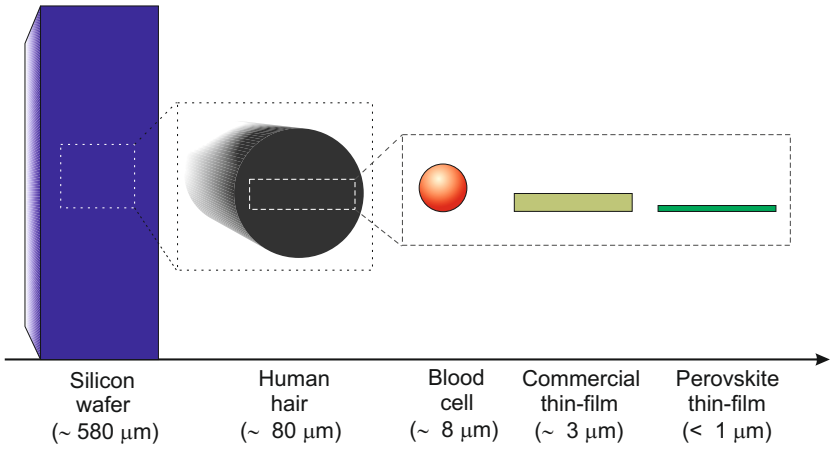

Figure 1.1: Schematic of cross-sectional scale (drawn to scale) of perovskite thin-films compared to other micron-scale relevant objects.

chemical tunability of their optoelectronics properties and low-temperature and solution-based deposition recall organics; their relatively high carrier mobility, diffusion length, and radiative lifetime more resemble those of polycrystalline semiconductors (**Table 1.1**). These attractive properties have inspired dreams well beyond photovoltaics, and research in sunlight-to-fuel conversion [1], light-emitting diodes (LED) [2, 3], lasers [4–6], photodetectors [7, 8], and recently thermochromics [9] is already underway.

Although rapid progress has been made, many fundamental aspects of halide perovskite materials still remain mysterious. Notable examples include the role of non-stoichiometric starting precursors (small fraction of chloride, acetate, or water content) in the formation of $CH_3NH_3PbI_3$, the origin of the electrical hysteresis seen in many solar cells, and the underlying reason for such high open-circuit voltages and slow recombination in thin-films containing a large density and diversity of defects (vacancies, chemical impurities, grain boundaries, unpassivated surfaces) that in most material systems would be considered of very low quality [10]. Also, because of their promise for large-scale applications such as photovoltaics, stability problems and degradation mechanisms must be well characterized. In these and other remaining puzzles, there is ample room for contributions from scientists and engineers with different backgrounds working in both experiment and theory. While many have chronicled the development of halide perovskite photovoltaic devices, this introduction focuses on the structure and deposition methods, before surveying their unique optical and electrical properties, noting areas that still require further investigation.

1.1.1 Crystal structures

The general formula of the perovskite crystal structure is ABX_3, in which A is the larger cation, B is the smaller cation, and X is the anion. In the most common hybrid-halide perovskites these are, respectively $CH_3NH_3^+$, Pb^{2+}, and a halide (I^-, Br^-, and Cl^-) or mixture of halides. The smaller B cations are octahedrally coordinated by X anions,

with the octahedra sharing corners in a three-dimensional (3D) lattice. The larger *A* cations fill the vacancies between the octahedra and have twelve X nearest neighbors. The possibilities for cation *A* and *B* are limited by the stability of the resulting structure, which can be estimated geometrically by the Goldschmidt tolerance factor and an octahedral factor introduced by Li [11]. Although these two parameters are quite successful in predicting the formation of a perovskite, predicting which distortions occur to the archetypical cubic structure is more difficult because these geometric factors do not account for ionic or covalent-bonding interactions, vibrational motion, or hydrogen bonding. These distortions reduce the symmetry of the lattice into a tetragonal or orthohombic space group, but the distorted perovskite retains the chemical formula and coordination numbers of the archetypical cubic structure.

To determine the structure and space group of perovskite experimentally, X-ray diffraction (XRD) is typically used, but it provides limited information. For example, in $CH_3NH_3PbI_3$, the position of the $CH_3NH_3{}^+$ is determined only indirectly by its effect on the inorganic portion of the crystal. Analyzing the position and orientation of this molecule within the 3D framework is important since alignment of the C-N dipoles is proposed to be the source of ferroelectricity in this materials. The rotational freedom imparts pseudo-spherical symmetry to the $CH_3NH_3{}^+$ which is necessary for a cubic structure [10].

1.1.2 Methods of deposition

One of the key benefits of perovskites is the apparent simplicity of their preparation; however, often a simple procedure belies complex thermodynamics and kinetics that give the material its unique morphology and properties. The $CH_3NH_3PbI_3$ perovskite thin-films have been produced primarly by precipitation from solution: the metal halide and organic halide are dissolved, and spin-coating followed by evaporation yields perovskite thin-films. Additionally, a combination of two-step processes in both solution and vapor phases have been explored as well as fully vapor-phase methods.

Common solvents include Lewis bases such as dimethylformamide (DMF), dimethylsulfoxide (DMSO), and gamma-butyrolactone. Little is known about the species present in solution, although solvents such as DMSO and DMF are known to coordinate to Pb^{2+} halide salts [12–14], and Pb^{2+} halide complexes are common in aqueous solutions of excess halide [15, 16]. The morphology of the resulting films produced from solution depends critically on the choice of solvent(s), the mode of their removal, and also on the substrate's morphology and surface chemistry [17–20, 22, 58]. For example, using DMSO in a mixture of solvents produces an intermediate phase after spincoating that then crystallizes into the perovskite film upon annealing [19]. Addition of a hydrohalic acid into the precursor solution has offered some improvement in the film morphology, but the underlying reason remains unclear [20, 22, 23, 58].

In order to gain better control over the deposition of $CH_3NH_3PbI_3$, a two-step solution process was developed and has in general produced solar cells with higher efficiencies than the single-step process [24], which could be due to the film's different carrier type and doping concentration. In this approach, either PbI_2 or $PbCl_2$ is

dissolved in DMF, spincoated onto a substrate, and then dried into a film. This film is then either dipped into an alcoholic solution of excess CH_3NH_3I alone or a CH_3NH_3I - CH_3NH_3Cl mixture [24, 25] or spincoated repeatedly with such a solution to convert the lead-halide film into the perovskite [26]. When such a process is applied to $PbCl_2$, $CH_3NH_3PbI_3$ is formed, presumably because according to the theory of hard and soft acids and bases [27] the softer, more polarizable I^- has much greater affinity for Pb^{2+} than the much harder Cl^-. As this approach requires diffusion of the $CH_3NH_3{}^+$ cations into the lead-halide matrix, it is possible that there is a thickness limitation on the films formed by this approach or higher temperatures or longer times are required to produce thicker films [28].

Vapor-phase methods produce halide-perovskites with different morphology and crystal structure. Co-evaporation of $PbCl_2$ and CH_3NH_3I in a vacuum deposition chamber yields highly uniform $CH_3NH_3PbI_3$ films with excellent photovoltaic characteristics [30]. The evaporation rates of the precursors determine the composition of the resulting perovskite, and the $CH_3NH_3PbI_3$ produced was confirmed to be cubic rather than the usual tetragonal phase that exists at room temperature.

Table 1.1: Comparison between $CH_3NH_3PbI_3$-based perovskites and other photovoltaic technologies. Perovskites have many of the advantages of polycrystalline semiconductors such as CIGS and CdTe, but they are processed from solution-like organic materials or quantum dots. Material characteristics refer to values measured for materials similar to those used in the highest performing solar cells. This table is adapted from [10] with updated number of column 2; the efficiency[29].

Photovoltaic technology	Power conversion efficiency (%) †	Absorption coefficient (cm^{-1}) ‡	Diffusion length (μm) ♭	Carrier mobility (cm^2/V.s) ♭	Carrier lifetime ♭
c-Si	26.7	10^2	100 - 300	10 - 10^3	4 ms
GaAs (thin-film)	28.8	10^4	1 - 5	>10^3	50 ns
CIGS	22.6	10^3 - 10^4	0.3 - 0.9	10 - 10^2	250 ns
CdTe	21.5	10^3	0.4 - 1.6	10	20 ns
Organic	12.1	10^3 - 10^5	0.005 - 0.01	10^{-5} - 10^{-4}	10-100 μs
Quantum dot	13.4	10^2 - 10^3	0.08 - 0.2	10^{-4} - 10^{-2}	30 μs
Perovskite	22.7	10^3 - 10^4	0.1 - 1.9	2 - 66	270 ns

† under AM1.5 (100 mW/cm^2)
‡ at 300 K in the vicinity of the band edge
♭ of the minority carrier (c-Si, GaAs, CIGS, CdTe, Perovskite) or the mobility of the exciton (Organic, Quantum dot)

1.1.3 Optical properties

Understanding the optical response of halide perovskite thin-films is crucial for optoelectronic applications such as photovoltaics, but it can also provide insight into the electronic and chemical structure.

Although tuning the band gap of perovskites is well documented, a more detailed understanding of these materials's optical properties awaits further research. For instance, dielectric constants in the ultraviolet, visible, and near-IR regions are critical to understanding the optical response of perovskites and also to calculating their absorption and emission properties when incorporated into optoelectronic devices. Progress in this area has been hindered by the difficulty of producing continuous films of sufficient smoothness [31] to avoid measurement artifacts from spectroscopic measurements of reflectance, transmittance, and ellipsometry. Film characterization using ellipsometry usually accounts for remaining surface roughness via modeling to produce the most reliable optical constants possible remains to be independently confirmed. Quantitative absorption coefficients have been determined from the absorption of $CH_3NH_3PbI_3$ on quartz [32], and glass [5], yielding values of 10^4 cm^{-1} near the band edge, but no detailed data of the film's morphology has been provided and no corrections for the surface's inhomogeneity have been applied; consequently, the reported values are only preliminary, but they are consistent with the absorption coefficients calculated based on the optical constants of $CH_3NH_3PbI_3$ [35]. Additionally, the absorption spectrum of $CH_3NH_3PbI_3$ when it is deposited within a mesoscopic template differs from that of perovskite deposited on planar substrates, which has been attributed to changes in the crystallite morphology that affect the optical transition. Band structure calculations indicate that this change in morphology affects the dipole screening of the excitonic transition [36]. Such differences further complicate accurate determination of the absorption coefficient and other optical parameters of perovskite films, so control over the materials properties of perovskites is of the greatest importance for characterization and applications.

The role of excitons in perovskites has been a topic of considerable debate. Recent studies indicate, however, that no significant population of excitons is present in photovoltaics made from $CH_3NH_3PbI_3$, whose excition-binding energy has generally been reported between 20 and 50 meV and is therefore comparable with the thermal energy at room temperature (k_bT = 26 meV) [37, 38]. Although the population of excitons is small in photovoltaics and remains small even at the higher excitation densities required for stimulated emission [38], the excitonic transition significantly enhances the absorption of hybrid perovskites near the band edge; consequently, the electronic band gap taking this into account is 1.65 eV for $CH_3NH_3PbI_3$. The density of excitons and associated effects should be greater in perovskites with higher band gaps, such as $CH_3NH_3PbBr_3$, whose binding energy has been estimated to be between 15 to 40 meV [39, 40].

Photoluminescence (PL) has been observed in perovskites of pure and mixed compositions. PL efficiency depends strongly upon pump fluence. At low excitation intensities, trapping of photogenerated charges competes effectively with direct

radiative recombination of electrons and holes, reducing luminescence [41]. As the excitation increases, these traps are filled and radiative electron-hole recombination dominates. In this regime, studies have confirmed low trap-induced recombination and two-body recombination dynamics over a range of pump intensities [42, 43]. At higher pumping, the PL efficiency falls as Auger recombination becomes more competitive at the higher carrier densities [31, 32, 38]. PL lifetime measurements have been reported for $CH_3NH_3PbI_3$ and $CH_3NH_3PbI_{3-x}Cl_x$, with longer lifetimes exhibited by the latter (3 to 18 ns *versus* 91 to 341 ns). In general, it is difficult to compare lifetimes directly unless they are measured at the same pump fluence, and the wide range of reported lifetimes for each material is likely due to a combination of varying excitation density and synthetic procedures. For solution-processed polycrystalline semiconductors, such lifetimes are surprising especially considering that essentially nothing has been done to reduce recombination at surface or grain boundaries. Considering that the perovskites exhibit clear self-absorption in their PL [38] and lasing spectra [32], it is not surprising that photon recycling has been reported to play an important role in their excited state dynamics when pathways of non-radiative decay are adequetely suppressed [33, 34].

1.1.4 Electrical properties

For solution-processed semiconductors with domain sizes below a few micrometers, halide perovskites exhibit unprecedented carrier transport properties that enable their stellar performance in photovoltaics. Quantitatively characterizing this transport, understanding the materials properties that give rise to it, and developing ways to improve it are all key directions for research.

The intrinsic electrical properties, such as carrier type, concentration, mobility, and diffusion lengths in halide perovskites have exhibited a large range of values often influenced by the method used to prepare the films. Additionally, the lack of smooth and uniform films on which to perform measurements can make the determination of intrinsic electrical properties challenging since conventional techniques often assume the sample exhibits a specific geometry. The carrier type is typically measured using thermoelectric measurement of the Seebeck coefficient, Hall measurement of the conductivity's response to an applied magnetic field, or thin-film transistor's response to a gating electric field. The Seebeck, Hall, and early resistivity measurements on polycrystalline $CH_3NH_3PbI_3$ indicated n-type conductivity, a carrier concentration of $\sim 10^9$ cm^{-3}, and an electron mobility of 66 cm^2/V.s [44]. From Hall measurements, the electron mobility for n-type films deposited from stoichiometric precursors was determined to be 3.9 cm^2/V.s [45] which is in accord with the 8 cm^2/V.s measured using terahertz spectroscopy [46], a technique that usually provides an upper limit because it neglects long-range carrier scattering [45]; however, it is not surprising that the mobility depends strongly on the preparation of the film.

The electron mobility of polycrystalline $CH_3NH_3PbI_3$ films compares favorably to that of films of other materials used as absorbers in solar cells. It is larger than the thin-film mobility of polymers (10^{-7} to 1 cm^2/V.s) [47, 48] and colloidal quantum dots (10^{-3} to 1 cm^2/V.s) [49] and it is comparable with that of CdTe (10 cm^2/V.s) [50],

CIGS and Cu_2ZnSnS_4 (CZTS) (10 to 100 cm^2/V.s) [51, 52] and polycrystalline Si (40 cm^2/V.s) [53]. Even in polycrystalline form, hybrid perovskites's inexpensive processing and tolerance to defects offer a significant advantage over conventional semiconductors.

As is the case for other polycrystalline semiconductors, electrical properties in hybrid perovskites are likely correlated with the film morphology. For instance, the dark and light conductivities of $CH_3NH_3PbI_{3-x}Cl_x$ deposited on a planar scaffold or on mesostructured aluminum oxide are quite different [56]. This difference has been attributed to an increase in the perovskite Fermi level in the mesostructured scaffold either through more surface iodide vacancies or through electrostatic gating from the aluminum oxide. Also, the role of grain boundaries in conduction through perovskite films has not been thoroughly explored, although passivation of grain boundaries with PbI_2 has been correlated to increased radiative lifetimes [57]. Inspired by the literature on organic solar cells, solvent annealing has been applied to $CH_3NH_3PbI_3$ solar cells to increase the grain size of the films to ~1 μm [58]. Such processing results in an increase in the photovoltaic performance and radiative lifetime.

1.2 Sources of losses

Generally, materials with a simple processability, such as halide perovskites, would pose a non-negligible level of defects at temperatures relevant for solar cell applications. However, halide perovskite thin-films are considered tolerant to defects [59, 60], relative to conventional semiconductors, and their solar power-conversion-efficiencies already exceed 20 % [61]. Nevertheless, defects still remain one of the critical issues that underpin limitations for further progress of approaching maximum attainable performance. Therefore, with improved engineering methods to control defects, the solar cell power-conversion-efficiencies can be expected to continue approaching the Shockley-Queisser limit [62]. Although theoretical studies of defects have proven useful, experimental confirmation of these results remains paramount. One main obstacle is the inability to identify and decouple the sources of losses. The well-known sources of losses are due to (1) impurities (point defects) and dislocation (line defects) in the bulk, (2) surface imperfections at the front- and back-surfaces, and (3) grain boundaries; all contribute in parallel to the total recombination process of halide-perovskite thin-films [63]. Precise identification of the bulk, surface, and grain boundary effects can help close the gap between our current understanding of defects and their implications for optoelectronic properties, and devices.

1.2.1 Bulk recombination

The bulk recombination occurs via point and line defects. Point defects include vacancy, interstitial, anti-site substitution, Frenkel defect (vacancy and interstitial co-exist at the same ion), and Schottky defect (cation and anion vacancies). While line defects form from dislocation of propagation point defects. These defects are

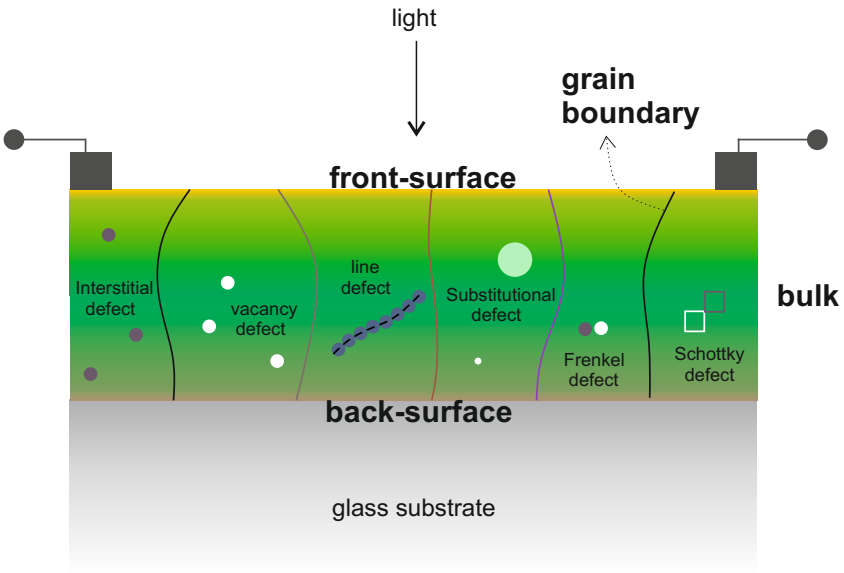

Figure 1.2: Basic topological imperfections showing the source of losses in halide perovskite thin-film: bulk, surfaces, and grain boundary. Each contains different characteristics and types of defects (illustrated by the colors).

thermodynamically favourable within the halide perovskites when their formation energies are negative [59, 60, 63]. Since the formation energies depend on atomic and chemical arrangements of the materials, they can vary under different growth conditions. A high-purity bulk (contains only a few parts per millions of impurities) is typically limited to a high temperature and slow grown process, such as the Czochralski method for monocrystalline silicon [64]. Bulk defects can contribute to several unusual phenomena in halide perovskites, such as ionic migration associated with the device electrical hysteresis [10].

1.2.2 Surface recombination

Interfaces consist of various dangling bonds at terraces, kinks, steps, vacancies, and ad-atoms where all non-radiative recombination can take place [65]. These interfaces can occur between the halide perovskite and air (surface), the substrate, another dielectric layer or with a contact layer. Surface and interface quality often has major implications on final device characteristics (particularly the open-circuit voltage and external quantum-yield). Surface recombination velocity is the standard metric used to assess the electronic quality of the front- and back-surfaces in semiconductors [66]. This recombination increases proportionally to the charge density at the interfaces. In a standard device configuration where the incoming light comes from the top, the highest charge generation rate and therefore highest recombination takes place at the front surface. There are two general strategies to minimize surface recombination: (1) reducing the surface state density, and (2) reducing the minority carrier density at the

surface. The first strategy relies on chemical passivation, for instance, by using an appropriate heterojunction [67], while the second one relies on field effect passivation, created for example by heavily doping the surface [54].

1.2.3 Grain boundary recombination

A misorientation between crystal planes creates a grain boundary. This can occur during a fast crystallization process [68]. Any segregation across the grain boundary induces excess free energy which is used to equilibrate the mechanical strains of the planar defect. In other words, the more grain boundaries, the higher mobility toward deformation [69–71]. Abnormal grain growth can occur if there is a large variation in grain boundary mobility and interfacial energy. Thermodynamic principles allow us to predict the grain boundary energies based on their crystallographic misorientation angles. At low angle, the energy enhances proportionally with misorientation, but then strongly depends on population numbers of the misorientation angles [72]. Although the driving forces for forming grain boundaries are similar to those of bulk and surface defects, the implications can be slightly different. For example, there is no fixed charge at the crystalline grain boundaries, therefore the band bending is solely governed by charges at the interface that can be compensated at much lower injection levels [73]. This leads to a higher recombination rate compared that of the front- or back-surface, where fixed charges can reside in the adjacent dielectric layers [74]. Halide perovskite thin-films contain a large grain boundary density. In conventional semiconductors, such as crystalline silicon, grain boundaries create deep-level defect states that reduce carrier lifetime and mobility. On the other hand, the role of grain boundaries in halide perovskite materials remains unclear, with conflicting reports suggesting they are detrimental, unimportant, or even beneficial [75, 76]. A technique that can be suitably used to identify the grain boundaries in halide perovskites will open a great avenue to engineer numerous types of grain boundaries and understand their correlation with optical and electrical properties.

1.3 Methodology for identifying losses

Bulk, surface, and grain boundary defects occur in all thin-film semiconductors. However, differentiating the losses contributed from each mechanism is not straight forward. This requires complete characterization of the materials system and the ability to independently vary the density of each defect. Experimental results are quite often deceiving, given the sensitivity of halide perovskites to a wide variety of stimuli used in standard characterization techniques (electron/ion beams, laser, electric fields) as well as environmental conditions (humidity, temperature, oxygen). This makes careful and highly controlled experiments that can measure materials properties accurately and reproducibly very important. These material properties then can be used as reliable inputs for modelling and simulations. The methodology used in this thesis attempts to improve our understanding, while pointing the way forward to eliminate the losses, and

finally utilizing this knowledge to design even better performing devices. **Figure 1.3** shows a development cycle of understanding the losses for thin-film halide perovskites.

1.3.1 Modelling can tell everything about solar cells

Solar cells consist of multilayer stacked structures (generally). The losses can be identifed from the interface, contact, and bulk properties. Standard methods use first optical simulations taking into account interference between different layers, or using ray optics if combined with wafer based system such as for perovskite-silicon tandem cells. From optical simulations allow for thickness and geometry optimization to minimize parasitic absorption and reflectance losses: all are useful information for device fabrication. The generation rate obtained from the optical simulation can be used for input into the electrical simulation to solve the drift-diffusion equation in which solar cell performance can be predicted. The system becomes more complex when grain boundaries are considered, as the transport becomes a 3D problem. Grating or nanostructured embedded contacts can add additional complications that require full 3D modelling. Nevertheless, a sufficiently sophisticated model can tell us everything we need to know about the solar cells. Quite often modelling provides useful insights into counterintuitive experimental observations. This is a very important feedback loop to carefully design a clean system for measurements.

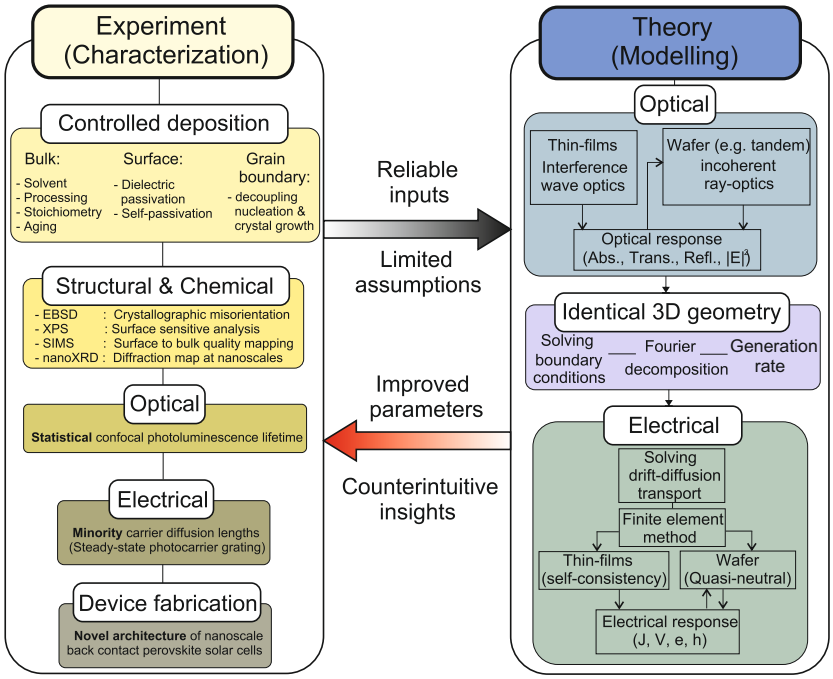

Figure 1.3: The development cycle tool combining experiment and theory to understanding losses in halide perovskite thin-films.

1.3.2 Results are only as accurate as the input and assumptions

The first step to ensure the accuracy from the modelling results is to use appropriate optical constants. One should be aware of the actual condition of the sample from which the optical constant is obtained. For example, very rough surface film could strongly perturb the measured refractive index due to light depolarization during the ellipsometry measurement. Therefore one should implement separetely an effective medium approximation to account for such effects in the input for optical modelling or use smooth films where this is not a problem. For the electrical modelling, it is very important to limit the assumptions being made. In order to extract out the recombination constants from the bulk, surface, and grain boundary, we developed a numerical solution to solve the three-dimensional transport equation using Fourier space. This makes fitting experimental data more efficient, which would otherwise be impossible using computer codes based on a finite element method. The boundary conditions obtained from the Fourier decomposition method can be implemented in our fullly coupled optical-electrical modelling. Instead of modelling a standard device used in the lab, we start by benchmarking our routine for a novel architecture device, such as nanoscale back-contact perovskite-silicon tandem. We considered the most ideal and realistic inputs possible to predict what novel design can beat the current standard device architecture.

1.3.3 What are required for reliable inputs ?

All outputs from the modelling should be aimed to help us understand the experimental results, toward reaching the best possible material and device properties. This process becomes meaningful when inputs obtained from the experiments are reliable. We developed two general strategies approaching that purpose: (1) controlled and clean systems, and (2) careful measurements.

Controlled and clean systems

Unlike silicon semiconductor technology with complex processing but simple structure, halide perovskites display relatively complex chemistry and rich physics given their simple solution deposition. Therefore we develop thin-film deposition protocols to have control over the bulk, surface, and grain size characteristics. Among those the most notable protocol is the deposition method to control grain size without affecting much the bulk and surface quality. This can be achieved by decoupling the nucleation and crystal growth steps. The nucleation is controlled during the spin-coating process from a saturated stock solution. The nucleation sites can stay for extended periods of time, unless heat treatment is applied, at which point crystal growth takes place. The final grain size is inversely proportional to the density of nucleation sites; a lower nucleation density yields larger grains. The density of nucleation sites is controlled by the spin-coating time with fixed spin-speed; longer time yields higher nucleation density. We continuously document our observation, optimize it, and assess the compatibility and limitation of our method. Even if we are able to control the grain size, this still does

not guarantee a perfectly clean system; we observe one peculiar case where amorphous grain boundaries showing unusual optical properties form at a particular spin speed. This makes careful characterization critically important as well.

Careful measurements

The various types of characterization techniques used to understand the sources of losses in halide-perovskite thin films should be directed toward the following considerations: (1) what are the limitations of the techniques? (2) are common artifacts and discrepancies routinely addressed? (3) to what extent are the materials tolerant to external perturbation, e.g electron beam-dose, light-soaking, applied voltage (4) what are the actual conditions, settings, and assumptions governing the chosen characterization techniques? and (5) are well-known principles developed for other semiconductors rigorously applicable for the materials under study here? Addressing all such issues simultaneously can be challenging especially at an early stage, so instead of debate, practice should be taken to advance our understanding toward more solid conclusions.

In order to carefully identify the sources of losses, in this thesis there are two notable routine techniques that we used, namely steady-state photocarrier grating (SSPG), and electron back-scattered diffraction (EBSD). These two methods have already been known in the past to study silicon based thin-films, and now have been successfully used perhaps for the first time in halide perovskite thin-films. SSPG is used to directly quantify the minority carrier diffusion length - one of the properties most strongly correlated with optoelectronic device performance. EBSD is used to identify crystalographic misorientation - therefore grain boundaries - whose effect remains poorly understood in the community. For each utilized technique we systematically report their limitations, important artifacts, methods for analysis corrections, and all possible ambiguous deductions or conclusions. In this way, we hope to streamline progress in the community toward rigorous conclusions about the properties of these exciting new optoelectronic materials and their perspectives for high-performance devices.

1.4 Outline of this thesis

This thesis is aimed to improve our limited understanding of losses in the bulk, on the surface, and at the grain boundaries of halide perovskite semiconductor materials, and top point the way forward to even better performance using novel design. Controlled, clean experimental systems along with careful measurement and full optoelectronic modelling/theory are used as a developing cycle tool to verify, and quantify the losses in halide perovskite thin-films. By quantifying and considering all of the losses, the ultimate goal is directed at designing a novel architecture device that potentially exceeds the performance and relaxes the limitation of traditional solar cell configurations.

In **Chapter 2**, we measure minority carrier diffusion length - a key parameter for

solar cell performance - of halide perovskite thin-films. We describe how controlled processing, composition, aging, and surface passivation correlate to the measured diffusion lengths. We find in pure $CH_3NH_3PbI_3$, the diffusion length is largely dependent on the controlled processing conditions. Next, we partially replace iodide (I) with bromide (Br) and find that surprisingly, the diffusion length increases after aging for 1 month in air. Finally, we use a 4-nm Al_2O_3 passivation layer on the top surface of $CH_3NH_3PbBr_3$, leading to a remarkable increase in diffusion length from 201 nm to 532 nm. The correlation that we have established between basic parameter space and diffusion length offers guidance in how to improve material properties.

In **Chapter 3**, we identify and characterize the grain boundary - an important aspect which is often misidentified - of halide perovskite thin-films. The biggest limiting factor is that a gold standard technique - electron backscattered diffraction (EBSD) - destroys halide perovskite thin films. Therefore identifying the grain boundaries using non-crystallographic techniques is deceiving, leading to conflicting literature reports about their influence. We solve this problem using a solid-state EBSD detector with 6,000 times higher sensitivity than the traditional phosphor screen and camera. We model the characteristics of grain boundary interface energy in $CH_3NH_3PbBr_3$ thin-films, and show that the halide-perovskite grains contain no special boundaries, such as crystal twinning. In addition, we find a peculiar case, where the grain boundary very likely consists of amorphous regions.

In **Chapter 4**, we correlate the information from **Chapter 3** to measure and model the effect of grain size on halide perovskite thin-films - a major challenge in understanding perovskite semiconductors. Correlating true grain size with PL lifetime, carrier diffusion length and mobility, shows that grain boundaries are not benign as is often claimed, but have a recombination velocity of 1670 cm/s, comparable to that of crystalline silicon. However, as with silicon, amorphous perovskite can passivate crystalline boundaries, leading to brighter photoluminescence and longer carrier lifetime without reducing diffusion length. This variable grain boundary character explains the mysteriously long lifetime and record efficiency achieved in small grain halide perovskite thin films, while pointing the way forward to even better performance.

In **Chapter 5**, we use our understanding of the losses to design a novel device architecture - nanoscale back-contact perovskite solar cell to improve tandem efficiency. Using coupled optical-electrical modelling, we optimize this architecture for a planar perovskite-silicon tandem, highlighting the roles of nanoscale contacts to reduce the required perovskite electronic quality such as minority carrier diffusion length. We discuss the advances of our design over the traditionally used two- (2-T) and four-terminal tandem (4-T), and point the way towards further improvements enabled by our design such as surface texturing, surface passivation and photoluminescence outcoupling.

Chapter 1 is partly based upon [10], while **Chapter 2**, and **Chapter 5** are based upon [77], and [78], respectively. Full details are listed at the end of this thesis (Scientific portfolio).

References

[1] J. Luo, J-H. Im, M. T. Mayer, M. Schreier, M. K. Nazeeruddin, N. G. Park, S. D. Tilley, H. J. Fan, and M. K. Grätzel, *Water photolysis at 12.3 % efficiency via perovskite photovoltaics and earth-abundant catalysts*, Science **353**, 1593 (2014).

[2] Z. K. Tan, R. S. Moghaddam, M. L. Lai, P. Docampo, R. Higler, F. Deschler, M. Price, A. Sadhanala, L. M. Pazos, D. Credgington, F. Hanusch, T. Bein, H. J. Snaith, and R. H. Friend, *Bright light-emitting diodes based on organometal halide perovskite*, Nature Nanotech. **9**, 1687 (2014).

[3] Y. H. Kim, H. Cho, J. H. Heo, T. S. Kim, N. Myoung, C-L. Lee, S. H. Im, and T. W. Lee, *Multicolored organic-ionorganic hybrid perovskite light-emitting diodes*, Adv.Mater. **27**, 1248 (2014).

[4] F. Deschler, M. Price, S. Pathak, L. E. Klintberg, D. Jarausch, R. Higler, S. Hu, T. Leijtens, S. D. Stranks, H. J. Snaith, M. Atatu, R. T. Phillips, and R. H. Friend, *High photoluminescence efficiency and optically pumped lasing in solution-processed mixed halide perovskite semiconductors*, J. Phys. Chem. Lett. **5**, 1421 (2014).

[5] B. R. Sutherland, S. Hoogland, M. M. Adachi, C. T. O. Wong, E. H. Sargent, and S. E. T. Al, *Conformal organohalide perovskites enable lasing on spherical resonators*, ACS Nano. **8**, 10947 (2014).

[6] Q. Zhang, S. T. Ha, X. Liu, T. C. Sum, and Q. Xiong, *Room-temperature near-infrared high-q perovskite whispering-gallery planar nanolasers*, Nano Lett. **14**, 5995 (2014).

[7] Y. Lee, J. Kwon, E. Hwang, C-H. Ra, W. J. Yoo, J-H. Ahn, J. H. Park, and J. H. Cho, *High-performance perovskite-graphene hybrid photodetector*, Adv. Mater. **27**, 41 (2014).

[8] L. Dou, Y. M. Yang, J. You, Z. Hong, W-H. Chang, G. Li, and Y. Yang, *Solution-processed hybrid perovskite photodetectors with high detectivity*, Nature Comm. **5**, 5404 (2014).

[9] J. Lin, M. Lai, L. Dou, C. S. Kley, H. Chen, F. Peng, J. Sun, D. Lu, S. A. Hawks, C. Xie, F. Cui, A. P. Alivisatos, D. T. Limmer, and P. Yang, *Thermochromic halide perovskite solar cells*, Nature Mat. **5**, 1476 (2018).

[10] S. Brittman, G. W. P. Adhyaksa, and E. C. Garnett *The expending world of hybrid perovskites: materials properties and emerging applications*, MRS Comm. **3**, 7 (2015).

[11] C. Li, X. Lu, W. Ding, L. Feng, Y. Gao, and Z. Guo *Formability of ABX_3 (X = F, Cl, Br, I) halide perovskites*, Acta Crystallogr. B **64**, 702 (2008).

[12] I. Wharf, T. Gramstad, R. Makhija, and M. Onyszchuk *Synthesis and vibrational spectra of some lead(II) halide adducts with O-, S-, and N-donor atom ligands*, Can. J. Chem. **54**, 3430 (1976).

[13] R. J. Alvarado, J. M. Rosenberg, A. Andreu, J. C. Bryan, W-Z. Chen, T. Ren, and K. Kavallieratos *Structural insights into the coordination and extraction of Pb(II) by disulfonamide ligands derived from o-phenylenediamine*, Inorg. Chem. **44**, 7951 (2005).

[14] I. Persson, K. Lyczko, D. Lundberg, L. Eriksson, and A. Paczek *Coordination chemistry study of hydrated and solvated lead(II) ions in solution and solid state*, Inorg. Chem. **50**, 1058 (2011).

[15] G. P. Haight and J. R. Peterson*Chloro complexes of lead(II)*, Inorg. Chem. **4**, 1073 (1965).

[16] H. L. Clever and F. J. Johnston*The solubility of some sparingly soluble lead salts: an evaluation of the solubility in water and aqueous electrolyte solution*, J. Phys. Chem. Ref. Data **9**, 751 (1980).

[17] D. B. Mitzi*Solution-processed inorganic semiconductors*, J. Mater. Chem. **14**, 2355 (2004).

[18] G. E. Eperon, V. M. Burlakov, P .Docampo, A. Goriely, and H. J. Snaith*Morphological control for high performance, solution-processed planar heterojunction perovskite solar cells*, Adv. Funct. Mater. **24**, 151 (2014).

[19] N. J. Jeon, J. H. Noh, Y. C. Kim, W. S. Yang, S. Ryu, and S. Il. Seok*Solvent engineering for high-performance inorganic-organic hybrid perovskite solar cells*, Nature Mater. **13**, 897 (2014).

[20] J. H. Heo, D. H. Song, and S. H. Im*Planar $CH_3NH_3PbBr_3$ hybrid solar cells with 10.4% power conversion efficiency, fabricated by controlled crystallization in the spin-coating process*, Adv. Mater. **26**, 8179 (2014).

[21] Z. Xiao, Q. Dong, C. Bi, Y. Shao, Y. Yuan, and J. Huang*Solvent annealing of perovskite-induced crystal growth for photovoltaic-device efficiency enhancement*, Adv. Mater. **26**, 6503 (2014).

[22] J-H. Im, I-H. Jang, N. Pellet, M. Grätzel, and N-G. Park*Growth of $CH_3NH_3PbI_3$ cuboids with controlled size for high-efficiency perovskite solar cells*, Nature Nano. **9**, 927 (2014).

[23] G. E. Eperon, S. D. Stranks, C. Menelaou, M. B. Johnston, L. M. Herz, and H. J. Snaith*Formamidinium lead trihalide: a broadly tunable perovskite for efficient planar heterojunction solar cells*, Energy Environ. Sci. **7**, 982 (2014).

[24] J. Burschka, N. Pellet, S-J. Moon, R. Humphry-Baker, P. Gao, M. K. Nazeeruddin, and M.Grätzel*Sequential deposition as a route to high-performance perovskite-sensitized solar cells*, Nature **499**, 316 (2013).

[25] P. Docampo, F. Hanusch, S. D. Stranks, M. Döblinger, J. M. Feckl, M. Ehrensperger, N. K. Minar, M. B. Johnston, H. J. Snaith, and T. Bein*Solution deposition-conversion for planar heterojunction mixed halide perovskite solar cells*, Adv. Energy Mater. **4**, 1400355 (2014).

[26] Y. Kutes, L. Ye, Y. Zhou, S. Pang, B. D. Huey, and N. P. Padture*Direct observation of ferroelectric domains in solution-processed $CH_3NH_3PbI_3$ perovskite thin films*, J. Phys. Chem. Lett. **5**, 3335 (2014).

[27] R. G. Pearson *Hard and soft acids and bases*, J. Chem. Educ. **45**, 581 (1968).

[28] N. Kitazawa, Y. Watanabe, and Y. Nakamura *Optical properties of $CH_3NH_3PbX_3$ (X = halogen) and their mixed-halide crystals*, J. Mater. Sci. Soc. **7**, 3585 (2002).

[29] A. Polman, M. Knight, E. C. Garnett, B. Ehrler, and W. C. Sinke *Photovoltaic materials ? present efficiencies and future challenges*, Science **352**, 307 (2016).

[30] M. Liu, M. B. Johnston, and H. J. Snaith *Efficient planar heterojunction perovskite solar cells by vapour deposition*, Nature **501**, 395 (2013).

[31] T. C. Sum and N. Mathews *Advancements in perovskite solar cells: photophysics behind the photovoltaics*, Energy Environ. Sci. **7**, 2518 (2014).

[32] G. Xing, N. Mathews, S. S. Lim, N. Yantara, X. Liu, D. Sabba, M.Grätzel, S. Mhaisalkar, and T. C. Sum *Low-temperature solution-processed wavelength-tunable perovskites for lasing*, Nature Mater. **13**, 476 (2014).

[33] L. M. Pazos-Outon, M. Szumilo, R. Lamboll, J. M. Richter, M. Crespo-Quesada, M. Abdi-Jalebi, H. J. Beeson, M. Vrucinic, M. Alsari, H. J. Snaith, B. Ehrler, R. H. Friend, and F. Deschler *Photon recyling in lead iodide perovskite solar cells*, Science **351**, 1430 (2016).

[34] J. M. Richter, M. Abdi-Jalebi, A. Sadhanala, M. Tabachnyk, J. P. H. Rivett, L. M. Pazos-Outon, K. C. Godel, M. Price, F. Deschler, and R. H. Friend *Photon reabsorption masks intrinsic bimolecular charge-carrier recombination in $CH_3NH_3PbI_3$ perovskite*, Nature Comm. **8**, 13941 (2016).

[35] M. Stuckelberger, B. Niesen, M. Filipic, S. Moon, J. Yum, M. Topic, and C. Ballif *Complex refractive index spectra of $CH_3NH_3PbI_3$ perovskite thin films determined by spectroscopic ellipsometry and spectrophotometry*, Phys. Chem. Lett. **6**, 66 (2015).

[36] J. Even, L. Pedesseau, J-M. Jancu, and C. Katan *Importance of spin-orbit coupling in hybrid organic/inorganic perovskites for photovoltaic applications*, Phys. Chem. Lett. **4**, 2999 (2013).

[37] V. D'Innocenzo, G. Grancini, M. J. P. Alcocer, A. R. S. Kandada, S. D. Stranks, M. M. Lee, G. Lanzani, H. J. Snaith, and A. Petrozza *Excitons versus free charges in organo-lead tri-halide perovskites*, Nature Comm. **5**, 3586 (2014).

[38] M. Saba, M. Cadelano, D. Marongiu, F. Chen, V. Sarritzu, N. Sestu, C. Figus, M. Aresti, R. Piras, A. Geddo-Lehmann, C. Cannas, A. Musinu, F. Quochi, A. Mura, and G. Bongiovanni *Correlated electron-hole plasma in organometal perovskites*, Nature Comm. **5**, 5049 (2014).

[39] K. Tanaka, T. Takahashi, T. Ban, T. Kondo, K. Uchida, and N. Miura *Comparative study on the excitons in lead-halide-based perovskite-type crystals $CH_3NH_3PbBr_3$ and $CH_3NH_3PbI_3$*, Solid State Commun. **127**, 619 (2003).

[40] D. Guo, D. Bartesaghi, H. Wei, E. M. Hutter, J. Huang, and T. J. Savenije *Photoluminescence from radiative surface states and excitons in methylammonium lead bromide perovskites*, J.Phys.Chem.Lett. **8**, 4258 (2017).

[41] S. D. Stranks, V. M. Burlakov, T. Leijtens, J. M. Ball, A. Goriely, and H. J. Snaith *Recombination kinetics in organic-inorganic perovskites: excitons, free charge, and subgap states*, Phys. Rev. Appl. **2**, 034007 (2014).

[42] C. Wehrenfennig, M. Liu, H. J. Snaith, M. B. Johnston, and L. M. Herz *Homogeneous emission line broadening in the organo lead halide perovskite $CH_3NH_3PbI_3$*, J. Phys. Chem. Lett. **5**, 1300 (2014).

[43] J. S. Manser and P. V. Kamat *Band filling with free charge carriers in organometal halide perovskites*, Nature Photon. **8**, 737 (2014).

[44] C. C. Stoumpos, C. D. Malliakas, and M. G. Kanatzidis *Semiconducting tin and lead iodide perovskites with organic cations: phase transitions, high mobilities, and near-infrared photoluminescent properties*, Inorg. Chem. **52**, 9019 (2013).

[45] Q. Wang, Y. Shao, H. Xie, L. Lyu, X. Liu, Y. Gao, and J. Huang *Qualifying composition dependent p and n self-doping in $CH_3NH_3PbI_3$*, Appl. Phys. Lett. **105**, 163508 (2014).

[46] C. Wehrenfennig, G. E. Eperon, M. B. Johnston, H. J. Snaith, and L. M. Herz *High charge carrier mobilities and lifetimes in organolead trihalide perovskites*, Adv. Mater. **26**, 1584 (2014).

[47] D. Venkateshvaran, M. Nikolka, A. Sadhanala, V. Lemaur, M. Zelazny, M. Kepa, M. Hurhangee, A. J. Kronemeijer, V. Pecunia, I. Nasrallah, I. Romanov, K. Broch,

I. McCulloch, D. Emin, Y. Olivier, J. Cornil, D. Beljonne, and H. Sirringhaus *Approaching disorder-free transport in high-mobility conjugated polymers*, Nature **515**, 384 (2014).

[48] J. You, L. Dou, Z. Hong, G. Li, and Y. Yang *Recent trends in polymer tandem solar cells research*, Polym. Sci. **38**, 1909 (2013).

[49] C. S. S. Sandeep, S. Cate, J. M. Schins, T. J. Savenije, Y. Liu, M. Law, S. Kinge, A. J. Houtepen, and L. D. A. Siebbeles *High charge-carrier mobility enables exploitation of carrier multiplication in quantum-dot films*, Nature Comm.**4**, 2360 (2013).

[50] Q. Long, S. A. Dinca, E. A. Schiff, M. Yu, and J. Theil *Electron and hole drift mobility measurements on thin film CdTe solar cells*, Appl. Phys. Lett.**105**, 042106 (2014).

[51] B. Shin, O. Gunawan, Y. Zhu, N. A. Bojarczuk, S. J. Chey, and S. Guha *Thin film solar cell with 8.4% power conversion efficiency using an earth-abundant Cu_2ZnSnS_4 absorber*, Prog. Photovolt. Res. Appl.**21**, 72 (2013).

[52] G. Brown, V. Faifer, A. Pudov, S. Anikeev, E. Bykov, M. Contreras, and J. Wu *Determination of the minority carrier diffusion length in compositionally graded Cu(In,Ga)Se_2 solar cells using electron beam induced current*, Appl. Phys. Lett.**96**, 022104 (2010).

[53] T. I. Kamins *Hall mobility in chemically deposited polycrystalline silicon*, J. Appl. Phys. **42**, 43574365 (1971).

[54] M. A. Green , *Silicon Solar Cells Advanced Principles and Practice*, UNSW Photovoltaics, Sydney, 1995.

[55] J. S. Blakemore *Semiconducting and other major properties of gallium arsenide*, J. Appl. Phys. **53**, 123 (1982).

[56] T. Leijtens, S. D. Stranks, G. E. Eperon, R. Lindblad, E. M. J. Johansson, J. M. Ball, M. M. Lee, H. J. Snaith, and I. J. McPherson *Electronic properties of meso-superstructured and planar organometal halide perovskite films: charge trapping, photodoping, and carrier mobility*, ACS Nano **8**, 7147 (2014).

[57] Q. Chen, H. Zhou, T-B. Song, S. Luo, Z. Hong, H-S. Duan, L. Dou, Y. Liu, and Y. Yang *Controllable self-induced passivation of hybrid lead iodide perovskites toward high performance solar cells*, NanoLett. **14**, 4158 (2014).

[58] Z. Xiao, Q. Dong, C. Bi, Y. Shao, Y. Yuan, and J. Huang *Solvent annealing of perovskite-induced crystal growth for photovoltaic-device efficiency enhancement*, Adv.Mater.**26**, 6503 (2014).

[59] W-J. Yin, T. Shi, and Y. Yan, *Unusual defect physics in $CH_3NH_3PbI_3$ perovskite solar cell absorber*, Appl.Phys.Lett. **104**, 4 (2014).

[60] A. Walsh, D. O. Scanlon, S. Chen, X. G. Gong, and S-H. Wei, *self-regulation mechanism for charged point defects in hybrid halide perovskites*, Angew. Chem. Int. Ed. **54**, 1791 (2015).

[61] M. A. Green, Y. Hishikawa, E. D. Dunlop, D. H. Levi, J. H-Ebinger, and A. W. Y. Ho-Baillie *Solar cell efficiency tables (version 51)*, Prog.in Photovolt. **26**, 3 (2018).

[62] W. Shockley and H. J. Queisser *Detailed balance limit of efficiency of p-n junction solar cells*, J.Appl. Phys. **31**, 510 (1961).

[63] J. M. Ball and A. Petrozza *Defects in perovskite-halides and their effects in solar cells*, Nature Energy **1**, 16149 (2016).

[64] T. Nishinaga, *Handbook of Crystal Growth: Fundamentals*, Elsevier, Amsterdam, 2015.

[65] G. A. Somorjai and Y. Li , *Introduction to Surface Chemistry and Catalysis*, Wiley-Interscience, New Jersey, 2010.

[66] Y. Yang, M. Yang, D. T. Moore, Y. Yan, E. M. Miller, K. Zhu, and M. C. Beard *Top and bottom surface limit carrier lifetime in lead iodide perovskite films*, Nature Energy **2**,

16207 (2017).

[67] G. Dingemans and W. M. M. Kessels *Status and prospects of Al_2O_3 based surface passivation schemes for silicon solar cells*, J. Vac. Sci. Tech. A Vacuum, Surface, Film **30**, 40802 (2012).

[68] A. P. Sutton and R. W. Balluffi, *Interfaces in Crystalline Materials*, Clarendon Press, Oxford, 1998.

[69] B. L. Adams, S. Ta'asan, D. Kinderlehrer, I. Livshits, D. E. Mason, C-T, Wu, W. W. Mullins, G. S. Rohrer, A. D. Rollett, and D. M. Saylor, *Extracting grain boundary and surface energy from measurement of triple junction geomtery*, Interface Science **7**, 321 (1999).

[70] Y. Huang and F. J. Humphreys, *Measurement of grain boundary mobility during recrystallization of a single-phase aluminium alloy*, Acta Materialia **47**, 2259 (1999).

[71] M. Taheri, H. Weiland, and A. Rollett, *Method of measuring stored energy macroscopically using statistically stored dislocations in commercial purity aluminum*, Metall. and Mat. Trans. A **37**, 19 (2006).

[72] W. T. Read and W. Shockley, *Dislocation models of crystal grain boundaries*, Phys. Rev. **78**, 275 (1950).

[73] J. Nelson, *The Physics of Solar Cells*, Imperial Collage Press, London, 2003.

[74] R. Brendel, *Thin-Film Crystalline Silicon Solar Cells Physics and Technology*, Willey-VCH Verlag GmbH, Weinheim, 2003.

[75] J. S. Yun, A. Ho-Baillie, S. Huang, S. H. Woo, Y. Heo, J. Seidel, F. Huang, Y-B. Cheng, and M. A. Green, *benefit of grain boundaries in organic-inorganic halide planar perovskite solar cells*, J.Phys.Chem.Lett. **6**, 875 (2015).

[76] D. W. deQuilettes, S. M. Vorpahl, S. D. Stranks, H. Nagaoka, G. E. Eperon, M. E. Ziffer, H. J. Snaith, D. S. Ginger, *Impact of microstructure on local carrier lifetime in perovskite solar cells*, Science **348**, 683 (2015).

[77] G. W. P. Adhyaksa, L. W. Veldhuizen, Y. Kuang, S. Brittman, R. E. I. Schropp, and E. C. Garnett, *Carrier diffusion lengths in hybrid perovskites: processing, composition, aging, and surface Passivation Effects*, Chem. Mater. **28**, 5 (2016).

[78] G. W. P. Adhyaksa, E. Johlin, and E. C. Garnett, *Nanoscale Back Contact Perovskite Solar Cell Design for Improved Tandem Efficiency*, Nature Lett. **17**, 7 (2017).

2

Carrier Diffusion Lengths in Halide Perovskites

This Chapter reports experimental values of carrier diffusion lengths in halide perovskite thin films and describes how processing, composition, aging and surface passivation affect the results. Considering the many possibilities for all three ions in the halide perovskite structure, hundreds of distinct compositions have already been reported. Such compositional changes can alter the carrier diffusion length - a key parameter for solar cell performance. Given the large compositional and processing parameter space, a rapid and simple technique for directly measuring diffusion length is needed. Here we use a laser grating technique to screen the diffusion length in perovskite materials. First, in pure $CH_3NH_3PbI_3$ we observe the diffusion length is largely dependent on the controlled processing conditions. Next, we partially replace iodide (I) with bromide (Br) and show that surprisingly, the diffusion length increases after aging for 1 month in air. Finally, we use a 4-nm Al_2O_3 layer (atomic layer deposition) to passivate the surface of $CH_3NH_3PbBr_3$, leading to a remarkable increase in diffusion length from 201 nm to 532 nm. The correlation that we have established between materials processing and diffusion length offers guidance in how to improve materials for devices.

2.1 Introduction

Hybrid halide perovskites are an emerging class of semiconductors that has drawn great interest recently because of its simple solution processing, tunable band gap,

high solar cell efficiency, and low lasing threshold [1–5]. They have the same ABX_3 configuration as the classic oxide perovskites but have metal halide rather than metal oxide corner-sharing octahedra. Typically, organic cation A is methylammonium (MA) or formamidinium (FA), B is lead (Pb) or tin (Sn), and X is chloride (Cl), bromide (Br), or iodide (I); already combining just these ions in pure or 50/50 mixes, nearly 50 distinct varieties emerge. Such compositional variations strongly affect material properties. For example, the addition of only a few percent of $PbCl_2$ to $MAPbI_3$ (known as $MAPbI_{3-x}Cl_x$) increases the film's diffusion length from $\sim$ 100 nm to 1 μm and raises optimized photovoltaic efficiency from 4.2 % to 12.2 % [6]. Even within a single material composition, solvent engineering used to increase the domain size of the film has already been shown to have dramatic effects on device performance [3, 7]. While there are many ways to screen materials and processing conditions, the diffusion length of the photogenerated carrier has been one of the properties most strongly correlated with optoelectronic device performance [6, 8]. Despite this importance, the most common methods for measuring this diffusion length are not compatible with simple, rapid screening that would be ideal for testing the large number of possible new materials and processing conditions. For example, photoluminescence lifetime measurements can be combined with mobility measurements to yield indirectly the carrier diffusion length, but these measurements are impractically slow to be used for routine testing. Clearly a simple, rapid, and direct method for measuring diffusion length would be useful in screening both new hybrid halide perovskite materials and processing conditions that lead to better material quality.

Here we apply such a method, called the steady-state photocarrier grating (SSPG) technique, to hybrid perovskite materials and use it to investigate the influence of material composition, material processing conditions, aging, and surface passivation on the diffusion length. Originally developed in the 1980s as a way to measure diffusion length in amorphous silicon thin films, SSPG relies on a change in conductivity in the presence of an optical grating created by two interfering laser beams [9, 10]. First, we use SPPG to show that varying the solvent and processing conditions can lead to at least a factor of 2 variation in the diffusion length of methylammonium lead iodide ($CH_3NH_3PbI_3$ or $MAPbI_3$). Next we demonstrate how the diffusion length varies with halide substitution, and for each composition, how it changes with aging. Finally, we show that a thin (4-nm) passivating aluminium oxide layer can increase the diffusion length of methylammonium lead bromide ($CH_3NH_3PbBr_3$ or $MAPbBr_3$) by nearly a factor of 3, while the process of adding the same coating dramatically degrades $MAPbI_3$.

2.2 Setup

Figure 2.1a shows a schematic of the SSPG measurement setup used in this study, where we measure a small change in sample conductivity (at a given voltage) in the presence of an optical grating. The grating is created by overlapping two interfering laser beams on the sample. The measurement is conducted under illumination of I_1

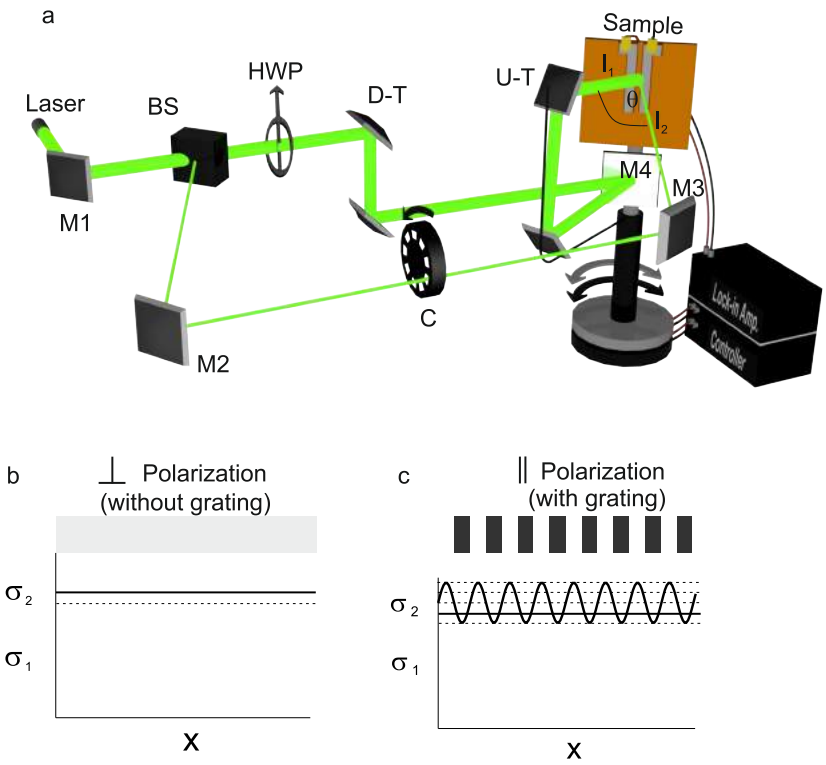

Figure 2.1: **(a)** Schematic of the setup: I_1 is the strong beam, I_2 is the weak beam, θ is the angle between I_1 and I_2, M_1, M_2, M_3, and M_4 are mirrors, BS is a beam splitter, HWP is a half-wave plate, C is chopper, U-T is up-transport mirrors, and D-T is down-transport mirrors. The axis has two rotating stages (black and gray) and each can rotate independently: (1) the sample along with M_4 underneath (gray arrow) and (2) the up-transport mirror connected with the arm (black arrow). Sample: a perovskite film deposited on a glass substrate with two coplanar gold (Au) electrodes. **(b)** Lateral conductivity pattern without grating: when I_1 and I_2 are orthogonally polarized. **(c)** Lateral conductivity with grating: when I_1 and I_2 are in parallel polarization. The conductivity σ_1 and σ_2 are not to scale for better visualization (perturbation by σ_2) should be very small relative to σ_1 in order to maintain the steady-state condition).

and I_2, where the intensity of beam I_1 is much stronger than the chopped beam I_2. In this way, I_1 serves as a background illumination ensuring an almost constant carrier generation rate over the sample surface, while I_2 acts as a probe beam providing a small perturbation ($\sim 5\%$). The change in conductivity is directly measured on the sample using a lock-in amplifier for two configurations: (1) when the two beams have orthogonal polarization states and therefore do not interfere (**Figure 2.1b**), and (2) when the polarization states are aligned, creating a periodic optical grating (**Figure 2.1c**). The grating period can be controlled by changing the angle between the two beams (grating period decreases as angle increases). The down-transport mirrors, up-transport mirrors, and rotating stages enable continuous overlap between I_1 and I_2 with varying angle.

Solving the one-dimensional steady-state diffusion equation leads to a relation

between the photoconductivity ratio and grating period [11–13]:

$$\left[\frac{1}{1-\beta}\right]^{\frac{1}{2}} = \frac{(2\pi L_D)^2}{(2Z)^{\frac{1}{2}}}\left[\frac{1}{\Lambda}\right]^2 + \frac{1}{(2Z)^{\frac{1}{2}}}, \tag{2.1}$$

where Λ is the grating period, β is the photoconductivity ratio of lock-in amplifier signals under the parallel and perpendicular polarization configurations (**Figure 2.1c,b**), L_D is the diffusion length of the photogenerated carrier, and Z is a fitting parameter related to non-ideal grating formation (e.g., due to surface scattering or poor photoconductivity). L_D describes ambipolar transport of the Coulomb-coupled electron and hole, but it will be dominated by the photogenerated carrier with the smaller diffusion length (e.g., minority carrier in a doped material). The value of β will be close to unity when diffusion length is much longer than the grating period. This case takes place when carrier diffusion significantly smears out the grating, so that the signal is the same if I_1 and I_2 create a grating (**Figure 2.1c**) or not (**Figure 2.1b**). Increasing the grating period beyond the diffusion length drastically decreases the sample conductivity, consequently decreasing β. The value of Z falls between 0 and 1 ($0 < Z < 1$; 1 is for a perfect grating) and depends on factors such as photosensitivity of the sample and grating contrast ratio [10]. The diffusion length (L_D) can be directly extracted from a linear fit of **equation 2.1**, with error bars coming from the fitting procedure (see Supporting Information for details).

2.3 Processing effect

We begin by studying the dependence of diffusion length on the sample preparation method using $MAPbI_3$. Samples were prepared by depositing thin-film hybrid perovskites on glass substrates by spin-casting from different solvents (details in the Supporting Information). On top of the film, two gold electrodes were deposited (1 mm spacing) for electrical contacts. **Figure 2.2a** shows a transform of change in conductivity ratio (β) as a function of the grating size (Λ) for $MAPbI_3$ and the corresponding diffusion lengths for each of the three processing conditions. The film processed with dimethylsolfoxide (DMSO) solvent yielded the longest diffusion length (up to 490 nm) followed by the dimethylformamide (DMF, up to 396 nm) and gamma-butyrolactone (GBL, up to 288 nm) films. The SEM images show morphological differences consistent with the measured diffusion lengths: films cast from DMSO formed large, smooth plates, while films from DMF were continuous but had a higher roughness, and those cast from GBL had the highest apparent porosity **Figure 2.2b-d**. A variety of different processing treatments including solution filtration before spin coating and toluene anti-solvent dripping also were tested and showed distinct differences in diffusion length (more details in **Figure 2.5a**). Diffusion length values we measure are similar to what has been reported using other techniques including intensity modulated photocurrent/photovoltage spectroscopy (IMPS/IMVS), photoluminescence quenching, and photoluminescence lifetime combined with mobility, where values of 100 to 1000 nm are typical, depending on preparation conditions [6, 8, 14].

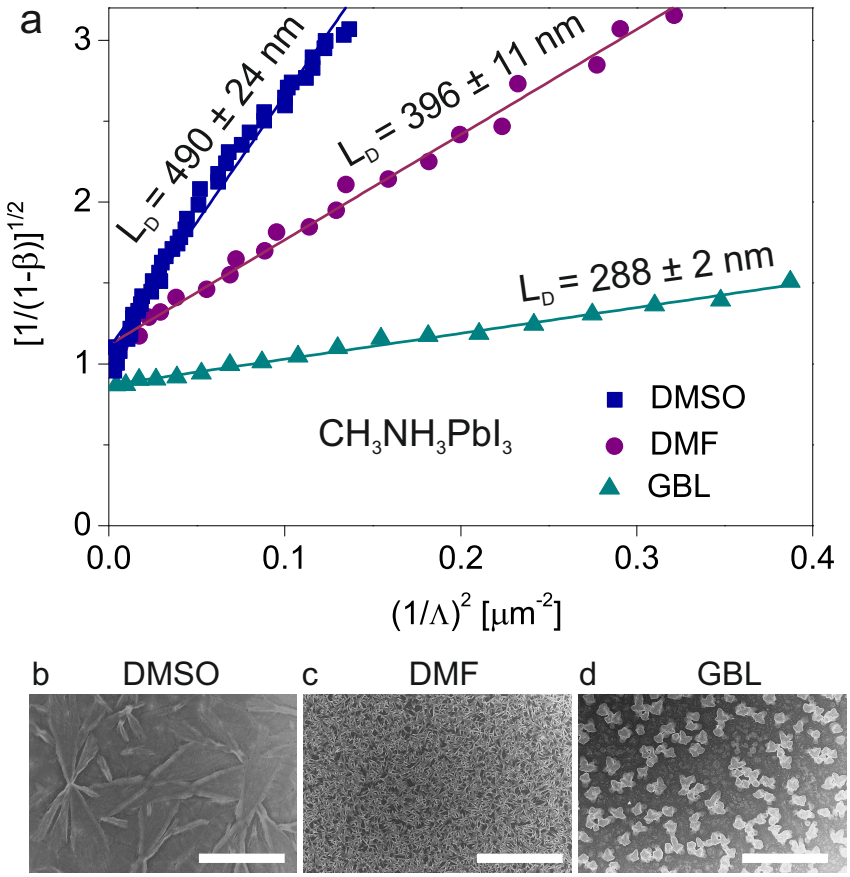

Figure 2.2: Variation of carrier diffusion length in $MAPbI_3$. **(a)** Experimental data of a transform of the photoconductivity ratio (β) as a function of grating size (Λ). The lines are the linear fitting of each corresponding experimental data set. Corresponding scanning electron microscope images of samples prepared with different solvents: **(b)** DMSO, **(c)** DMF, and **(d)** GBL.

To gain more insight into the origin of the observed morphology that is created by the solvent, we analyze X-ray diffraction patterns of six $MAPbI_3$ films processed from DMSO, DMF, and GBL, each with two different preparation conditions (**Figure 2.5b**). All films show a perovskite structure with tetragonal phase/*P4mm* (a = b = 8.86 Å, c = 12.67 Å) typical of literature reports for $MAPbI_3$ [7, 16]. We observed a direct correlation between diffusion length and the broadening of the XRD peak (**Figure 2.5c-e**), which could arise from effects such as smaller crystallite size or micro-strain within the film [17]. Assuming that the broadening arises entirely from the size of the crystallites (Supporting information for details), the full width at half-maximum of the peak corresponding to the (220) crystal orientation was used to estimate the crystallite size in the six $MAPbI_3$ films with different sample preparation conditions. The diffusion length increased by more than a factor of 2 (from 216 to 490 nm) with an increase in (XRD based) estimated crystallite size from 78 to 152 nm.

2.4 Compositional and aging effects

In addition to looking at solvent and preparation effects on diffusion length in the pure iodide, we have also examined how the diffusion length varies with halide composition. Here samples based on neat and mixed $MAPbI_3$ and $MAPbBr_3$ (hereafter denoted as $MAPb(I_{1-x}Br_x)_3$) are studied. The mixed $MAPb(I_{1-x}Br_x)_3$ is of interest because of its bandgap can be tuned throughout the region of interest for multijunction solar cells and visible light-emitting diodes or laser [2, 4, 18–22], although there are currently some problems with spontaneous phase separation under solar illumination [23]. We soaked the samples under laser illumination before the SSPG measurement in order to stabilize the properties (see methods). Spin coating from the mixed halide solutions was used to prepare these alloy samples (see methods). The bandgap gradually becomes larger by adding $MAPbBr_3$ into the neat $MAPbI_3$, as can be seen from gradual blue-shifted absorption with a clear onset following a linear relation $E_G = 0.69[Br] + 1.55$; where E_G is the optical bandgap (eV) and [Br] is the $MAPbBr_3$ fraction relative to $MAPbI_3$, from 0 to 1 (**Figure 2.6a,b**). There is only one single phase observed across the transition from tetragonal to cubic phase implying a successful incorporation of iodide-bromide ions into the perovskite structures.

The plot in **Figure 2.3a** shows that the $MAPbI_3$ film has a diffusion length (475 nm) about two times longer than that of $MAPbBr_3$ film (201 nm), as indicated by its steeper slope. All alloy compositions initially exhibit diffusion lengths below those of both pure $MAPbBr_3$ and $MAPbI_3$ (**Figure 2.3b**), consistent with an earlier proposal of trap-state formation in the mixed halide perovskites [23]. Interestingly, after aging the films for 1 month (stored in air at room temperature in the dark) all mixed halide films show a substantial increase in diffusion length from initial values of 151 - 183 nm to final values of 238 - 392 nm (**Figure 2.3b** and **Figure 2.7**). The diffusion length in aged alloy films increases proportionally with the Br fraction up to 0.66 (at 1.97 eV band gap) before dropping to values very close to those seen in the pure bromide film. The pure bromide film showed no change in diffusion length with aging, while pure iodide film showed a large decrease in diffusion length after one month. This result is consistent with the XRD, which showed partial decomposition to lead iodide only for the pure iodide perovskite; the pure bromide and mixed halide perovskite films showed no crystalline secondary phases (**Figure 2.6c**). The only change in the alloy perovskite films with aging was a slight blue shift in the absorption onset (**Figure 2.6a,b**), consistent with a previous report [20].

The origin of increased diffusion length with aging for mixed halide perovskite films is still unclear, but reactive oxygen species have been reported to play a role in deactivating defect states in the mixed halide perovskites [24, 25]. This strong difference in stability with variation in composition underlines the importance of having a simple and rapid technique for directly measuring the diffusion length of the perovskite itself, isolating its aging characteristics from those of the interfacial and contact layer used in complete devices.

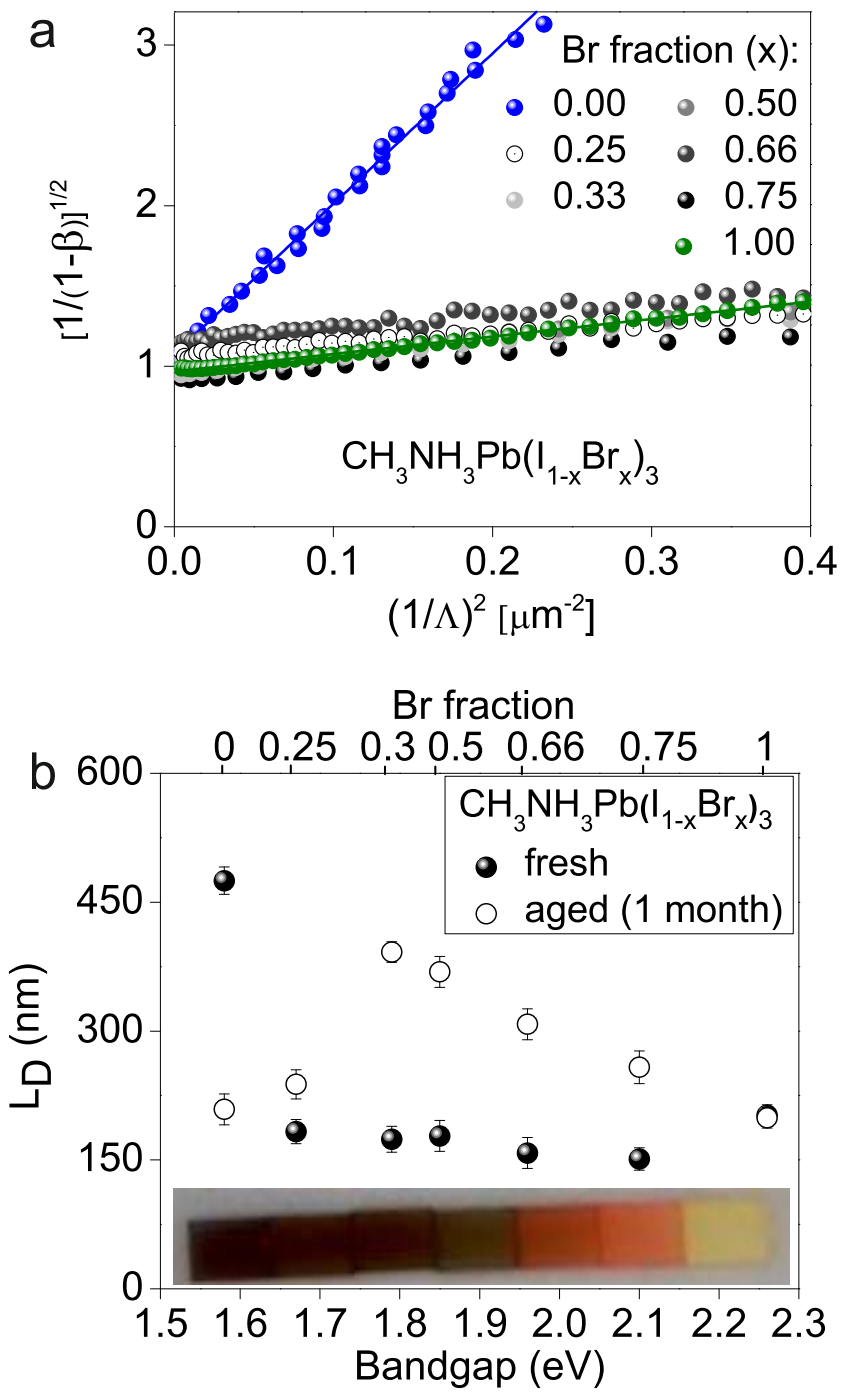

Figure 2.3: Diffusion length and aging effects in $MAPb(I_{1-x}Br_x)_3$. **(a)** Experimental data of a transform of the photoconductivity ratio β as a function of grating size (Λ) before aging. The lines are the linear fitting of data from each corresponding composition (the fitting lines and diffusion length for mixed samples are not displayed for clarity). **(b)** Diffusion length as a function of (initial) optical bandgap and bromide fraction: fresh sample (filled circle) and aged samples (open circel); inset photograph of aged samples arranged with their corresponding bandgap.

2.5 Surface passivation effect

Although the experiment creates an optical grating throughout the entire perovskite film thickness, a transfer matrix calculation [26, 27] shows that most of the highest photocarrier generation rate occurs at the surface of the film. This suggests that the SSPG technique could be sensitive to surface recombination and surface passivation effects [28]. **Figure 2.4** shows the transform of the photoconductivity ratio as a function of grating size of $MAPbI_3$ and $MAPbBr_3$ films before and after coating with a 4-nm thin amorphous aluminum oxide (Al_2O_3) layer deposited by atomic layer deposition (ALD). The deposition takes place at 100 °C using trimethylaluminum (TMA) and water (H_2O) as the Al_2O_3 precursors and the whole process takes 30 min (50 cycles). There is a dramatic increase in diffusion length for the $MAPbBr_3$ film from 201 to 532 nm, while the diffusion length of the $MAPbI_3$ film decreases from 475 to 213 nm. From XRD it is clear that $MAPbI_3$ decomposes substantially, as indicated by the appearance of PbI_2 precursor peaks (**Figure 2.10b**) after ALD deposition. In fact, we observed that the $MAPbI_3$ had started to decompose even after 10 cycles of ALD (<1 nm). This can explain both the lower diffusion length and poor signal-to-noise ratio in the measurement. In contrast, the cubic phase of $MAPbBr_3$ is still preserved without any trace of precursor peaks observed (**Figure 2.10a**).

To elucidate if surface passivation is the main reason for the diffusion length improvement, we conducted a vacuum annealing experiment by placing a $MAPbBr_3$ film in the ALD chamber in which all parameters were set to be the same (100 °C, 30 min, 10^{-3} mbar), only without feeding in the precursors. We observed the diffusion length also increased after the vacuum annealing, but only by about 20 % from its initial value, which cannot account for the nearly threefold increase seen after ALD (**Figure 2.9**). Previously a thin ALD alumina layer has been shown to be an effective passivation scheme for a variety of semiconductor surfaces (Si [29], CIGS [30], ZnO [31]) either through a field effect (fixed interfacial charges) or reduced interfacial trap state density, both of which reduce the surface recombination velocity. However, the exact role of the ALD passivation on hybrid perovskites is still under investigation. As ALD has been used in the past as an encapsulation layer to improve the stability of metal nanowire transparent electrodes [32], we expect it could also serve a similar role here.

2.6 Conclusions

In conclusion, we have performed a simple and rapid technique to screen quantitatively the diffusion length in halide perovskite thin films. This laser grating technique directly measures the diffusion length, which eliminates the need to measure lifetime and mobility separately. We demonstrate that the diffusion length halide perovskite is very sensitive with processing condition. For instance in $MAPbI_3$ films the diffusion length can be improved from 216 to 490 nm just by changing the deposition condition. We also show that the diffusion length in mixed $MAPb(I_{1-x}Br_x)_3$ films has a complex aging behavior that varies dramatically with composition: pure iodide films degrade,

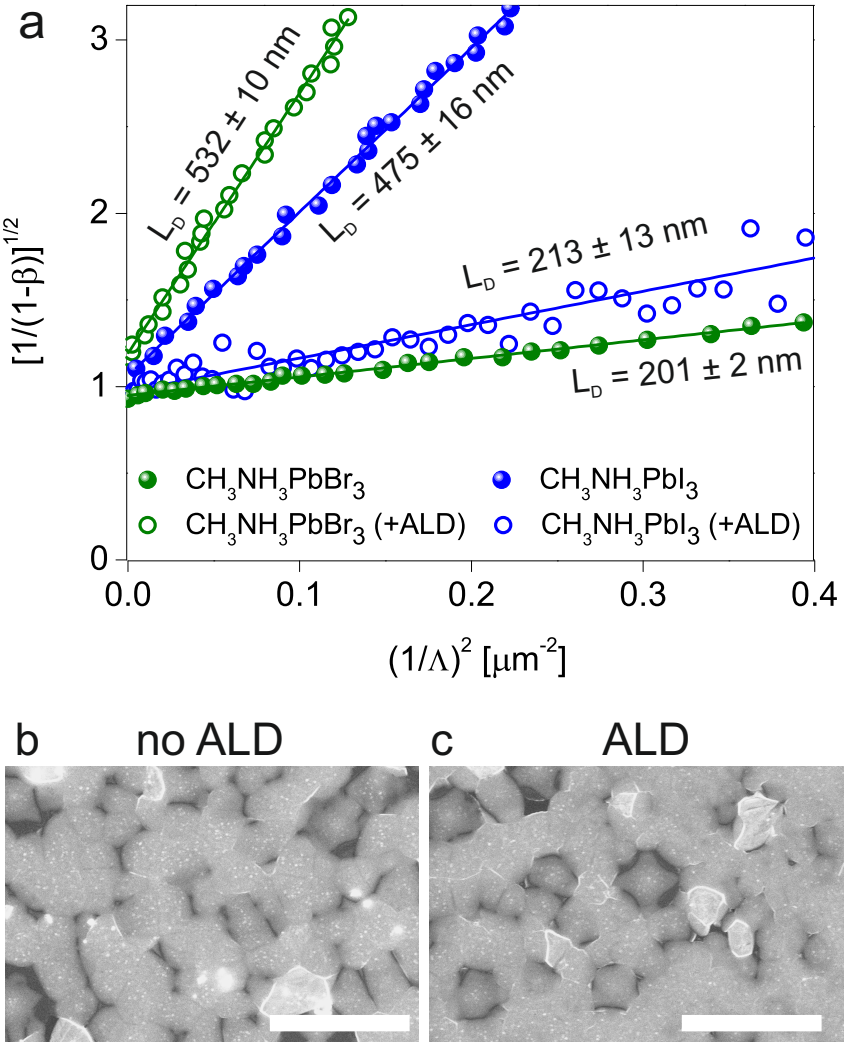

Figure 2.4: Surface passivation effect on the lateral diffusion length. **(a)** Experimental data of a transform of photoconductivity ratio (β) as a function of grating size (Λ) before and after passivation with 4-nm thin aluminum oxide film deposited by atomic layer deposition (ALD); the lines are the linear fitting of each corresponding data. Scanning electron microscope images of $MAPbBr_3$ before **(b)** and after **(c)** ALD; the bright-small dots are from sputtered chromium particles.

pure bromide films do not change, and the alloy films improve with aging. Finally, we demonstrate an improvement in the diffusion length of $MAPbBr_3$ films from 201 to 532 nm after deposition of a 4-nm thin Al_2O_3 layer by ALD. This remarkable improvement in diffusion length justifies further investigations on interfacial modification with other oxides such as nickel oxide (NiO_x), molybdenum oxide (MoO_x), and titanium oxide (TiO_x) for broadening its applicability not only for solar cells but also for photoelectrochemical water splitting.

2.7 Outlook and data validation

SSPG technique measures the change in photoconductivity laterally across the sample, which is associated with the diffusion of photogenerated carriers. This measurement geometry is distinct as compared to other methods that measure carrier diffusion through the thickness of the film. Although in a standard solar cell current is extracted in the direction perpendicular to the substrate through the thickness of the film, diffusion in the lateral direction is still strongly correlated to device efficiency for materials whose transport is not strongly anisotropic (e.g. 2D halide perovskite) or a device relying on lateral charge collection (e.g. back-contact solar cells). For example, a study of halide perovskite thin film devices with domain sizes 100 times larger than the film thickness has shown that grain boundary recombination still plays a role in decreasing solar cell performance, indicating the influence of lateral diffusion [15]. This indicates that the diffusion length measured by SSPG in the lateral geometry is a relevant parameter for solar cell performance.

In this chapter, to confirm that the SSPG technique applied to hybrid perovskites yields a diffusion length similar to that measured by more conventional techniques, we used electron beam induced current (EBIC) to measure the diffusion length in $MAPbI_3$ and $MAPbBr_3$ films of the same quality, processing conditions, and lateral sample geometry used for SSPG measurements. The EBIC values agree well with those obtained using SSPG (**Figure 2.12**). This setup has also been used to benchmark carrier diffusion lengths in halide perovskites with state-of-the-art silicon based (a-Si:H, a-SiGe:H, and μ c-Si:H), and chalcopyrite based ($Cu(In,Ga)Se_2$) thin films [33]. The next generation of the SSPG setup to account further for error corrections and beyond will be discussed in Chapter 4.

2.8 Supporting information

2.8.1 Sample preparation

Perovskite films were deposited on insulating glass substrates (1.5×1.5 cm). Prior to the deposition, the substrates were cleaned by the following protocol: 15 minutes in acetone (ultra-sonication), 15 minutes in isopropanol (ultra-sonication), 1 - 2 hours under hydrochloric acid bath (18 % in deionized water); between each step the substrates were rinsed with isopropanol and dried with nitrogen (N_2) flow; the substrates were then

cleaned using an oxygen plasma (50 W, 2 minutes) to make the surface hydrophilic. The perovskite film was formed by spin-coating (10,000 rpm, for 60 seconds) a perovskite solution (1 - 2 M in DMSO, 1 M DMF, or 1 M GBL) on the glass substrate followed by thermal annealing at 100 °C for 30 minutes; all deposition processes were done in a N_2 glovebox. The perovskite solutions were prepared following the previous report [2]. It was synthesized by mixing equimolar concentrations of methylammonium halides (CH_3NH_3X; X = I, Br) and lead halide (PbX_2; X = I, Br) precursors. The mixture was ultra-sonicated to help dissolving any precursor flakes followed by 2 - 3 hours stirring in the N_2 glove box. The CH_3NH_3 was synthesized by mixing methylamine (Sigma-Aldrich, 33 wt. % in ethanol) and hydrobromic (or hydroiodic) acid (Sigma-Aldrich, 48-57 % in H_2O) in an ice bath for 2 hours. The solvents were evaporated by heating the solution at 150 °C while stirring until a white or occasionally yellowish powder was formed. The powder was then recrystallized from a boiling ethanol to form white powders (CH_3NH_3I) or flakes (CH_3NH_3Br). The PbI_2 and $PbBr_2$ were used as purchased (Sigma-Aldrich, 99 %). For mixed $MAPb(I_{1-x}Br_x)_3$ solution, 1 M $CH_3NH_3PbI_3$ solution and 1 M $CH_3NH_3PbBr_3$ solutions were mixed by varying the volume ratio (for example 1 : 3 of I : Br means 1 mL of 1 M $CH_3NH_3PbI_3$ mixed with 3 mL of 1 M $CH_3NH_3PbBr_3$). Two co-planar gold electrodes were deposited on the thin film perovskites using a thermal evaporator (base pressure 10^{-5} mbar). The thickness of the electrodes was about 100 to 170 nm with 1 mm spacing in between. For the optimized condition: the optimized films with DMSO or GBL were from 1 M filtered solution of $MAPbI_3$ (0.22 micron, PTFE), and the solution was stirred overnight at 60 - 70 °C before the deposition. Optimized films with DMF were from 2 M solution of $MAPbI_3$, hydrochloric iodic was added into the solution (<8 % v/v), toluene drop casting during the spin-coating (at 10^{th} - 15^{th} second out of 60 seconds spinning). Otherwise, non-optimized films are from 1 M solution of $MAPbI_3$ with 60 seconds spinning with no pre-heat treatment of solution involved.

2.8.2 Atomic layer deposition (ALD)

Al_2O_3 was deposited on the thin film of halide perovskites in an Oxford Instrument OpALTM reactor located in a cleanroom facility at Technical University of Eindhoven. The 4-nm Al_2O_3 layer, with thickness monitored by an *in situ* spectroscopic ellipsometry, were deposited on the substrate by 50 cycles at 100 °C. Each ALD cycle consists of an $Al(CH_3)_3$ dosing of 0.02 s, followed by a purge of 3.5 s, then a water vapor exposure of 0.02 s, followed by a purge of 3.5 s.

2.8.3 Laser grating setup

A diode-pumped solid-state laser (532 nm, LasNova Series 50 green) was used as an excitation source. The power output, coherence length, and polarization ratio of the laser was 4.1 mW, > 5 m, and 500 : 1, respectively. The beam was split into two-coherent beams at BK7 glass window. The intensity ratio I_1/I_2 between the two beams was 15, and adjusted by a neutral density filter. A DC voltage of 10 V was applied

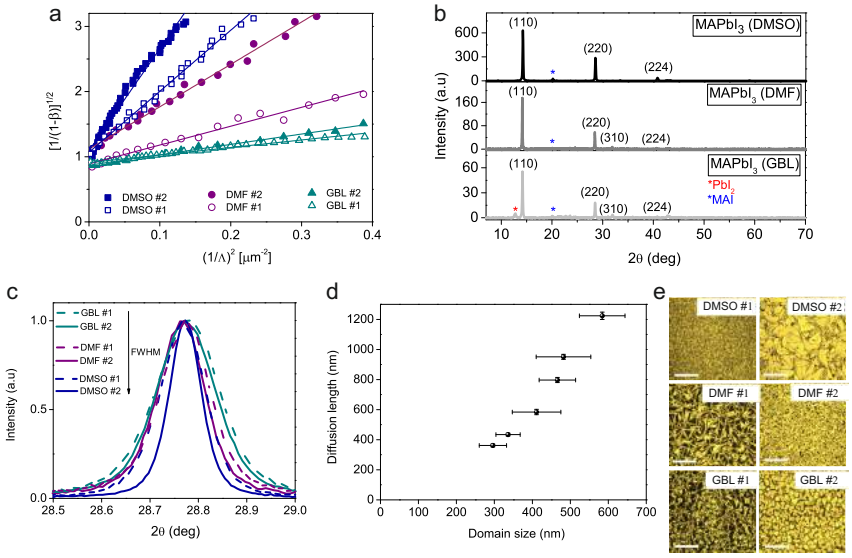

Figure 2.5: Diffusion length and crystallite size correlation in $MAPbI_3$: **(a)** Experimental data of a transform of the conductivity ratio (β) as a function of grating size (Λ): The lines are the linear fitting of each corresponding experimental data. **(b)** XRD spectra scanned from 7-70° and all showing the same crystal phase (tetragonal phase/P4mm (a = b = 8.86 Å, c = 12.67 Å) with small fraction of precursor traces (PbI_2 and MAI). **(c)** XRD at (220) crystal orientation showing different XRD peak width. **(d)** Measured diffusion length as a function of estimated crystallite size (determined from the XRD peak width). **(e)** Optical images (top view, with the scale bar of 50 μm) of samples prepared with different solvent and treatments: #1 refers to non-optimized samples, and #2 refers to the optimized ones.

via the two electrodes on the sample, corresponding to an electric field strength of about 100 V/cm. This field strength was low enough to be in the diffusion regime. The polarization of beam I_1 was changed by a half-wave plate. The beam I_2 was chopped at 110 Hz. Two rotating mirrors were used to direct the two beams onto the sample aiming for continuous overlap while changing the angle between the two-interfering beams. For hybrid perovskite measurements, To be in the linear regime, we typically varied the angle from 3° to 15°, and this corresponds to optical grating periods from ~ 5 μm down to ~ 0.8 μm; the lower boundary for the measured diffusion length is about 0.1 times the grating period. The sample was pre-soaked under ~ 100 mW/cm^2 laser illumination for 1 - 2 minutes before the measurement to minimize the light-induced phase separation effect to ensure consistent measurements.

The uncertainty of the measured diffusion length values in this chapter is derived from the linear fitting of the data to the equation 2.1. With a linear fitting of [Y] = a[X] + c; where a is the slope, and c is the intercept of the data plot. So, we can calculate the diffusion length as:

$$L_D = \frac{1}{2\pi}\left(\frac{a}{c}\right)^{\frac{1}{2}}, \tag{2.2}$$

The error bar of L_D is calculated by summing the error propagation of the slope (a)

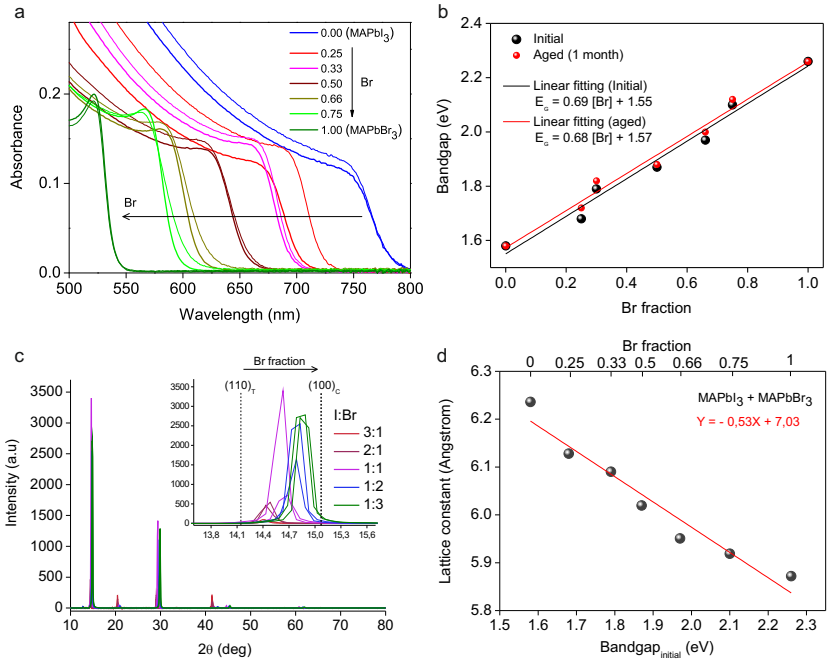

Figure 2.6: Bandgap and lattice constant correlation in $MAPb(I_{1-x}Br_x)_3$: **(a)** Absorption spectra as a function of wavelength showing a gradual blue-shift for increasing Br fraction before (thin lines) and after (thick lines) 1 month aging in air. **(b)** Linear correlation of bandgap as a function of Br fraction (bandgap increases with increasing Br fraction) showing the optical stability of $MAPb(I_{1-x}Br_x)_3$ after aging for 1 month in air. **(c)** XRD spectra showing gradual transition from (110) tetragonal to (100) cubic with increasing Br fraction. **(d)** Linear correlation of lattice constant (derived from the XRD peak) as a function of bandgap showing a linear reduction of lattice constant as the bandgap increases (as Br fraction increase).

and the intercept (c) as:

$$\delta L_D = \frac{1}{4\pi}\left(\frac{a}{c}\right)^{\frac{1}{2}}\sqrt{\left(\frac{\delta a}{a}\right)^2+\left(\frac{\delta c}{c}\right)^2}, \tag{2.3}$$

The δa and δc are errors based on confidence intervals on a and c. The standard error values of a and c from the regression analysis are used to construct δa and δc. Here we take 90 % critical values from the t-distribution with 20 to 30 degrees of freedom. This gives 90 % confidence intervals that are 1.31 to 1.33 times larger than the standard error values. Further correction and considereation of data and error analysis will be discussed in Chapter 4.

2.8.4 Estimating crystallite size using X-ray diffraction analysis

The crystal structure of the samples was analyzed based on their X-ray diffraction spectra (using a Bruker D2-phaser instrument, Bragg-Brentano geometry) under the

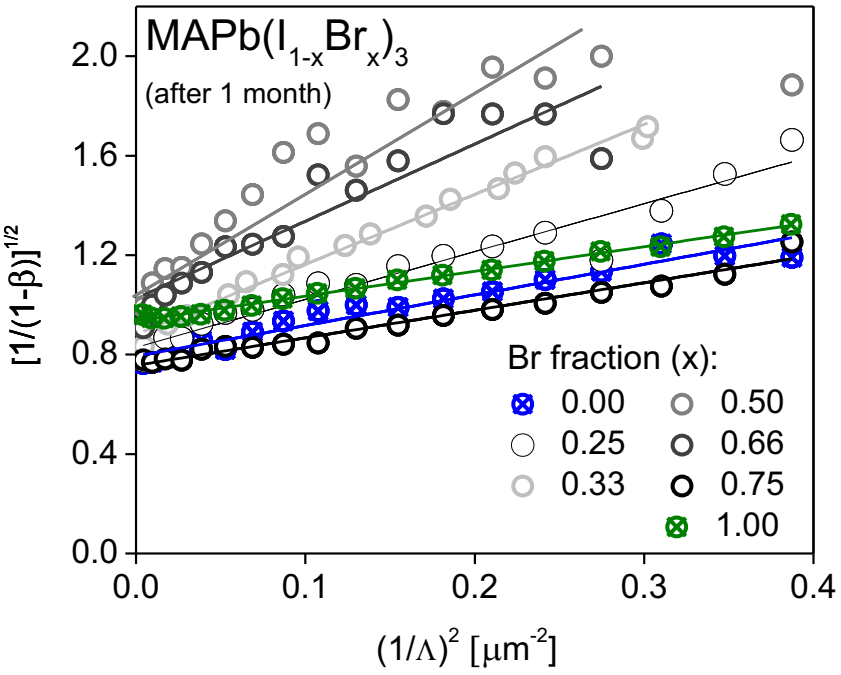

Figure 2.7: Experimental data of MAPb($I_{1-x}Br_x$)$_3$ after 1 month aging (in air): Experimental data of a transform of the conductivity ratio (β) as a function of grating size (Λ), the lines are linear fittings of each corresponding experimental data. Diffusion length values and errors are tabulated in **Table S1**.

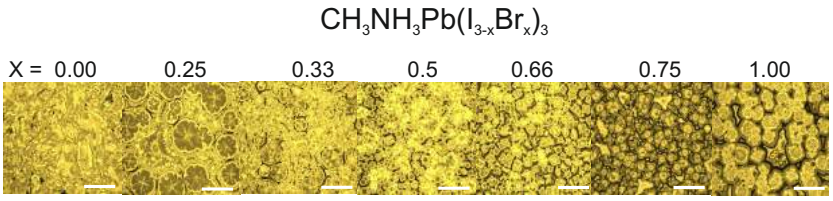

Figure 2.8: Optical images of MAPb($I_{1-x}Br_x$)$_3$ after 1 month aging (in air).

θ - 2θ configuration. The average crystallite size was determined using the Scherrer equation [17]:

$$\langle R \rangle = \frac{k\lambda}{B\cos\theta}, \tag{2.4}$$

where $\langle R \rangle$ is the average crystallite size in the crystal direction along the normal of the diffraction plane, k is a constant that depends on the crystallite shape, but normally is approximately 0.94 ($k = 0.94$ for a cubic crystallite shape), λ is the X-ray wavelength (here $\lambda = 0.154$ nm for Cu-Kα), B is the 2θ full-width-half-maximum (FWHM) peak (in Radian) after correction by the FWHM contributed by the instrumental broadening, θ is the Bragg angle. The FWHM correction was done by taking the XRD spectra of a certified Corundum standard and substracting the XRD FWHM peak of the perovskite at 28.8° (220) with the Corundum FWHM peak at 25.6 °. A systematic

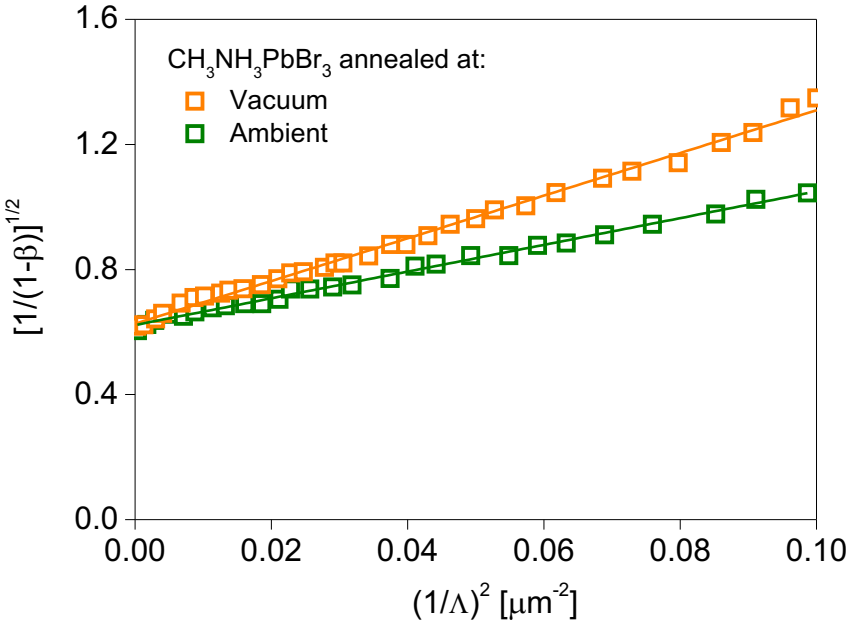

Figure 2.9: Diffusion length of MAPbBr3 under different annealing.

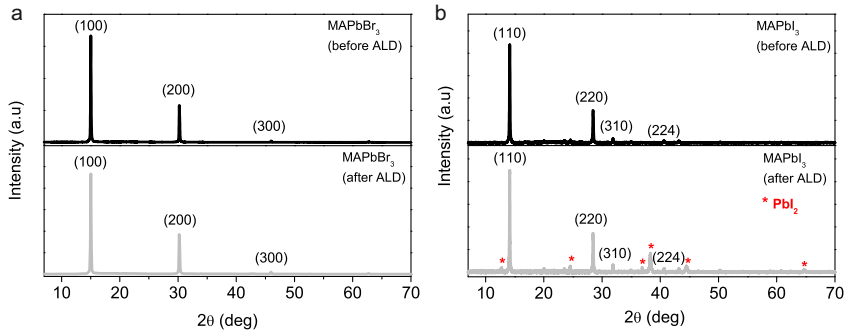

Figure 2.10: X-ray diffraction after ALD passivation.

error because of a different sample thickness (Z-height error correction) is minimized by scanning XRD spectra of a sample also containing CeO_2, and then adjusting the peak position according to the pure CeO_2 standard. The error range of the $\langle R \rangle$ for each sample was estimated by calculating the $\langle R \rangle$ on 3 - 4 samples with the same preparation condition. All measurements were performed under the same instrumental setting: using 0.6 divergence slit to control illuminated area, 1 mm beam knife to limit unwanted scattering and optimize the low angle spectra, nickel filter to reduce 20 - 30 % contribution from Cu-Kβ. The scan interval ($\Delta 2\theta$) was 0.01° with multiple scans repeated to improve signal-to-noise ratio.

However, the broadening of the XRD peaks is not only due to crystallite size and instrumental effects, but also lattice strain. The effect of lattice strain can be represented

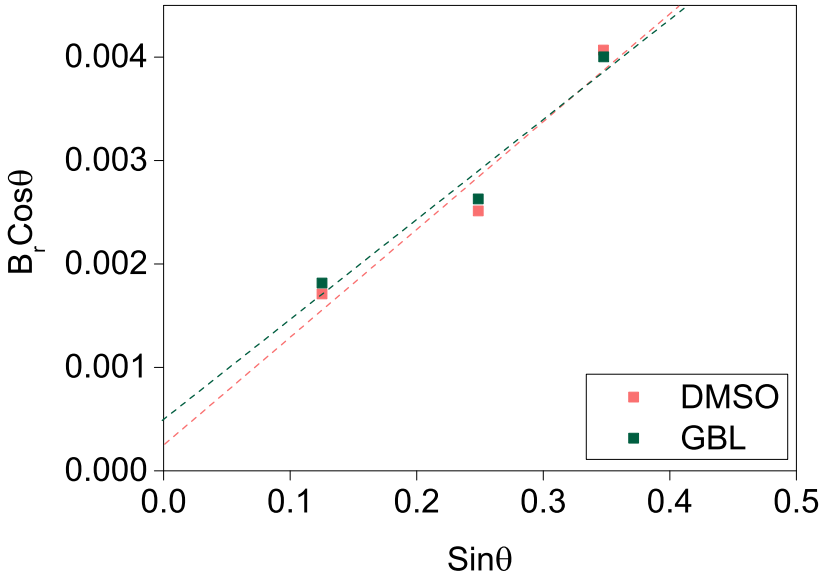

Figure 2.11: Distinguishing lattice strain and crystallite size from the XRD peak broadening. This data already substracted by the intrumental broadening.

by the [17]:

$$B_{strain} = \eta \tan\theta, \tag{2.5}$$

where η is the strain of the perovskite material. So, the total broadening of XRD peak, after substrating with the contribution from intrumental broadening, can be expressed as summation of equation 2.4 and 2.5:

$$B_{total} = \frac{k\lambda}{\langle R \rangle \cos\theta} + \eta \tan\theta, \tag{2.6}$$

by multiplying equation 2.6 by $\cos\theta$, we find:

$$B_{total} \cos\theta = \frac{k\lambda}{\langle R \rangle} + \eta \sin\theta, \tag{2.7}$$

If we plot the B_{total} *versus* $\sin\theta$, the intercept tells us about crystallite size, and the slope provides the strain information. The closer the intercept to the origin point (0,0), the larger the crystallite size. While the steeper the slope, the larger the strain. **Figure 2.11** shows the plot of two extrema cases used in this study (sample with largest and smallest estimated crystallite size made by DMSO, and GBL, respectively). After correction with the lattice strain, the estimated crystallite size seems to increase proportionally from the original value (equation 2.4). Although we should question the accuracy of lattice strain contribution based on this data where the second data are quite off from the linear fitting. The other way to find the strain contribution is by comparing the data with a large single crystal halide perovskite materials. However, even using a large crystal halide perovskite still gives twice larger broadening than

just a Corrundum standard based on the identical intrumental setting. Unless a good standard peaks for each of the perovskite peaks (close to the actual XRD peak) is used, then doing the strain calculation artificially enlarges the calculated crystallite size and provide a larger error than just leaving out the strain calculation entirely. Therefore, we excludes the contribution of lattice strain to estimate the crystallite size in correlation with the diffusion length result.

2.8.5 Electron beam induced current (EBIC)

The samples for the EBIC measurement were prepared by depositing halide perovskite films on metal electrodes. Gold (Au) and Titanium (Ti) fingers with 2 mm spacing in between them were fabricated using two steps of photolithography. The procedure of thin-film deposition was the same as that used to prepare the films for the optical grating measurement (see sample preparation protocol). The contacts were wire-bonded to a printed circuit board, allowing the current of the perovskite films to be measured inside the SEM. The SEM used for the imaging is FEI Verios 460. The EBIC measurement was performed in the SEM as used for imaging, equipped with a current amplifier (FEMTO, DLPCA-200, gain set to $\sim 10^{11}$ - 10^{9} V/A), and the electron beam was set at 10kV, 10pA, 1 ms integration time. To roughly estimate the electron trajectory, therefore interaction volume, for the given electron beam parameters entering our structure, we used a Monte Carlo simulation of the electron's trajectory (CASINO) in the solid with 10^6 simulated electron [34]. To extract the photcurrent decay curves, the periodic noise from the EBIC maps was removed by filtering the image in Fourier space, and the current decay profiles over a uniform region of the image were averaged. For the $MAPbI_3$ EBIC images, this region was typically the whole frame, while for the $MAPbBr_3$ EBIC images, smaller areas were used because of non-uniformity in the morphology of the film and charging effects.

To validate our SSPG measurements, we compared the diffusion lengths determined using the SSPG technique to diffusion lengths measured using EBIC, which is a well-established technique that also measures lateral diffusion length. EBIC measurements, however, measure only local diffusion length (nm to μm scale), while SSPG measurements average over the entire film (mm scale).

According to our EBIC measurements, the diffusion lengths obtained from the current decay profiles in $MAPbI_3$ are 555 nm (**Figure 2.12e**), 512 nm, 454 nm, 518 nm, and 371 nm, as compared to the 490 ± 24 nm measured by the SSPG technique. This range of extracted diffusion length values likely originated from a local difference in crystallinity and film morphology. For the $MAPbBr_3$, EBIC-measured diffusion lengths included 215 nm (**Figure 2.12f-h**), 164 nm, 219 nm, 128 nm, 172 nm, 186 nm, and 318 nm, as compared to 201 ± 2 nm measured using SSPG. The average values (491 nm and 200 nm for $MAPbI_3$ and $MAPbBr_3$, respectively). For EBIC, the standard deviation is much larger (62 nm and 56 nm for $MAPb_3$, and $MAPbBr_3$, resepectively), as expected, because of the more local nature of the EBIC measurement. Since EBIC is a well-established technique, these measurements confirm that SSPG provides an accurate measurement of the film's lateral diffusion length averaged over a large scale.

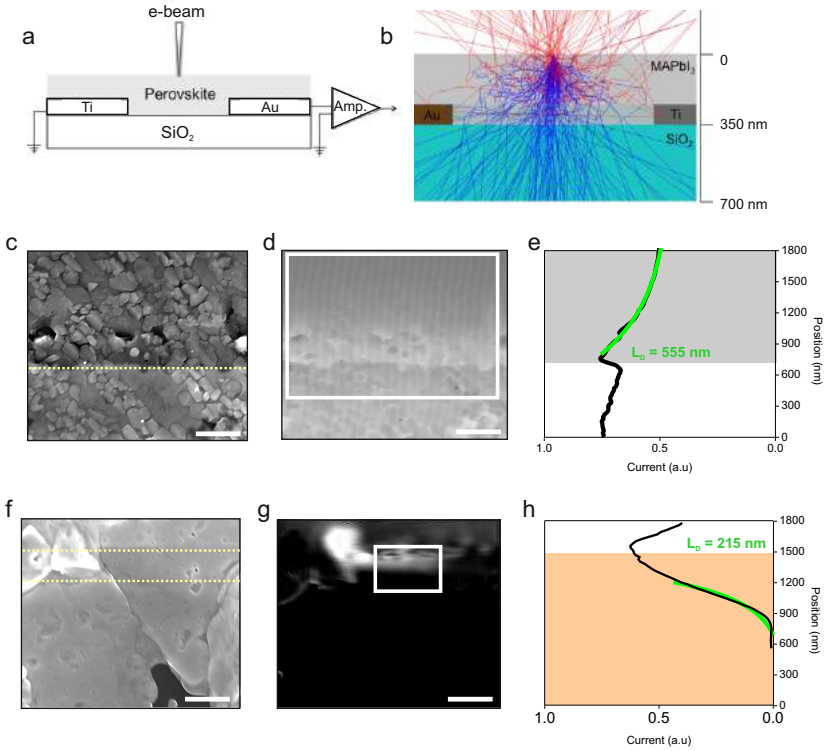

Figure 2.12: Electron beam induced current (EBIC) on $MAPbI_3$ and $MAPbBr_3$ films: **(a)** Measurement geometry. **(b)** Simulated electron trajectories and scattering events of the corresponding geometry in **figure 2.12a** (blue: secondary electron path; red: back-scattered electron path). **(c)** SEM image showing $MAPbI_3$ films on top of Au (bottom side; below the blue dashed-line) and Ti (beyond the top of the frame) contacts. **(d)** Corresponding EBIC image of **figure 2.12c**: darker areas indicate lower current; the scale bar for **figure 2.12c-d** is 400 nm. **(e)** Averaged current response profile from the EBIC extracted from **figure 2.12d** (framed with white line) showing an exponential decay tail toward the Ti side (gray area) of the depletion region (the green line is the fitting curve from which the diffusion length is obtained; L_D = 555 nm). **(f)** SEM image showing $MAPbBr_3$ films on top of Au (bottom side; below the bottom blue dashed-line) and Ti (top side; above the top blue dashed-line) contacts. **(g)** Corresponding EBIC image of **figure 2.12f**: darker areas indicated lower current; the scale bar for **figure 2.12f-g** is 2 μm. **(h)** Averaged current response profile from the EBIC extracted from **figure 2.12g** (framed with white line) showing an exponential decay tail toward the Au side (orange area) of the depletion region (the green line is the fitting curve from which the diffusion length is obtained; L_D = 215 nm).

In our EBIC measurements, we needed a relatively high voltage (10 kV) and current (50 pA) to measure a clear EBIC signal. This voltage ensures that the electron beam penetration depth is sufficient for the back electrodes can collect the signal (**Figure 2.12b**). We are aware that others have advocated using a lower voltage (1 - 3 kV) to prevent film damage over time for halide perovskite [35], but we did not see visible damage to our films with repeated scans. The instability reported in the literature could arise from the film's being damaged by preparing the cross section or from the use of transporting layer (e.g Spiro-OMeTAD) in the device. In our case, to give a structure comparable to that used for the SSPG measurements, we did not use any transporting layer, relaying on the barrier between the metal contact and the perovskite to produce a Schottky contact at which to measure th photocurrent's decay.

References

[1] M. M. Lee, J. Teuscher, T. Miyasaka, T. N. Murakami, and H. .J. Snaith, *Efficient hybrid solar cells based on meso-superstructured organometal halide perovskites*, Science **338**, 643 (2012).

[2] J. H. Noh, S. H. Im, J. H. Hoe, T. N. Mandal, and S. I. Soek, *Chemical management for colorful, efficient, and stable inorganic- organic hybrid nanostructured solar cells*, Nano Lett. **13**, 1764 (2013).

[3] N. J. Jeon, J. H. Noh, W. S. Yang, Y. C Kim, S. Ryu, J. Seo, and S. I. Soek, *Compositional engineering of perovskite materials for high- performance solar cells*, Nature **517**, 476 (2015).

[4] H. Zhu, Y. Fu, F. Meng, X. Wu, Z. Gong, Q. Ding, M. V. Gustafsson, M. T. Trinh, S. Jin, and X. Y. Zhu, *Lead halide perovskite nanowire lasers with low lasing thresholds and high quality factors*, Nat. Mater. **14**, 636 (2015).

[5] J. Burschka, N. Pellet, S. J. Moon, R. Humphry-Baker, P. Gao, M. K. Nazeeruddin, and M. K. Grätzel, *Sequential deposition as a route to high-performance perovskite-sensitized solar cells*, Nature **499**, 316 (2013).

[6] S. D. Stranks, G. E. Eperon, G. Grancini, C. Menelaou, M. J. P. Alcocer, T. Leijtens, L. M. Herz, A. Petrozza, and H. J. Snaith, *Electron-hole diffusion lengths exceeding 1 micrometer in an organometal trihalide perovskite absorber*, Science **342**, 341 (2013).

[7] N. J. Jeon, J. H. Noh, Y. C. Kim, W. S. Yang, S. Ryu, and S. I. Seok, *Solvent engineering for high-performance inorganic-organic hybrid perovskite solar cells*, Nat.Mater. **13**, 897 (2014).

[8] G. Xing, N. Mathews, N. Sun, S. S. Lim, Y. M. Lam, M. Grätzel, S. Mhaisalkar, and T. C. Sum, *Long-range balanced electron-and hole- transport lengths in organic-inorganic* $CH_3NH_3PbI_3$, Science **342**, 344 (2013).

[9] S. Komuro, Y. Aoyagi, Y. Segawa, S. Namba, A. Masuyama, H. Okamoto, and Y. Hamakawa, *Study of optically induced degradation of conductivity in hydrogeneted amorphous silicon by transient grating method*, Appl. Phys. Lett. **42**, 807 (1983).

[10] D. Ritter, E. Zeldov, K. Weiser, *Steady-state photocarrier grating technique for diffusion length measurement in photo- conductive insulators*, Appl. Phys. Lett. **53**, 992 (1988).

[11] I. Balberg, A. E. Delahoy, and H. A. Weakliem, *Ambipolar diffusion length measurements on hydrogenated amorphous silicon p- i -n structures*, App. Phys. Let. **53**,1949 (1988).

[12] J. P. Nicholson, *Fresnel corrections to measurements of ambipolar diffusion length*, J. Appl. Phys. **88**, 4693 (2000).

[13] K. Hattori, H. Okamoto, and Y. Hamakawa, *Theory of the steady- state-photocarrier-grating technique for obtaining accurate diffusion- length measurements in amorphous silicon*, Phys. Rev. B: Condens. Matter Mater. Phys. **45**, 1126 (1992).

[14] J. H. Hoe, D. H. Song, H. J. Han, S. Y. Kim, D. Kim, H. Kim, T. K. Shin, T. K. Ahn, C. Wolf, T. W. Lee, and S. H. Im, *Planar $CH_3NH_3PbI_3$ perovskite solar cells with constant 17.2% average power conversion efficiency irrespective of the scan rate*, Adv. Mater. **27**, 3424 (2015).

[15] Y. Yang, Y. Han, M. Yang, S. Choi, K. Zhu, J. M. Luther, and M. C. Beard, *Low surface recombination velocity in solution-grown $CH_3NH_3PbBr_3$ perovskite single crystal*, Nat. Commun. **6**, 7961 (2015).

[16] C. Quarti, E. Mosconi, J. M. Ball, V. D. Innocenzo, C. Tao, S. Pathak, H. J. Snaith, A. Petrozza, and F. De Angelis, *Structural and optical properties of methylamaonium lead iodide across the tetragonal to cubic phase transition: implications for perovskite solar cells*, Energy Environ. Sci. **9**, 155 (2016).

[17] C. Suryanarayana and M. G. Norton, *X-ray diffraction: a practical approach*, Plenum Press, New York, 1998.

[18] T. P. White, N. N. Lai, and K. R. Catchpole, *Tandem solar cells based on high-efficiency c-Si bottom cells: top cell requirements for > 30% efficiency*, IEEE J. Photovolt. **4**, 208 (2014).

[19] L. Gil-Escrig, A. Miquel-Sempere, M. Sessolo, and H. J. Bolink, *Mixed iodide-bromide methylammonium lead perovskite-based diodes for light emission and photovoltaics*, J. Phys. Chem. Lett. **6**, 3743 (2015).

[20] A. Sadhanala, F. Deschler, T. H. Thomas, S. E. Dutton, K. C. Goedel, F. C. Hanusch, M. Lai, U. Steiner, T. Bein, P. Docampo, D. Cahen, and R. H. Friend, *Preparation of single-phase films of $CH_3NH_3Pb(I_{1-x}Br_x)_3$ with sharp optical band edges*, J. Phys. Chem. Lett. **6**, 3743 (2015).

[21] S. A. Kulkarni, T. Baikie, P. P. Boix, N. Yantara, N. Mathews, and S. Mhaisalkar, *Band-gap tuning of lead halide perovskites using a sequential deposition process*, J. Mater. Chem. A **2**, 9221 (2014).

[22] H. Cho, S. -H. Jeong, M. -H. Park, Y. -H. Kim, C. Wolf, C. -L. Lee, J. H. Hoe, A. Sadhanala, N. Myoung, S. Yoo, S. H. Im, R. H. Friend, and T. -W. Lee, *Overcoming the electroluminescence efficiency limitations of perovskite light-emitting diodes*, Science A **350**, 1222 (2015).

[23] E. T. Hoke, D. J. Slotcavage, E. R. Dohner, A. R. Bowring, H. I. Karunadasa, and M. D. McGehee, *Reversible photo-induced trap formation in mixed-halide hybrid perovskites for photovoltaics*, Chem. Sci. **6**, 613 (2015).

[24] Y. Tian, M. Peter, E. Unger, M. Abdellah, K. Zheng, T. Pullerits, A. Yartsev, V. Sundstrom, and I. G. Scheblykin, *Mechanistic insights into perovskite photoluminescence enhancement: light curing with oxygen can boost yield thousandfold*, Phys. Chem. Chem. Phys. **17**, 24978 (2015).

[25] J. F. Galisteo-Lopez, M. Anaya, M. E. Calvo, and H. Miguez, *Environmental effects on the photophysics of organic-inorganic halide perovskites*, J. Phys. Chem. Lett. **6**, 2200 (2015).

[26] P. Peumans, A. Yakimov, and S. R. Forrest, *Small molecular weight organic thin-film photodetectors and solar cells*, J. Appl. Phys. **93**, 3693 (2003).

[27] G. F. Burkhard, E. T. Hoke, and M. D. McGehee, *Accounting for intergerence, scattering, and electrode absorption to make accurate internal quantum efficiency measurement in organic and other thin solar cells*, Adv. Mater. **22**, 3293 (2010).

[28] M. Haridim, K. Weiser, and H. Mell, *Use of the steady-state photocarrier-grating technique for the study of the surface recombination velocity of photocarriers and the homogeneity of hydrogenated amorphous silicon films*, Philos. Mag. B **67**, 171 (1993).

[29] S. Kato, Y. Kurokawa, S. Miyajima, Y. Watanabe, A. Yamada, Y. Ohta, Y. Niwa, and M. Hirota, *Improvement of carrier diffusion length in silicon nanowire arrays using atomic layer deposition*, Nanoscale Res. Lett. **8**, 361 (2013).

[30] B. Vermang, V. Fjallstrom, X. Gao, and M. Edoff, *Improved rear surface passivation of Cu(In,Ga)Se_2 solar cells: a combination of an Al_2O_3 rear surface passivation layer and nanosized local rear point contacts*, Nanoscale Res. Lett. **8**, 361 (2013).

[31] M. Law, L. E. Greene, A. Radenovic, T. Kuykendall, J. Liphardt, and P. Yang, *ZnO-Al_2O_3 and ZnO-TiO_2 core-shell nanowire dye- sensitized solar cells*, J. Phys. Chem. B **110**, 22652 (2006).

[32] P. -C. Hsu, H. Wu, T. J. Carney, M. T. McDowell, Y. Yang, E. C. Garnett, M. Li, L. Hu, and Y. Cui, *Passivation coating on electrospun copper nanofibers for stable transparent electrodes*, ACS Nano **6**, 5150 (2012).

[33] L. W. Veldhuizen, G. W. P. Adhyaksa, M. Theelen, E. C. Garnett, and R. E. I. Schropp, *Benchmarking photoactive thin-film materials using a laser-induced steady-state photocarrier grating*, Prog. Photovolt: Res. Appl. **25**, 605 (2017).

[34] H. N. Demers, N. Poirier-Demers, A. R. Couture, D. Joly, M. Guilmain, N. de Jonge, and D. Drouin, *Three-dimensional electron microscopy simulation with the CASINO Monte Carlo software*, Scanning. **33**, 92 (2011).

[35] H. Yuan, E. Debroye, K. Janssen, H. Naiki, C. Steuwe, G. Lu, M. Moris, E. Origiu, H. Uji, F. D. Schryver, P. Samori, J. Hofkens, and M. Roeffaers, *Degradation of methylammonium lead iodide perovskite structures through light and electron beam driven ion migration*, J. Phys. Chem. Lett. **7**, 561 (2016).

3

Identifying Grain Boundaries in Halide Perovskites

This Chapter describes the use of electron backscattering diffraction (EBSD) to properly determine the grain boundary locations in halide perovskite thin-films. Grain boundaries play a key role in the performance of thin-film optoelectronic devices and yet their effect in halide perovskite materials is still not understood. The biggest factor limiting progress is the inability to identify grain boundaries; the gold standard - EBSD - destroys halide perovskite thin films. Non-crystallographic techniques commonly misidentify grain boundaries, leading to conflicting literature reports about their influence. Here we solve this problem using a solid-state EBSD detector with 6,000 times higher sensitivity than the traditional phosphor screen and camera. We used the crystal misorientation data set from the EBSD to model the characteristics of grain boundary interface energy in $CH_3NH_3PbBr_3$ thin-film, and show that the halide perovskite grains do not exhibit twinning. In addition, we find a peculiar case, where the grain boundary very likely consists of amorphous halide perovskites.

3.1 Introduction

Minimizing non-radiative recombination is critical to achieving high efficiencies in optoelectronic devices. Halide perovskites are an emerging class of semiconductor whose optoelectronic properties are tolerant to defects [1, 2], relative to conventional

semiconductors. Although the trap density in polycrystalline perovskite films is typically 10^{14} - 10^{16} cm^{-3} (as high as fifty per million unit cells) [3, 4], their photovoltaic power-conversion efficiencies exceed 20 % [5]. Single-crystalline perovskites exhibit far lower trap densities (as low as 10^{10} cm^{-3}) [6], and this difference indicates that polycrystalline thin films posses additional sources of non-radiative recombination such as more bulk defects, less well-passivated surfaces, or grain boundaries.

To improve the efficiency of devices made from polycrystalline perovskites, it is necessary to push the trap density of these films to lower values, toward those reported for single crystals. To achieve this, we first must understand which of these sources of non-radiative recombination is most important to reduce, a task that is complicated by the conflicting reports regarding whether grain boundaries in halide perovskite films are beneficial or detrimental [7–9].

All of these studies on perovskite films have inferred the grain size and grain boundary locations based on optical or scanning electron microscope (SEM) images, which contain no crystallographic information. As we show below, the conflicting results regarding the role of grain boundaries can be explained by misidentification of the true position and nature of grain boundaries. Therefore, the first step toward understanding the complex effects of grain boundaries is quantifying their local crystallographic metrics. Traditionally, electron backscatter diffraction (EBSD) is the "gold" standard for measuring grain size, orientation and boundary location in thin-film samples. However, its use in halide perovskites has been hampered by beam-induced damage, making EBSD mapping impossible in thin-film samples so far. There has been one report of single spot EBSD measurements, which was limited to single crystals where grain boundaries cannot be studied [10].

Here we demonstrate a new type of solid-state EBSD detector with 6,000 times higher sensitivity than the traditional camera and phosphor screen to collect EBSD maps of grain size and orientation in $CH_3NH_3PbBr_3$ thin films. We developed a thin film deposition protocol that allows us to control the resulting average grain size over a large range between 1 and 60 μm. We show that the average grain size measured from EBSD is different (up to a factor of ~ 1.9) from what is inferred from optical and SEM images. The EBSD is not only necessary for proper identification of grain boundaries but also enables deeper insights from studying the dependence on misorientation angle, disorder at the interface, and heterogeneity in grain size.

3.2 Film formation

In order to systematically study grain boundaries, we developed a simple process that provided smooth, continuous thin films with average grain size tunable between 1 and 60 μm, depending only on the spin-coating time and speed. Instead of using the more common lead halide precursor, we used lead acetate trihydrate ($Pb(CH_3COO)_2.3H_2O$). Dissolving lead acetate in dimethylformamide (DMF) had previously produced continuous and highly oriented films of $CH_3NH_3PbBr_3$ [11]. We dissolve $Pb(CH_3COO)_2.3H_2O$ and CH_3NH_3Br instead in dimethylsulfoxide (DMSO)

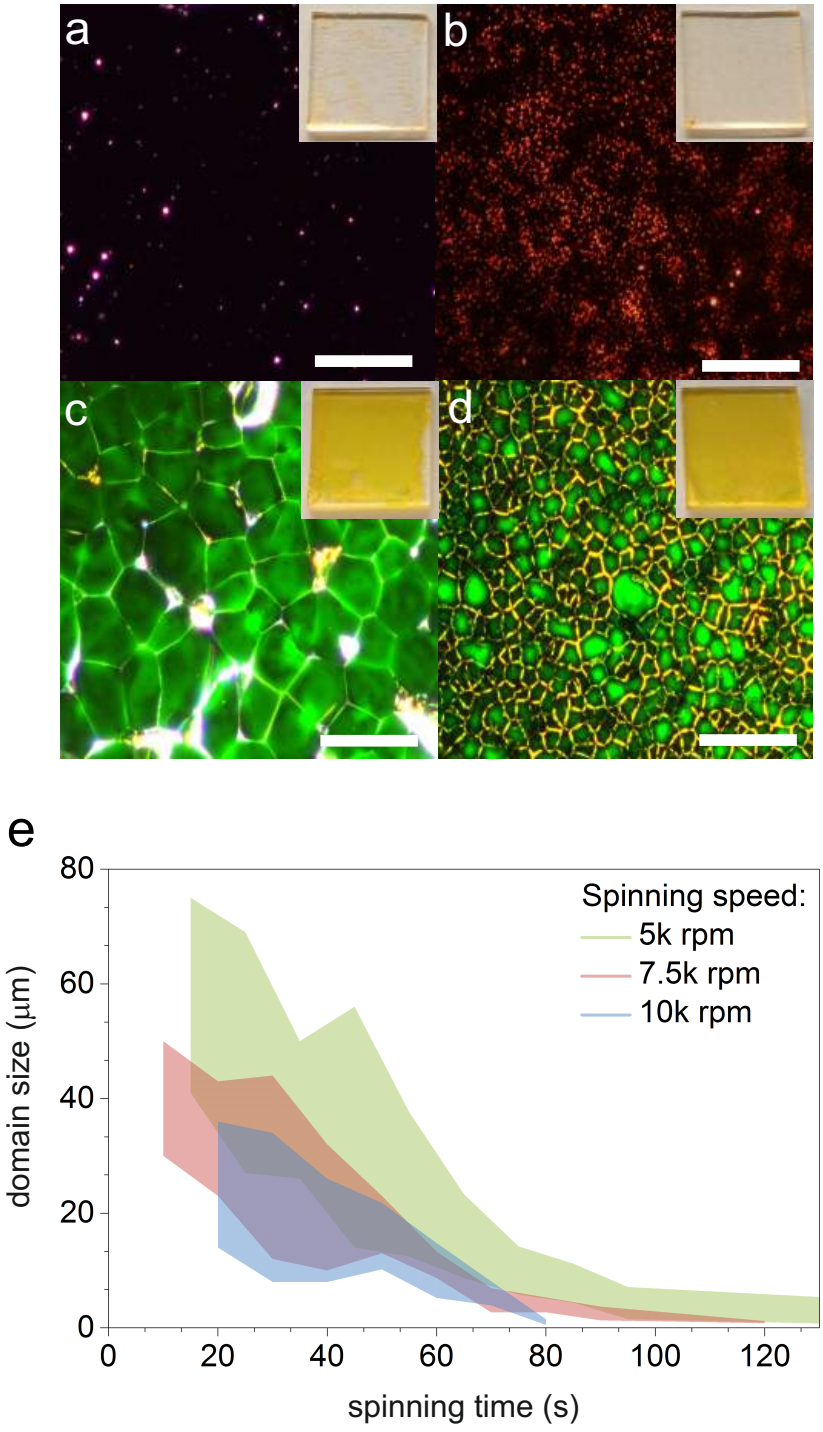

Figure 3.1: $CH_3NH_3PbBr_3$ perovskite film formation. Dark field optical images showing nucleation sites with short (**a**) and long (**b**) spinning time, and resulting films with short (**c**) and long (**d**) spinning time. The scale bars are 50 μm. The insets are photographs of wet intermediate films (**a** and **b**), and perovskite films (**c** and **d**) on glass substrates (each 15 mm × 15 mm). (**e**) domain size (pseudo-grain) statistics from optical microscopy versus spinning time with different spinning speeds. The spread of the areas represents a 95 % confidence interval.

in a 3.05 : 1 ratio. The spin-coating step determines the density of nuclei within the wet film of precursors and therefore the grain size of the resulting film: a shorter spin-coating duration produces fewer nuclei and larger grains. Scattering from the nuclei produced within the wet film is visible in dark-field optical images (**Figure 3.1a-b**). Given that intermediates are common in the halide perovskite literature [12–15] and our method does not produce perovskite without the subsequent annealing step, it is likely that these nuclei are a solvent-rich intermediate phase (details in Supporting information, **Figure 3.7**, and **3.8**).

During the annealing step at 90 °C over two hours, the nuclei become perovskite grains which merge into a continuous film. The density of grains in the resulting perovskite film correlates with the density of the initial nuclei in the precursor film (**Figure 3.1c-d**). Furthermore, the high concentration of solute ions in this wet film allows the perovskite to form before the film coalesces into isolated crystals. When a more dilute solution was used, islands of perovskite rather than a continuous film were formed. Although understanding the mechanism of film formation will require further study, this method successfully decouples the nucleation and growth steps of the film and therefore offers control over its final domain size (**Figure 3.1e**) on a variety of substrates such as glass, silicon, TiO_2, and ITO (**Figure 3.9**). Therefore, this method for making continuous, smooth thin-films with controlled domain size is a first step towards systematically studying the grain boundaries in halide perovskites using EBSD.

3.3 Grain boundary determination

We carried out EBSD measurements in an electron microscope that was equipped with a solid-state electron counting detector originally developed for mass spectrometry but now applied for electrons (**Figure 3.2a**) [16, 17]. The sensor is equipped with an electronic noise free circuit, and therefore provides high sensitivity and fast readout, which enable us to acquire clear EBSD maps of halide perovskite films on glass quickly before damaging the samples. We used an optimized beam current of 100 pA at an accelerating voltage of 30 kV, with a pixel dwell time of 100 ms. The electron dose needed for acquiring EBSD maps here is 6,000 times lower than what was previously necessary for single crystal samples using the traditional phosphor screen and camera (6 nA for 10s) [10]. Back-scattered electrons escape from the tilted sample and are projected onto the detector in a pattern of spherical bands that reflect the Bragg angles of the local crystal lattice (Kikuchi lines) [18]. By scanning the beam across the sample, we collected a pattern from each pixel and indexed it to the cubic $CH_3NH_3Br_3$ lattice to construct a map of the film's local crystallographic orientations (**Figure 3.2b**).

Figure 3.3a-d shows EBSD maps of the $CH_3NH_3PbBr_3$ perovskite prepared with different spinning times. It is evident that the grain size becomes larger with reduced spinning time (at a given spin speed), which is consistent with trends inferred from SEM (Top panel **Figure 3.3a-d**). Most crystal grains are oriented in the [001] direction. On samples with larger average grain size, however, the population becomes more

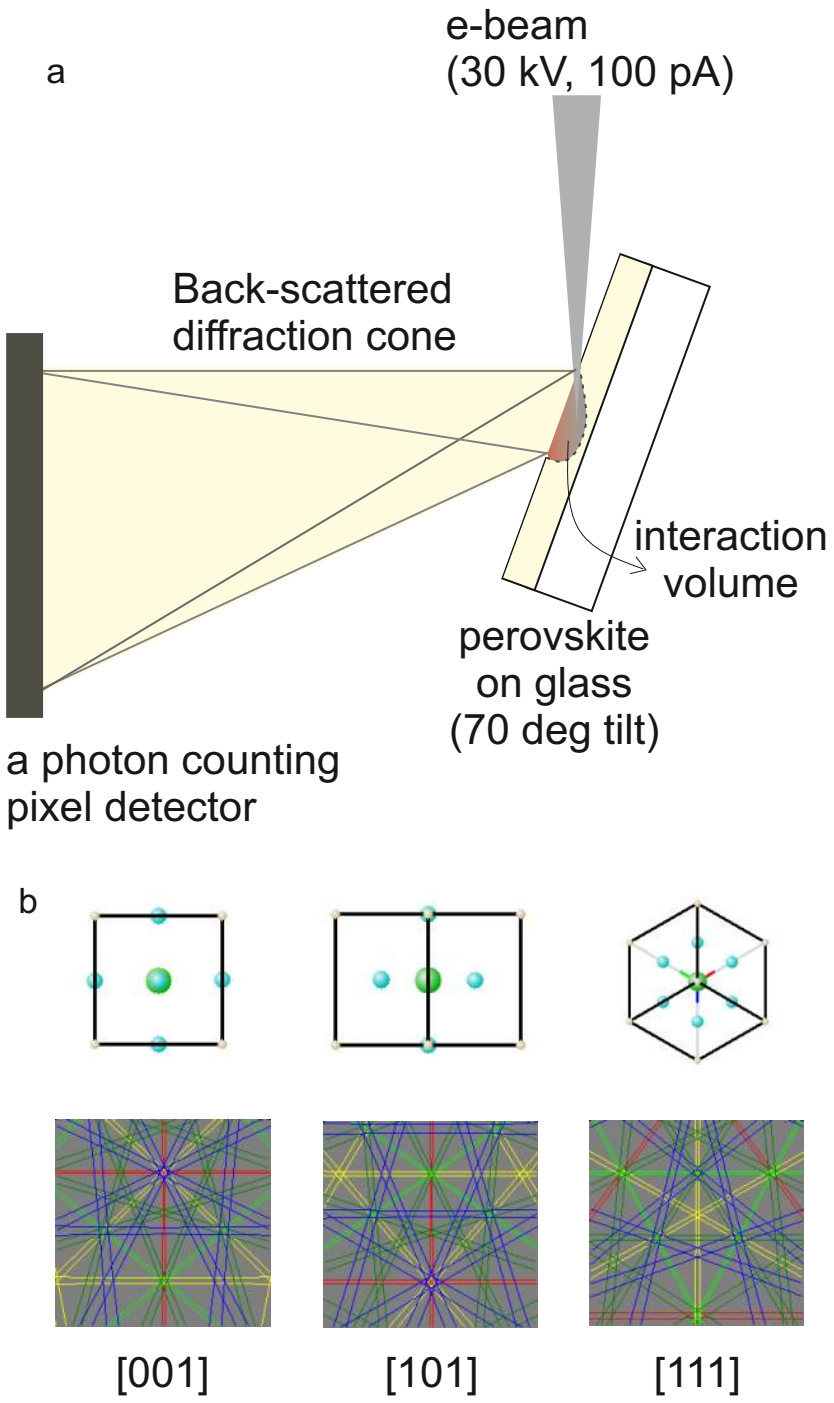

Figure 3.2: Electron backscattered diffraction (EBSD). (**a**) Schematic of our EBSD measurement. (**b**) Simulated Kikuchi patterns for cubic $CH_3NH_3Br_3$ lattice with [001], [101], and [111] crystal orientation.

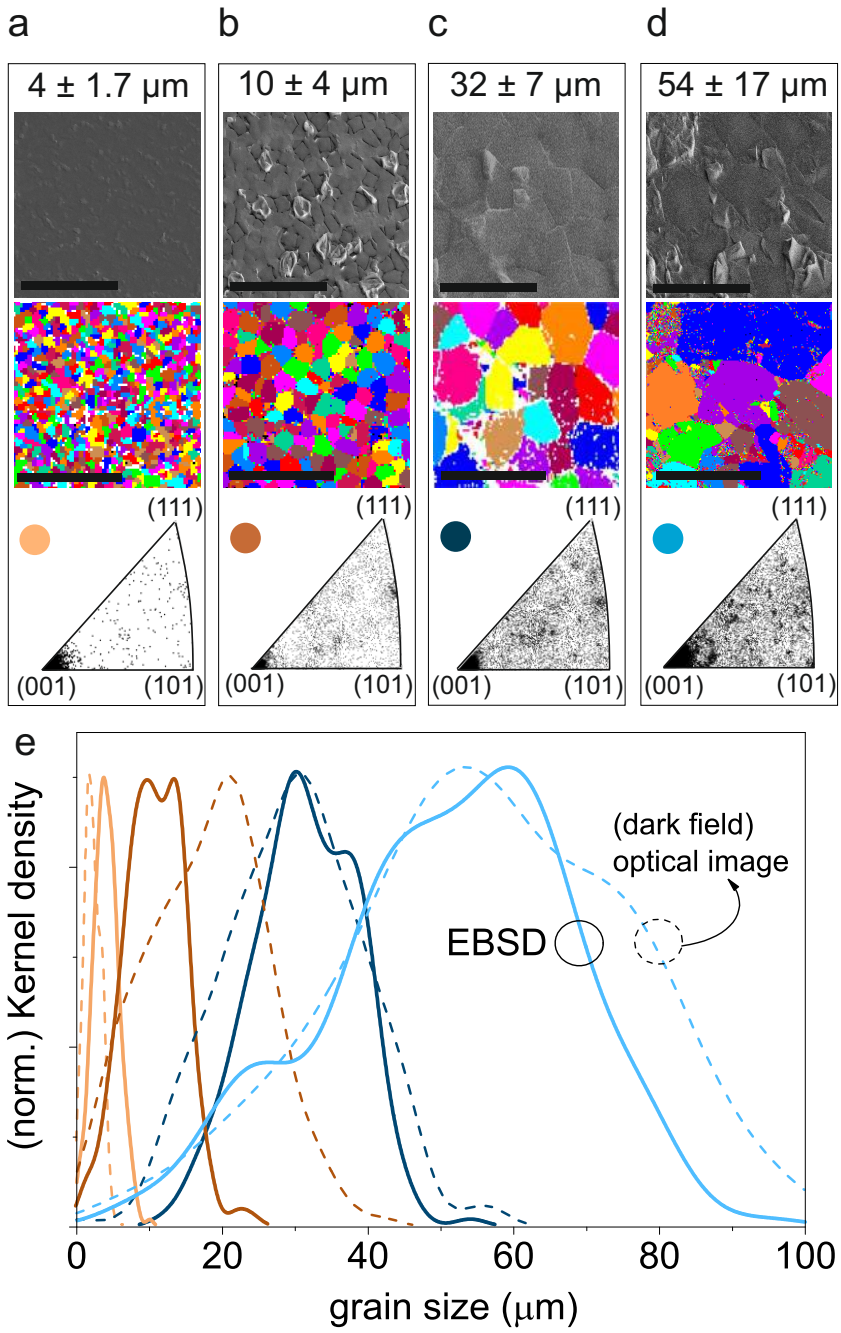

Figure 3.3: Collection of scanning electron-microscope (SEM) image (top panel) with its corresponding colour coded EBSD maps (middle panel), and distribution plot of crystallographic orientations (bottom panel) of perovskite films with 4 ± 1.7 μm (**a**), 10 ± 4 μm (**b**), 32 ± 7 μm (**c**), 54 ± 17 μm (**d**) grain sizes. The EBSD map for 32 ± 7 μm grain size shows disordered regions near the grain boundary (featured as a white colour coded). (e) Kernel density distribution of the grain size statistic (with a bandwidth of h = 0.337) [42] obtained from the EBSD compared with dark-field optical images. The size of the grains obtained from the optical images can be misleading (by a factor of up to 1.9).

dispersed to higher index orientations of [101] and [111] (the bottom panel) because of many smaller crystal grains trapped among adjacent larger grains. The mean of the distribution of apparent grain sizes obtained from optical images differs from the mean of the distribution obtained using EBSD (**Figure 3.3e**, the method in **Figure 3.10**). Typically the difference is less than 40 %, but in one particular case (brown trace), the optical images indicate an average grain size of more than a factor of 1.9 larger than the actual grain size.

Figure 3.4 shows the origin of this discrepancy between an SEM image and its corresponding EBSD map. Some pixels of the map show no Kikuchi pattern, for instance area **4**; this indicates a disordered region, which could contain amorphous (not fully crystallized) material [19], nanocrystalline perovskite with grains much smaller than our interaction volume (based on Monte Carlo simulation; **Figure 3.11**) or composite of the two. From EBSD data alone, we also cannot rule out the influence of surface roughness. The observation of disordered regions occurs primarily in the sample with an average grain size of 32 μm. In the optical image, such regions would be incorrectly classified as part of their neighboring grains. Furthermore, the identical

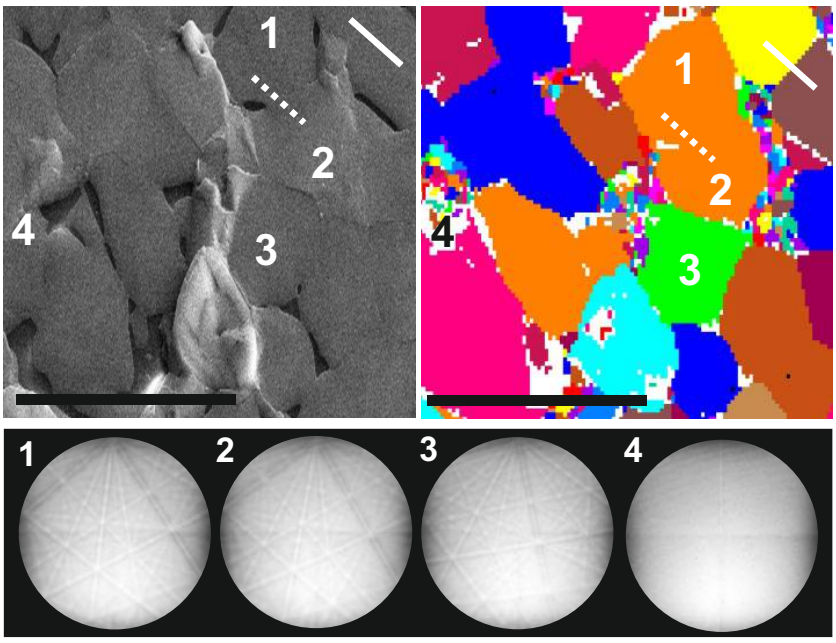

Figure 3.4: Deceiving features of grain boundaries showing two contrasting cases where the boundary that is visible under SEM (top-left panel; indicated by the white-dashed line) is not an actual grain boundary from the EBSD (see the corresponding EBSD maps; top-right panel); whereas within the apparent smooth grain under SEM (top-left panel; indicated by the white line), there is an invisible grain boundary (top-right panel); see the different colour maps under the EBSD). The bottom panel shows Kikuchi bands obtained by averaging multiple diffraction patterns per pixel within one scanning area (~200 - 600 pixels). The scanning areas **1** and **2** show identical Kikuchi bands, and this pattern is different than that of scanning area **3**. Scanning area **4** shows no distinct back-scattered diffraction. All scale bars are 50 μm.

Kikuchi patterns between domain **1** and **2** in **Figure 3.4** (across the dashed line) indicate that they are one grain, while their morphology (based on the SEM) suggests there is a grain boundary. In another area (solid line in Figure 2f), the SEM suggests there is no grain boundary but the EBSD map shows that one is present.

3.4 Amorphous grain boundary

To further resolve the origins of the disordered region at the grain boundary, we carried out synchrotron-based nanoprobe X-ray diffraction (nano-XRD) on the sample with <32 μm> grain size (details in the Supporting information, **Figure 3.14**, and **Figure 3.16**). On the basis of the nano-XRD analysis, the disordered grain boundary regions appear to be amorphous. **Figure 3.5** shows a region of grain boundaries where we detected neither scattering from oriented perovskite [001], nanocrystalline perovskite phase, intermediate phase, nor precursor traces of $PbBr_2$. Our nano-XRD scattering geometry cannot detect the presence of crystalline material with in-plane orientation ([101] or [111]), but since such orientations can be easily indexed from the EBSD maps, the disordered regions at the grain boundaries where we detect no EBSD nor

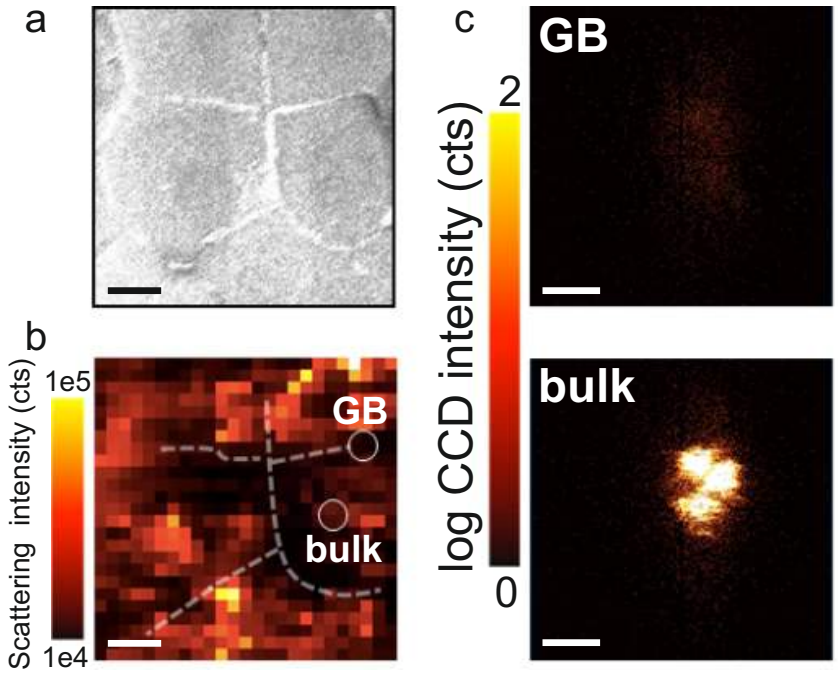

Figure 3.5: Amorphous grain boundaries probed using nano-XRD. (**a**) SEM image of grain boundary region. (**b**) Summed scattering intensity across the (002) $CH_3NH_3PbBr_3$ peak when rocking θ = 12.86 °, 13.47°, and 14.07° with 2θ fixed at 26.94°. The dashed lines are guides to the eye. Scale bars are 4 μm. (**c**) Diffraction pattern at the "GB" point highlighted in the scattering intensity map (**b**), and at the "bulk" point highlighted in the scattering intensity map. Scale bars 3 mrad. No intermediate or $PbBr_2$ phases were detected along the grain boundaries (**Figure 3.15**).

nano-diffraction intensity are likely to be amorphous perovskites.

3.5 Grain boundary characteristic

Little is known about the crystallographic nature of grain boundaries in halide perovskites; however, thermodynamically the main characteristics of grain boundaries can be inferred by their crystallographic misorientation angles which can be acquired from the EBSD [20–23]. Using crystallographic misorientation angles, we can calculate the interfacial energy among adjacent grain boundaries (details in the Supporting information, and **Figure 3.12**). For [001] crystal orientation (83 % of the $CH_3NH_3PbBr_3$ perovskite film studied here), the grain boundary interfacial energy increases with crystal misorientation angle up to 14°, but then fluctuates without a pronounced global minimum for samples with both the small (<4 μm>) and large (<54 μm>) grain size (**Figure 3.6**). A pronounced global minimum surface energy at high misorientation angle is typically associated with a special boundary, called coherent twinning (e.g. Σ3 or Σ5) which is often observed in other photovoltaic semiconductor materials (CdTe, chalcopyrite, InP, GaAs, and mc-Si) [24–28]. Removing twinning defects has been shown to improve solar cell performance [27, 28]. Although such twinning was previously found on $CsPbX_3$ (X = Cl, Br, I) perovskite nanocrystals [29], and $CH_3NH_3PbI_3$ thin film [30], we have not been able to observe it within the spatial resolution of our large-area EBSD mapping (83 nm), even on the higher index crystal

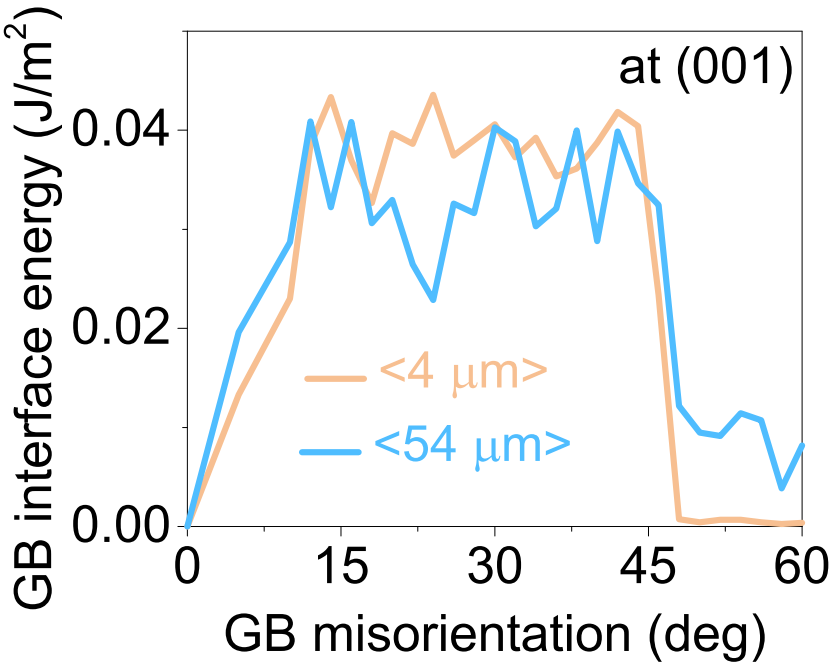

Figure 3.6: Grain boundary surface energy as a function of grain boundary misorientation for (001) crystal orientation and two grain sizes: <4 μm>, and <54 μm>.

orientation [101] and [111]. The absence of twinning itself in our films indicates that a higher excess interfacial energy at the grain boundary is always induced in order to equilibrate any general structural dislocation (further details of the consequence in the Supporting information, **Figure 3.13**).

3.6 Conclusions

In conclusion, here we show the first successful attempt of mapping crystal misorientation by means of electron backscattering diffraction (EBSD) technique in halide perovskite thin film. This should stimulate an advance toward microstructural characterization in such sensitive materials. We emphasize the importance of using a true crystallographic measurement when studying the grain boundaries in halide perovskite thin films. This is not only necessary for proper identification of grain boundaries but also enables deeper insights from studying dependence on misorientation angle, disorder at the interface, and heterogeneity in grain size. Using EBSD, we find that the $CH_3NH_3PbBr_3$ films lack crystal twinning. Interestingly, under certain conditions amorphous regions can form at the grain boundaries whose effects will be discussed in Chapter 4.

3.7 Supporting information

3.7.1 The role of the intermediate phase

The solution concentration was 6.15 M CH_3NH_3Br and 2 M $Pb(CH_3COO)_2.3H_2O$, and the solution was heated to 60°C for 30 minutes while stirring to ensure dissolution of the powders and then cooled to room temperature before use. Although the precursors can be temporarily dissolved in a concentrated solution, eventually white crystals form when the solution is left undisturbed for an extended period of time (several days to weeks, **Figure 3.7**). At this high concentration almost all of the solvent is

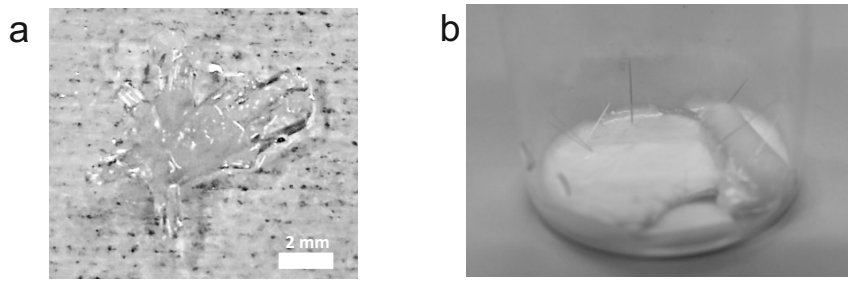

Figure 3.7: Intermediate crystal formation on $CH_3NH_3PbBr_3$ perovskite. (**a**) a gel form of the intermediate crystal phase where almost all of the solvent (DMSO) was used to form the gel phase. (**b**) a solution form of the intermediate crystal phase (6 M CH_3NH_3Br mixed with 2 M PbAc solution) after being left undisturbed for an extended amount of time (several days to weeks).

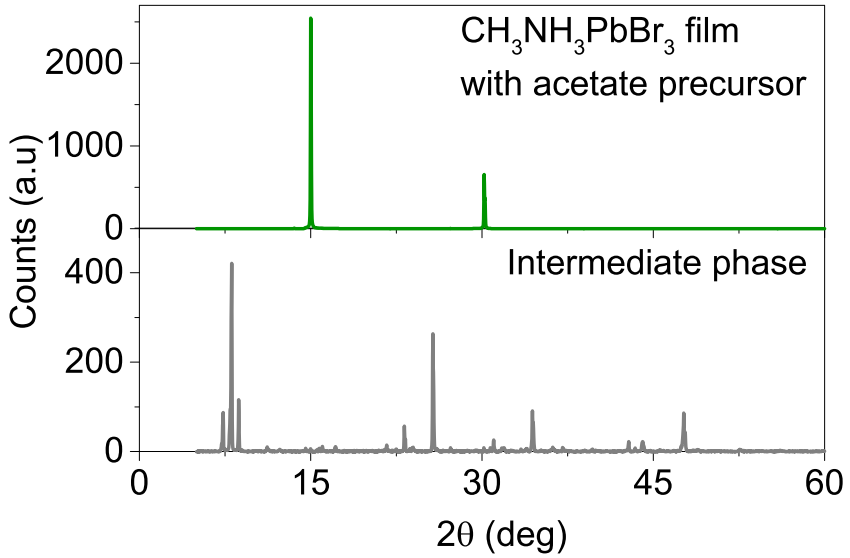

Figure 3.8: X-ray diffraction (Cu-Kα) showing low-angle peaks of the intermediate crystal powder compared to the typical XRD pattern of the final $CH_3NH_3PbBr_3$ perovskite film.

used up in the formation of these intermediate crystals, indicating that the solvent is also part of their structure. Low angle X-ray diffraction peaks of the polycrystalline intermediate support this conclusion (**Figure 3.8**). The highest concentration we tried was 10 M CH_3NH_3Br and 3.3 M $Pb(CH_3COO)_2.3H_2O$), and this was still not yet the limit. Similar behavior has been reported for intermediates formed during the deposition of $CH_3NH_3PbI_3$ thin films [12, 15]. These crystals, however, convert to the perovskite when removed from a solvent-rich environment (liquid or vapor), and higher temperatures accelerate this transformation. In our spin-coating method, the perovskite layer forms only during the annealing step, even after prolonged spinning, which suggests that crystals of a solvent-rich intermediate form during spin-coating and are later converted to the perovskite upon heating. This conclusion is supported by the fact that solvent- precursor interactions are observed to be particularly strong in this chemical system. The solubility of both precursors at room temperature increases when they are dissolved together. Separately each can be dissolved only up to only a 2 M concentration in DMSO.

3.7.2 Durability and practical limitation of the deposition method

Because of the high viscosity of the precursor solution, speeds between 5,000 to 10,000 rpm work best to generate a uniform film. Longer spin- coating duration yields denser nuclei and hence smaller domain sizes. Higher spin-coating speeds precipitate the nuclei faster for a given spin-coating duration, likely because more rapid evaporation of the solvent increases the supersaturation of the solution. We found that this method works on a variety of substrates such as glass, silicon, TiO_2, and ITO (**Figure 3.9**).

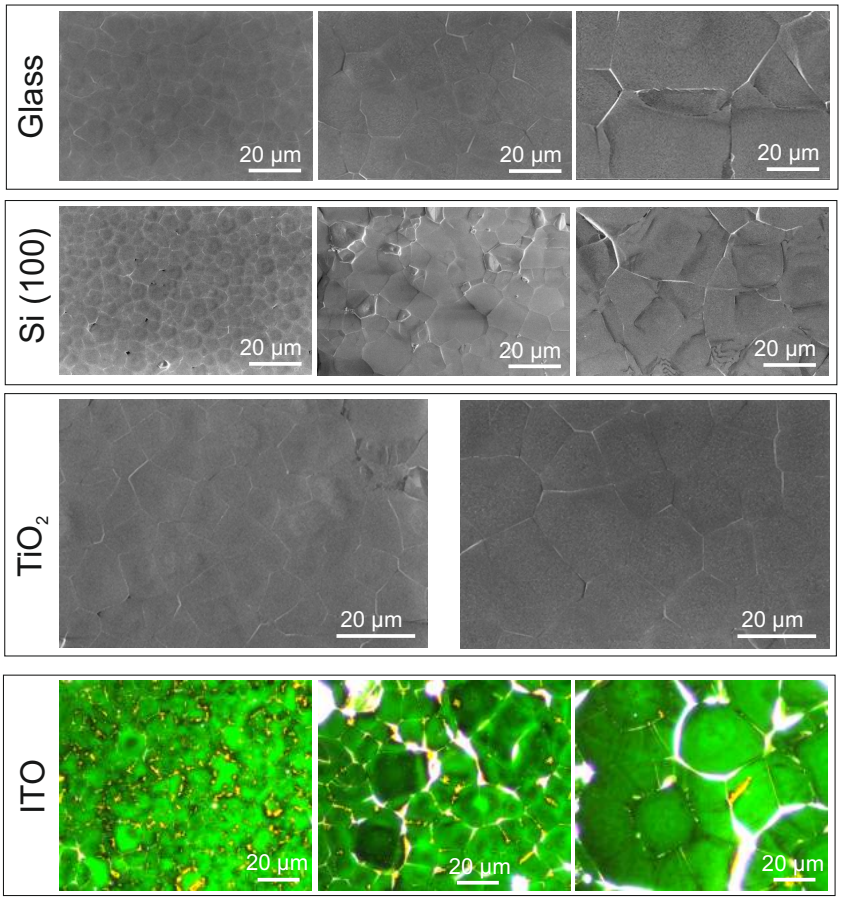

Figure 3.9: The efficacy of the controlled grain size method on different substrates. The top three panels show SEM images, while the bottom panel shows dark-field optical images.

Cleaning the surface to strong hydrophilicity is critical to produce continuous films, so pre-treatment of the substrate with piranha solution (containing a mixture of H_2SO_4 and H_2O_2 (3:1 volume ratio) at 120°C for 20 min) or an aggressive oxygen plasma (O_2 plasma descum for 10 minutes at 75 W) is required. This method offers the ability to tune the grain size of $CH_3NH_3PbBr_3$ films on substrates that are relevant for device applications. The method for determining the domain size (pseudo-grain) as well as the actual grain size will be discussed in the following sub-section (*Grain size reconstruction*, **Figure 3.10**).

3.7.3 Sample preparation for the EBSD measurement

The sample is perovskite film on glass. On top of the film, 100 nm thick gold (Au) metal pads are deposited by thermal evaporation. The separation between two gold pads is 0.6 mm where the EBSD was performed. The metal pads were grounded using copper tape. The electron beam was set to up to 100 pA, 30 keV with 9.3 mm working distance, and

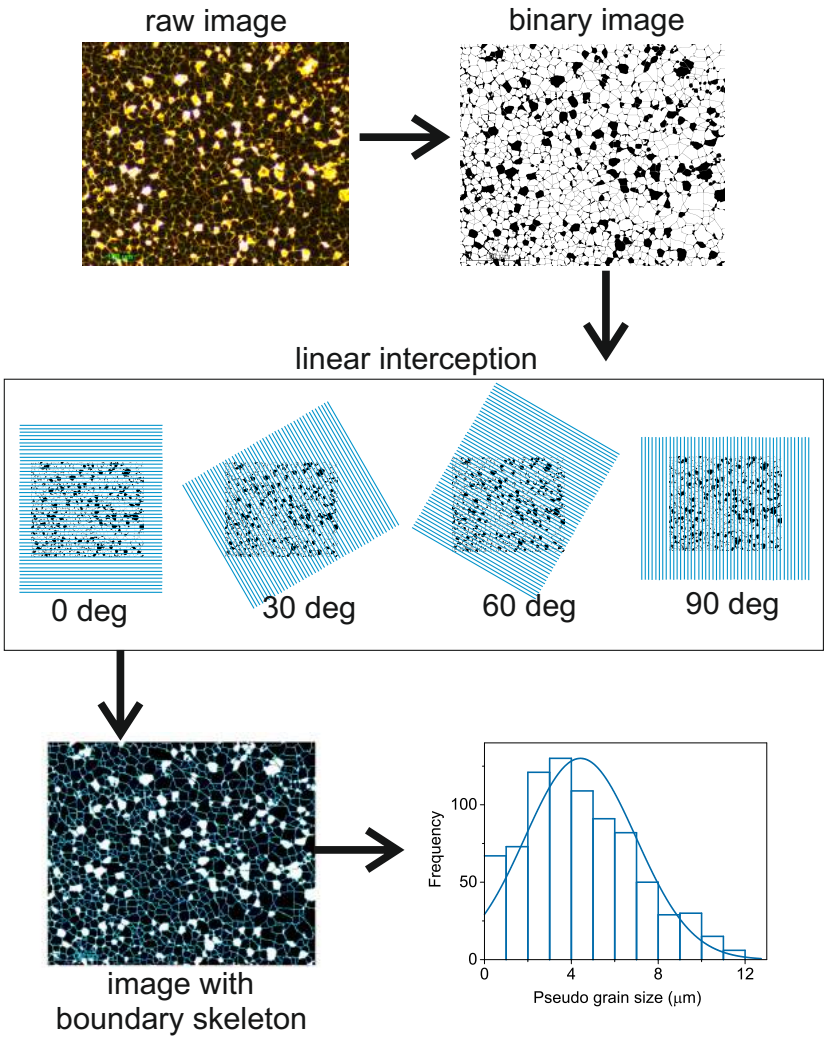

Figure 3.10: Procedure to determine the apparent grain size from the optical image, as well as for the actual grain from EBSD map.

hits at 70° tilted with respect to the sample surface. With this condition, we estimate the beam diameter is around 2 nm (Gaussian shape with landing position on the top sample surface), and based on Monte Carlo simulation (CASINO) [31], the penetration depth of interaction volume is around 250 nm after taking into account depth-dose function correction [43, 44]. Note that this interaction volume is justified when only 12.5 % of the initial energy from the electron beam remained. The penetration depth is around half compared to the normal incident geometry, which indicates that the EBSD geometry is more surface sensitive (**Figure 3.11a-b**). Therefore the escape probability of the back-scattered electron within this depth becomes higher for the EBSD geometry (**Figure 3.11e-f**). The escape probability (determines the contrast images for acquiring the EBSD) can reduce because of scattering from grain boundaries, and surface roughness. **Figure 3.11c-d** show gradual reduction of lateral back-scattered

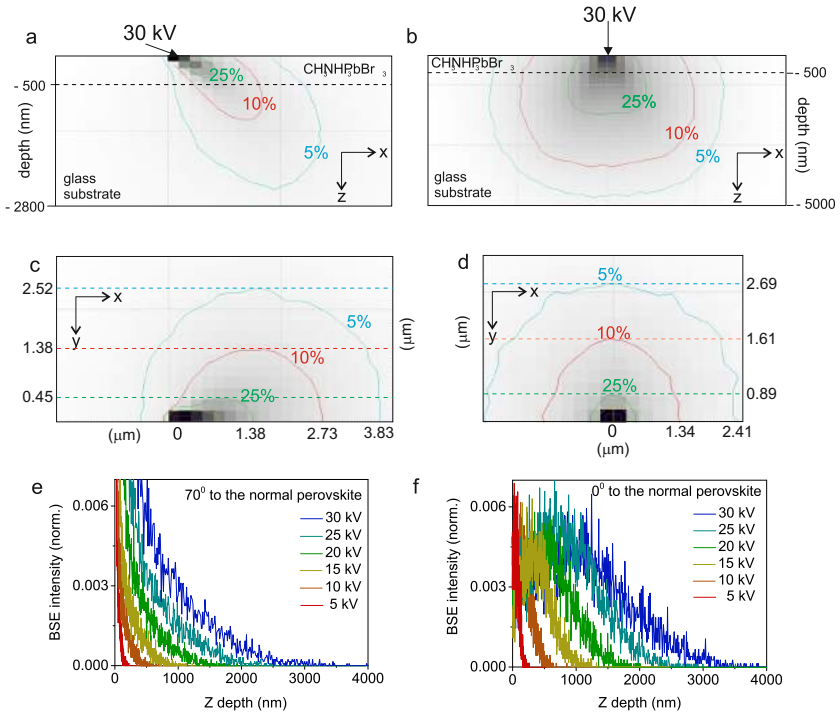

Figure 3.11: Simulated interaction volume between electron beam and $CH_3NH_3PbBr_3$ perovskite. X-Z depth profile of back-scattered electron beam energy at 70° tilted sample (**a**), and 0° tilted sample (**b**). X-Y plane profile of back-scattered electron beam energy at 70° tilted sample (**c**), and 0° tilted sample (**d**). Back-scattered electron (BSE) intensity decay as a function of the perovskite Z depth at 70° tilted sample (**e**), and 0° tilted sample (**f**) showing at 70° tilted sample (the EBSD geometry) is more surface sensitive, but with higher probability of having BSE escaping from the perovskite surface. All simulations were carried out using Monte Carlo based simulator (CASINO).

energy means increasing interaction volume) over the distance away from the landing position of the electron beam (0,0). Hypothetical dimensions of grain boundaries, or surface roughness (e.g. grooves) are indicated by the colored dashed line to provide an intuitive account of the percentage of image quality losses during the EBSD orientation mapping. For example, if the average grain size is 0.45 μm, then the image quality can reduce by 25 % because of the reduced surface interaction volume. However, it depends on a number of trajectories of electron beam hitting the grain boundaries. When the electron beam hits the grain boundaries in which the frequency is higher compared to the surface interaction volume, the EBSD patterns across the nighbouring grains cannot be discerned (failure of indexing), unless an image processing technique can decouple them. The image per pixel was collected using EDAX OIM software where in conjunction to this we use *Python code* to accelerate the image processing time. The Kikuchi patterns were indexed based on cubic $CH_3NH_3PbBr_3$ perovskite (a = 5.922 Å). The mapping step size in our measurement is typically up to 1 μm with a grain tolerance angle set to 1-3°. A narrower step size is possible, however

quite often we observed a higher dose level per unit area would degrade the halide perovskite samples. For a successful EBSD mapping, the narrowest step size that we have examined on our sample is 100 nm (~16.6 nm kernel resolution, **Figure 3.14**). Also, note that various factors might affect discrepancies to properly reconstruct the misorientation grain mapping (details discussion in the subsection *Disorder at the grain boundaries*, **Figure 3.14**).

3.7.4 Grain size reconstruction

We follow standard test methods (ASTM E112-13) for determining average grain size [32, 33]. First we converted the image into a binary type file until an appropriate skeleton of the grain boundary is distinguished. Next, we created a grid in four different orientation on top of the images. The idea of using grids with different orientations is to accommodate as many intersection points as possible between the grids and the boundary skeletons (contrast lines) of the binary image. Therefore we can reconstruct the area of every grain, whose square-root is used to determine the grain size; this model is valid only when the overall grain aspect ratios are nearly 1 to 1 in the x-y plane, which is the case for all $CH_3NH_3PbBr_3$ perovskite studied here. The orientations of the grids

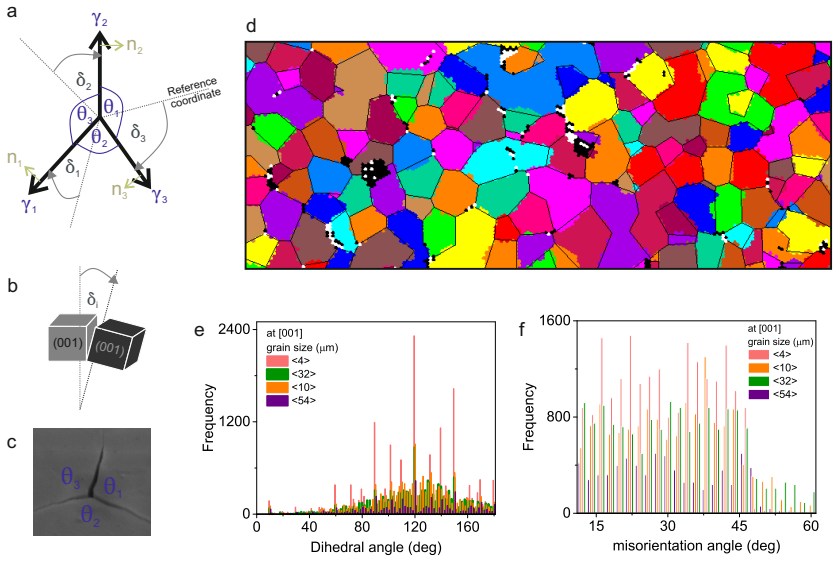

Figure 3.12: Grain boundary reconstruction. (**a**) The coordinate system for triple-points showing the dihedral angle (θ) between two adjacent grain boundaries, and misorientation angle (δ) between a grain boundary and its reference coordinate (coincidence site lattice). (**b**) illustration for the misorientation angle between two unit pixels having identical crystal orientation whose symmetry breaks at δ~60°. (**c**) SEM image showing three $CH_3NH_3PbBr_3$ perovskite grains (001) with their grain boundary triple point. (**d**) One example of grain boundary segmentation on an EBSD map from which multiple dihedral and misorientation angles were generated. Statistics showing dihedral angle (**e**) and misorientation angle (f) over the sample with different grain sizes studied here.

are 0°, 30°, 60°, and 90° orientation relative to the image coordinate. Each orientation of grid has multiple lines with interval 3 times less than the pixel size (assuming the pixel size is cubic; and this applies even better even if the actual pixel is hexagonal, in this routine we typically set 0.75306 pixels/μm). At least 5000 measurements per image are required, and preferably over 20000 for more accurate distribution analysis. The analysis and routine is done using *Python code*. Schematic of the reconstruction flow is shown in **Figure 3.10**.

3.7.5 Grain boundary energy calculation

According to the EBSD map, all crystal grains of $CH_3NH_3PbBr_3$ perovskite do not pose any strong anisotropic shape, so thermodynamically we can associate relative excess free energy based on local force balance (local minimum) created at every triple junction of the grain boundary (**Figure 3.12a-c**). The three angles (called dihedral angle) created at the triple junction are associated with their surrounding grain boundary surface energy whose vector sum of the normal force must be zero (Herring's law) [20, 34]. We then can use the classical sine law of Young's equation to determine the interfacial energy

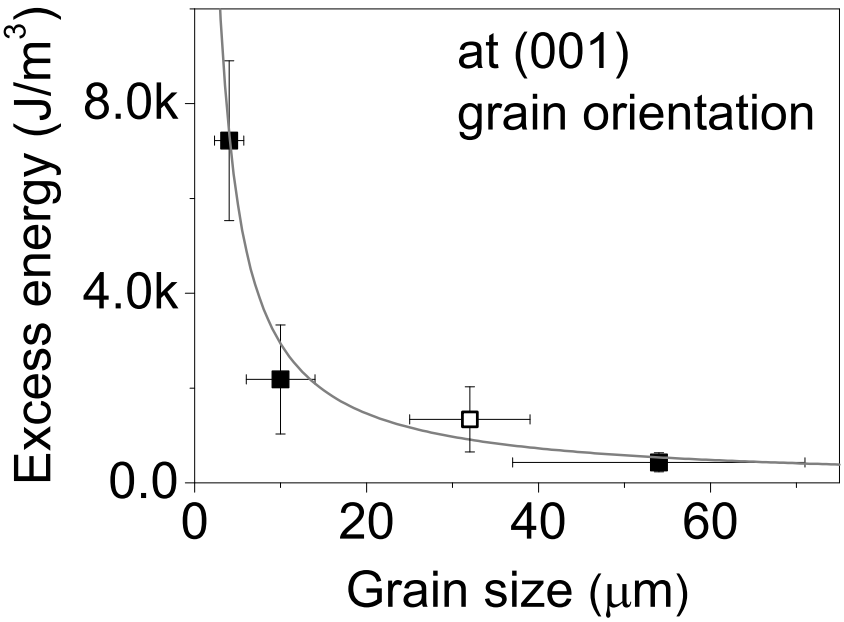

Figure 3.13: Total volumetric excess energy at the grain boundary. Total excess energy (stored energy) as a function of grain size at (001) crystal symmetry which fits well with an exponential decay line. The white square data (<32 μm> grain) indicates that the grain boundarys segmentation is not perfect because of the amorphous region present at the grain boundary (**Figure 3.14**).

of each boundary. At one triple junction it can be expressed as three linear equations:

$$\begin{bmatrix} \sin\theta_2 & -\sin\theta_1 & 0 \\ \sin\theta_3 & 0 & -\sin\theta_1 \\ 0 & \sin\theta_3 & -\sin\theta_2 \end{bmatrix} . \begin{bmatrix} \gamma_1 \\ \gamma_2 \\ \gamma_3 \end{bmatrix} = \begin{bmatrix} 0 \\ 0 \\ 0 \end{bmatrix} \tag{3.1}$$

Once multiple triple junctions are connected, a larger matrix will be created. We can express that as a sum of linear combination equation:

$$\sum_{j=1}^{N} \left[M_{i,j}\right]\left[\gamma_i\right] = \left[b_i\right]; i = 1,2,3,...N(N-1)/2 \tag{3.2}$$

where M is the combined matrix,γ is the grain boundary interfacial energy, j is the ordering number for the grain boundary with total number of N, and i is the ordering of the triple junction with total number of N(N-1)/2, and b_i is the residual of the sum. The grain boundary lines can be acquired from the EBSD map and reconstructed using *EDAX OIM*^{TM} *Analysis* software where we used Kernel method pattern analysis for a better segmentation result (**Figure 3.12d**). For one type of grain size sample, we typically generate around 18000 sets of triple junctions (**Figure 3.12e**). First we sorted the triple junctions based on crystallographic orientation; in this case, the crystals are mainly orientated in the (001) direction. Next, we sorted the triple junctions based on their crystal misorientation angle (**Figure 3.12f**). It measures how much the grain is tilted relative to the local reference frame of crystalline lattice (unit cell). The misorientation angle is binned and averaged to 2° intervals within the 0° to 60° range. Since every segmented grain boundary is connected with its adjacent four boundaries and two triple junctions, an overdetermined matrix system is created. So, in order to avoid highly symmetric system of linear equations, we used the Kaczmarz's iteration method on every row of the matrix in the equation 3.2, which is then projected to equation 3.3. For example, if the initial guess of the (γ_1, γ_2) is ($\gamma_1{}^0$, $\gamma_2{}^0$) then the successive solution is ($\gamma_1{}^1$, $\gamma_2{}^1$) where:

$$\gamma_1^1 = \gamma_1^0 + (\sin\theta_2)\,\frac{r}{(\sin\theta_2)^2 + (\sin\theta_1)^2} \tag{3.3}$$

$$\gamma_2^1 = -\gamma_1^0 + (\sin\theta_1)\,\frac{r}{(\sin\theta_2)^2 + (\sin\theta_1)^2} \tag{3.4}$$

$$r = b_i - (\sin\theta_2)\,\gamma_1^0 - (\sin\theta_1)\,\gamma_2^0 \tag{3.5}$$

We justified equation 3.3 to be converged at ${\gamma_j}^k$ where k is large enough (typically less than 1000 in this work) with residual less |0.00005|. The iteration routine was carried out using *Python code*. Since every step of the iteration is a projection of the previous one, the grain boundary surface energy (γ_j) is a normalized value. We converted the normalized values into a more quantitative approximation based on the grain boundary surface energy values at misorientation angle below 12° using Read-Shockley's model [21].

$$\gamma_j = \left[\frac{G.a}{4\pi\,(1-\sigma)}\right]\theta_j\left[0.23 - \ln\theta_j\right] \tag{3.6}$$

where G is the experimentally measured sheer modulus (10.4 GPa), a is lattice constant, and σ is Poisson's ratio (0.29) of bulk single crystal $CH_3NH_3PbBr_3$ perovskite [35, 36]. To estimate the microscopic impact of averaged grain size on the grain boundary energy, we calculated the volumetric excess energy as a function of grain size average grain boundary energy (also known as a stored energy, E_G) as [22, 23, 37]:

$$E_G \simeq \frac{\left[\gamma_m\left(\frac{\theta}{\theta_m}\right)\left(1-\ln\left(\frac{\theta}{\theta_m}\right)\right)\right]}{\overline{D}} \tag{3.7}$$

where γ_m is high angle grain boundary surface energy, θ is the grain misorientation, θ_m is the misorientation angle characteristic above which the grain boundary surface energy is independent of misorientation angle, and $\overline{D}$ is average grain size based on EBSD. We used Rayleigh's distribution to calculate the propagating error on the resulting E_G by considering the randomly scattered interfacial energy with misorientation angle (although it could be due to systematic coincidence site lattices). This is essentially the driving force for migration for the recrystallization grains, higher stored energy means higher mobility toward deformation to equilibrate the excess grain boundary interfacial free energy to accommodate a mechanical strain [21–23, 37]. It shows that the total excess energy decreases exponentially with grain size in $CH_3NH_3PbBr_3$ perovskite (**Figure 3.13**). If we can associate this volumetric excess energy at the grain boundary, then its evolution could appear as several phenomena, such as ionic conduction pathways, active adsorption sites, or space charge segregation; all of which should be responsible for the non-radiative recombination losses [38–40].

3.7.6 Disorder at the grain boundaries

There are at least three possible situations that might generate the disordered regions (in the next subsection, Nano-XRD, confirmed as amorphous) that we observe in our EBSD mapping at grain boundaries: (1) surface roughness (e.g. a groove), (2) strong lattice strain, and (3) amorphous grain boundaries, all of which are pointed out in the ROIs in **Figure 3.14**. It is important to note that EBSD alone cannot rule out mechanism (1) and (2). Instead, we confirmed the presence of amorphous regions using synchrotron based nano-XRD (next subsection). We refer to the disordered region as all pixelated areas without any visible Kikuchi patterns. Interestingly, the disordered regions (white color pixels) were still visible even at a smaller step size (100 nm; 16 nm kernel resolution, and up to 3°) misorientation tolerance). In addition, a very large groove could block the emitted back-scattered electron from the shadowed film surface to the detector, and this results in a failure of pattern recognition (partial Kikuchi patterns). We rarely observed such an effect in our films, unless a huge milimeter-sized chunk happened to stick on the top surfaces. A transition from (001) crystal orientation to its higher index orientation (101) or (111) also generates a disordered region which correlates to a larger strain (the hot spot, **Figure 3.14d**), although this is not always the case. The synchrotron based nano-XRD is used to confirm the nature of "disordered" regions because factors (1) and (2) do not apply.

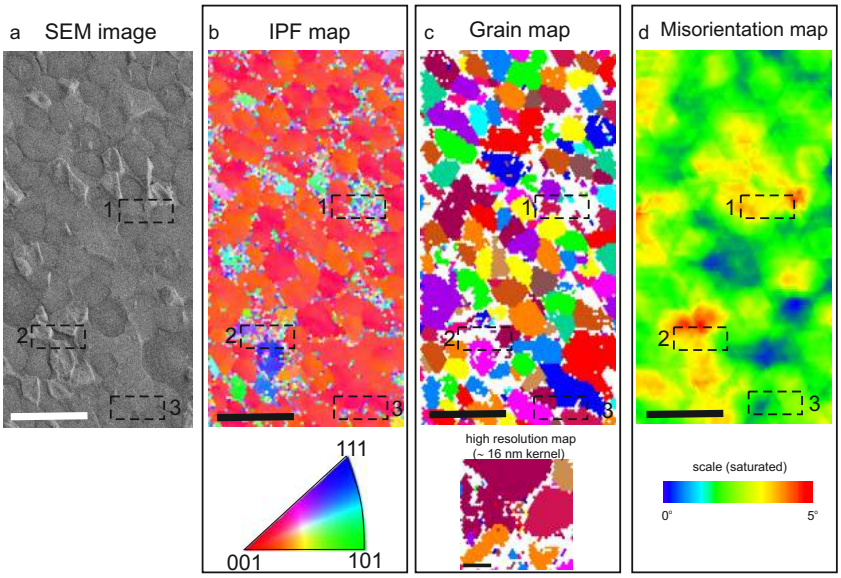

Figure 3.14: Factor contributing to disordered regions in the EBSD. (**a**) SEM image, (**b**) inverse polar figure (IPF) map showing the true crystallographic orientations, (**c**) grain map (the colors distinguish grains, not their crystallographic orientation); the high resolution map shows that the disordered region (white pixels) are clearly visible even at 100 nm step size, (**d**) local average misorientation map that is saturated up to 5 ° angle projecting the contrast clarity. Note that all of these mappings were acquired at smaller step sizes than the ones presented in **Figure 3.3**, and **Figure 3.4**. The scale bars are 20 microns. The marked regions of interest show possible causes of the disordered regions: (1) shadowing/groove/roughness, (2) transition to a higher index crystal orientation (larger lattice misorientation) and (3) intrinsic properties of the grain boundaries (at which nano-XRD confirms this is an amorphous boundaries).

3.7.7 Cross-sectional grain information

To identify if there is small grains underneath the thin-film surface, we first checked the cross-section SEM images for the whole samples with different grain sizes, and found there are no apparent small grains (**Figure 3.15a-d**). Conducting a cross-sectional EBSD map on a sub-micron thin-film is relatively challenging. Alternatively, we used a small-angle polishing technique to project the cross-section crystal misorientation mapping. The $CH_3NH_3PbBr_3$ thin-film sample was polished at 0.6° to 1° angle creating a wedge, in such the first starting line of the polished area represents the film thickness, and the last polished line represents the glass-substrate (fully polished); see the schematic **Figure 3.15e**. Using the polished sample allows us to do a top-view EBSD mapping with a geometrical correction mainly for the stretched working distance between the electron beam and sample of a half-micron (film thickness). Since the escape probability of emitted back-scattered electron in our geometry is larger than the film thickness, our detector should have detected any misorientation underneath the surface. **Figure 3.15f-h** suggest that all grains underneath the surface do not pose crystal misorientation with the top-surface. Some disordered regions appear because

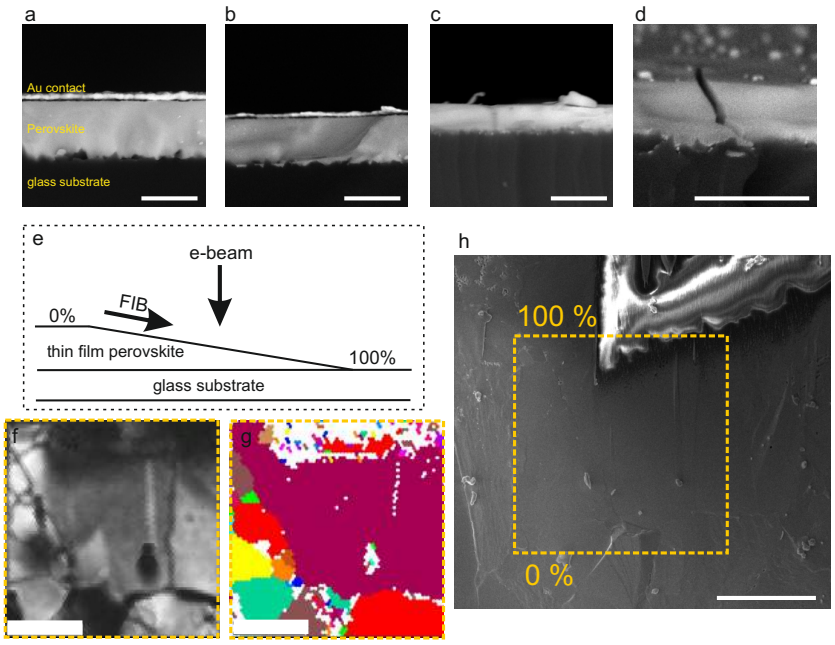

Figure 3.15: Cross-section and EBSD maps on small-angle polished thin-films. SEM cross-section showing no apparent small domains underneath the surface on samples with different grain sizes (**a-d**); the apparent rough substrates is due to an aggressive oxygen plasma treatment before the perovskite deposition; the scale bars are 500 nm. (**e**) cross-section schematic of the small-angle polishing technique with focus ion beam (FIB) creating a thin-film wedge to "look though" cross-sectional projection of EBSD mapping on sub-micron thin-film sample. The 0% indicate non-polished (starting point) and fully polished (end point) of the FIB milling. (**f**) Image quality after polishing. (**g**) grain map EBSD on the polished area. (**h**) SEM image showing the region of polished area. The end of the polished region hits the glass substrate (100 %). The scale bars are 20 μm.

of shadowing effect from the samll chunks and the debris of the glass substrate after ion-milling. From this analysis, we believe that the grain boundaries are vertically oriented, proving that the urface EBSD mappings are representative of the whole film. This is also supported by the XRD that shows very strong preferential (100) orientation of the films (**Figure 3.8**).

3.7.8 Nano X-ray diffraction analysis

The experiments were performed using the Hard X-ray Nanoprobe (HXN) of the Center for Nanoscale Materials (CNM) at sector 26-ID-C of the Advanced Photon Source, Argonne National Laboratory. The coherent and monochromatic incident X-ray beam (photon energy 9.0 keV, λ=1.378 Å) was focused on the sample by a Fresnel zone plate (Xradia Inc., 133 μm diameter gold pattern, 24 nm outer zone, 300 nm thickness), yielding $a \simeq 30$ nm full-width half-maximum lateral beam cross-section in the focal plane [41]. Imaging of the sample was performed by stepwise lateral scanning of the

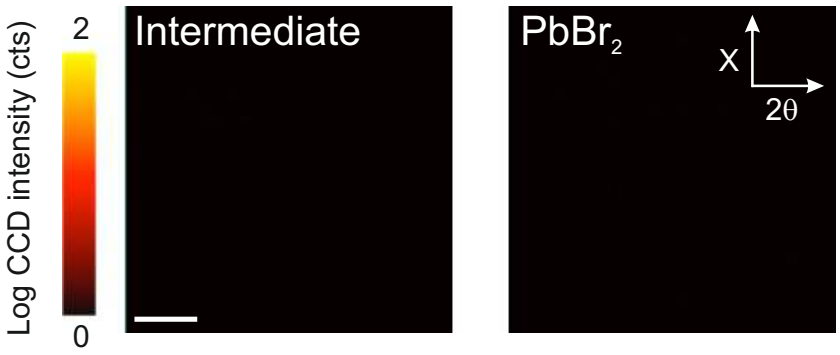

Figure 3.16: Detecting other phases. No scattering from out-of-plane intermediate or $PbBr_2$ phases was detected at the grain boundary region shown in Figure 1h. Left panel: CCD image of strongest intermediate phase scattering (θ = 15.33°, 2θ = 30.67°). Right panel: CCD iamge of strongest $PbBr_2$ scattering (θ = 16.94 °, 2θ = 33.84°).

sample and recording the diffraction image at each step. CCD images were recorded using a 0.5 s detector exposure. Simultaneous detection of element-specific X-ray fluorescence was carried out by a single-element X-ray fluorescence detector, which allowed for positioning with respect to fiducial markers created on sample surface by FIB. The $MAPbBr_3$ thin film was rotated to the [002] Bragg diffraction condition with sample θ = 13.47°, detector 2θ = 26.94°, and scanned across the region of interest. To bring tilted regions into Bragg diffraction condition, the same ROI was scanned with sample θ = 12.86° and 14.07°. The scattering intensity of the three scans were registered by the Pb fluorescence map and summed together to show all the [001]-oriented areas in (**Figure 3.16**). A very faint background scattered intensity that is apparent at the grain boundary region is attributed to scattering arising due to the extended X-ray beam tails that irradiate the nearby grains where the bulk grain is strongly diffracting. The same ROI was examined when at the Bragg diffraction condition of [002] $PbBr_2$ (sample θ = 16.94°, detector 2θ = 33.84°) and an intermediate phase peak (sample θ = 15.33°, detector 2θ = 30.67°). No scattered intensity is detected from out-of-plane $PbBr_2$ and intermediate phase at the grain boundary region of interest (**Figure 3.16**). The focused beam size of the nano-XRD used here is around 50 nm. However, the horizontal (x) resolution is compromised because of the Bragg angle (~13°) between X-ray and sample. So the horizontal (x) resolution is around 200 nm while the vertical (y) resolution is still 50 nm.

References

[1] W-J. Yin, T. Shi, and Y. Yan, *Unusual defect physics in $CH_3NH_3PbI_3$ perovskite solar cell absorber*, Appl.Phys.Lett. **104**, 4 (2014).

[2] A. Walsh, D. O. Scanlon, S. Chen, X. G. Gong, and S-H. Wei, *self-regulation mechanism for charged point defects in hybrid halide perovskites*, Angew. Chem. Int. Ed. **54**, 1791 (2015).

[3] S. Heo, G. Seo, Y. Lee, D. Lee, M. Seol, J. Lee, J-B. Park, K. H. Kim, D-J. Yun, Y. Kim, J. Shin, T. K. Ahn, and M. K. Nazeeruddin, *Deep level trapped defect analysis in $CH_3NH_3PbI_3$ perovskite solar cells by deep level transient spectroscopy*, Energy Environ. Sci. **10**, 1128 (2017).

[4] G. Xing, N. Mathews, S. S. Lim, N. Yantara, X. Liu, D. Sabba, M. Grätzel, S. Mhaisalkar, and T. C. Sum, *Low-temperature solution- processed wavelength-tunable perovskites for lasing*, Nature Mat. **13**, 476 (2014).

[5] S. D. Stranks, *Nonradiative losses in metal halide perovskites*, ACS Energy Lett. **2**, 1515 (2017).

[6] D. Shi, V. Adinolfi, R. Comin, M. Yuan, E. Alarousu, A. Buin, Y. Chen, S. Hoogland, A. Rothenberger, K. Katsiev, Y. Losovyj, X. Zhang, P. A. Dowben, O. F. Mohammed, E. H. Sargent, O. M. Bakr, *Low trap-state density and long carrier diffusion in organolead trihalide perovskite single crystals*, Science **347**, 519 (2015).

[7] J. S. Yun, A. Ho-Baillie, S. Huang, S. H. Woo, Y. Heo, J. Seidel, F. Huang, Y-B. Cheng, and M. A. Green, *benefit of grain boundaries in organic?inorganic halide planar perovskite solar cells*, J.Phys.Chem.Lett. **6**, 875 (2015).

[8] D. W. deQuilettes, S. M. Vorpahl, S. D. Stranks, H. Nagaoka, G. E. Eperon, M. E. Ziffer, H. J. Snaith, D. S. Ginger, *Impact of microstructure on local carrier lifetime in perovskite solar cells*, Science **348**, 683 (2015).

[9] D-Y. Son, J. W. Lee, Y. J. Choi, I-H. Jang, S. Lee, P. J. Yoo, H. Shin, N. Ahn, M. Choi, D. Kim, and N-G. Park, *Self- formed grain boundary healing layer for highly efficient $CH_3NH_3PbI_3$ perovskite solar cells*, Nature Energy **1**, 8 (2016).

[10] P. Khoram, S. Brittman, W. I. Dzik, J. N. H. Reek, and E. C. Garnett, *growth and characterization of PDMS-stamped halide perovskite single microcrystals*, J.Phys.Chem.C **7**, 6475 (2016).

[11] N. Giesbrecht, J. Schlipf, L. Oesinghaus, A. Binek, T. Bein, P. Mü?ller- Buschbaum, and P. Docampo, *synthesis of perfectly oriented and micrometer-sized $MAPbBr_3$ perovskite cyrstals for thin-film photovoltaic applications*, ACS Energy Lett. **1**, 150 (2016).

[12] N. J. Jeon, J. H. Noh, Y. C. Kim, W. S. Yang, S. Ryu, and S. I. Seok, *Solvent engineering for high-performance inorganic-organic hybrid perovskite solar cells*, Nat.Mater. **13**, 897 (2014).

[13] J. S. Manser, M. I. Saidaminov, J. A. Christians, O. M. Bakr, and P. V. Kamat, *Making and breaking of lead halide perovskites*, Acc.Chem.Res. **49**, 330 (2016).

[14] Y. Guo, K. Shoyama, W. Sato, Y. Matsuo, K. Inoue, K. Harano, C. Liu, H. Tanaka, and E. Nakamura, *Chemical pathways connecting lead(II) Iodide and perovskite via polymeric plumbate(II) fiber*, J. Am. Chem. Soc. **137**, 15907 (2015).

[15] Y. Rong, S. Venkatesan, R. Guo, Y. Wang, J. Bao, W. Li, Z. Fanc, and Y. Yao, *Critical kinetic control of non-stoichiometric intermediate phase transformation for efficient perovskite solar cells*, Nanoscale **8**, 12892 (2016).

[16] J. Visser, B. v. d. Heijden, S. J. A. Weijers, R. d. Vries, and J. L. Visschers, *A gigabit per second read-out system for Medipix quads*, Nuclear Instruments and Methods in Physics Research A **633**, S22 (2011).

[17] X. Liopart, R. Ballabriga, M. Campbell, L. Tlustos, W. Wong, *Timepix, a 65k programmable pixel readout chip for arrival time, energy and/or photon counting measurements*, Nuclear Instruments and Methods in Physics Research A **581**, 485 (2007).

[18] E. Levine, W. L. Bell, and G. Thomas, *Further applications of Kikuchi diffraction patterns; Kikuchi Maps*, Journal of Applied Physics **37**, 2141 (2007).

[19] J. J. Choi, X. Yang, Z. M. Norman, S. J. L. Billinge, and J. S. Owen, *Structure of methylammonium lead iodide within mesoporous titanium dioxide: active material in high-performance perovskite solar cells*, Nanolett. **14**, 127 (2014).

[20] B. L. Adams, S. Ta'asan, D. Kinderlehrer, I. Livshits, D. E. Mason, C-T, Wu, W. W. Mullins, G. S. Rohrer, A. D. Rollett, and D. M. Saylor, *Extracting grain boundary and surface energy from measurement of triple junction geomtery*, Interface Science **7**, 321 (1999).

[21] W. T. Read and W. Shockley, *Dislocation models of crystal grain boundaries*, Phys. Rev. **78**, 275 (1950).

[22] Y. Huang and F. J. Humphreys, *Measurement of grain boundary mobility during recrystallization of a single-phase aluminium alloy*, Acta Materialia **47**, 2259 (1999).

[23] M. Taheri, H. Weiland, and A. Rollett, *Method of measuring stored energy macroscopically using statistically stored dislocations in commercial purity aluminum*, Metall. and Mat. Trans. A **37**, 19 (2006).

[24] D. Abou-Ras and K. Pantleon, *The impact of twinning on the local texture of chalcopyrite-type thin films*, Phys.Stat.Sol (RRL) **1**, 187 (2007).

[25] J. D. Poplawsky, N R. Paudel, C. Li, C. M. Parish, D. Leonard, Y. Yan, and S. J. Pennycook, *Direct imaging of Cl- and Cu-induced short-circuit efficiency changes in CdTe solar cells*, Adv. Energy Mater. **4**, 1 (2014).

[26] G. Stokkan, *Twinning in multicrystalline silicon for solar cells*, Journal of Crystal Growth **384**, 107 (2013).

[27] R. L. Woo, R. Xiao, Y. Kobayashi, L. Gao, N. Goel, M. K. Hudait, T. E. Mallouk, and R. F. Hicks, *Effect of twinning on the photoluminescence and photoelectrochemical properties of indium phosphide nanowires grown on silicon*, Nanolett. **8**, 4664 (2008).

[28] E. Brown, C. Sheng, K. Shimamura, F. Shimojo, and A. Nakano, *Enhanced charge recombination due to surfaces and twin defects in GaAs nanostructures*, J. App. Phys. **117**, 054307 (2015).

[29] F. Bertolotti, L. Protesescu, M. V. Kovalenko, S. Yakunin, A. Cervellino, S. J. L. Billinge,

M. W. Terban, J. S. Pedersen, N. Masciocchi, and A. Guagliardi, *Coherent nanotwins and dynamic disorder in cesium lead halide perovskite nanocrystals*, ACS Nano **11**, 3819 (2017).

[30] M. U. Rothmann, W. Li, Y. Zhu, U. Bach, L. Spiccia, J. Etheridge, and Y-B. Cheng, *Direct observation of intrinsic twin domains in tetragonal $CH_3NH_3PbI_3$*, Nature Comm. **8**, 14547 (2017).

[31] H. N. Demers, N. Poirier-Demers, A. R. Couture, D. Joly, M. Guilmain, N. de Jonge, and D. Drouin, *Three-dimensional electron microscopy simulation with the CASINO Monte Carlo software*, Scanning. **33**, 92 (2011).

[32] ASTM E112-13, *Standard test methods for determining average grain size*, ASTM International, West Conshohocken, 2013.

[33] P. Lehto, H. Remes, T. Saukkonen, H. Hänninen, and J. Romanoff, *Influence of grain size distribution on the Hall?Petch relationship of welded structural steel*, Mater. Sci. Eng. A **592**, 28 (2014).

[34] K. Barmak, J. Kim, C. S. Kim, W. E. Archibald, G. S. Rohrer, A. D. Rollet, D. Kinderlehrer, S. Ta'asan, H. Zhang, and D. J. Srolovitz, *Grain boundary energy and grain growth in Al films: Comparison of experiments and simulation*, Scripta Materialia **54**, 1059 (2006).

[35] Y. Rakita, S. R. Cohen, N. K. Kadem, G. Hodes, and D. Cahen, *Mechanical properties of $APbX_3$ (A=Cs or CH_3NH_3; X = I or Br) perovskite single crystals*, MRS Communications **5**, 623 (2015).

[36] J. Feng, *Mechanical properties of hybrid organic-inorganic $CH_3NH_3BX_3$ (B = Sn, Pb; X = Br, I) perovskites for solar cell absorbers*, App.Phys.Lett. **2**, 081801 (2014).

[37] A. Godfrey, W. Q. Cao, N. Hansen, and Q. Liu, *Stored energy, microstructure, and flow stress of deformed metals*, Metallurgical and Materials Transactions A **36**, 2371 (2005).

[38] A. Aguiar, S. Wozny, T. G. Holesinger, T. Aoki, M. K. Patel, M. Yang, J. J. Berry, M. Al-Jassim, W. Zhou, and K. Zhu, *In situ investigation on the formation and metastability of formamidinium lead tri-iodide perovskite solar cells*, Energy Environmental Science **9**, 2372 (2016).

[39] L. D. Whalley, J. M. Frost, Y-K. Jung, and A. Walsh, *Perspective: theory and simulation of hybrid halide perovskites*, The Journal of Chemical Physics **146**, 220901 (2017).

[40] Y. Liu, K. Palotas, X. Yuan, T. Hou, H. Lin, Y. Li, and S-T. Lee, *Atomistic origins of surface defects in $CH_3NH_3PbBr_3$ perovskite and their electronic structures*, ACS Nano **11**, 2060 (2017).

[41] M. Holt, R. Harder, R. Winarski, and V. Rose, *Nanoscale hard X-ray microscopy methods for materials studies*, Annu.Rev.Mater.Res. **43**, 183 (2013).

[42] B. W. Silverman, *Kernel density estimation using the fast Fourier transform*, Journal of the Royal Statistical Society. Series C (Applied Statistics) **31**, 93 (1982).

[43] B. G. Yacobi and D. B. Holt, *Cathodoluminescence Microscopy of Inorganic Solids*, Plenum Press, New York, 1990.

[44] K. Kanaya and S. Okayama, *Penetration and energy-loss theory of electrons in solid targets*, J.Phys.D: Appl. Phys. **5**, 17 (1972).

4

Detrimental and Beneficial Roles of Grain Boundaries in Halide Perovskites

This Chapter attempts to correlate the true grain size with photoluminescence lifetime, carrier diffusion length, and mobility in halide perovskites. We find that the grain boundaries are not benign as is often claimed, but have a recombination velocity of 1670 cm/s, comparable to that of crystalline silicon. However, as with silicon, amorphous perovskite can passivate crystalline boundaries, leading to brighter photoluminescence and longer carrier lifetime without reducing diffusion length. This variable grain boundary character explains the mysteriously long lifetime and record efficiency achieved in small grain halide perovskite thin films, while pointing the way forward to even better performance.

4.1 Introduction

The influence of grain boundaries on material properties in halide perovskites has been debated and remains an outstanding question in the field. Several studies [1–3, 5, 6, 36] on $CH_3NH_3PbI_3$ perovskite films with grain domains less than 5 μm show that carrier lifetime, mobility, and diffusion length increase with domain size, as does the power conversion efficiency of solar cells. These correlations suggest that grain boundaries contribute to non-radiative recombination and reduce device performance. Improvements in performance have also been reported for films with (claimed) grain size even up to the millimeter-scale [7]. In contrast, Kelvin probe

force microscopy studies of $CH_3NH_3PbI_3$ films have claimed that grain boundaries are beneficial for charge separation and collection [8], and theory has suggested that PbI_2 at grain boundaries can be beneficial [9], supporting an earlier hypothesis [10, 11]. Furthermore, experiments examining the effects of grains on photovoltaic performance have indicated that heterogeneity of local voltage [12] and crystal facets [13] near grain boundaries are important factors. Finally, while many factors have been shown to contribute to the exceptionally long photoluminescence lifetime in halide perovskites, none of them explain why high performance films with the largest grain size to date (approaching 1 mm) have a lifetime nearly 2 orders of magnitude shorter than those with a 2 micron grain size [7, 14].

We address the issue by correlating the accurate values of grain sizes of $CH_3NH_3PbBr_3$ (**Chapter 3**) with photoluminescence intensity and lifetime, minority carrier diffusion length, and mobility. Larger grain size (even up to 60 microns) is generally beneficial for all properties. Although most samples show crystalline grain boundaries, samples with amorphous regions at the grain boundaries show properties better than expected according to the grain size. The longer PL lifetime and higher PL intensity at these amorphous regions suggests that amorphous interfaces can improve optoelectronic properties, perhaps either by improving grain boundary passivation, locally doping the material or gettering native defects. Putting the grain size dependence of optoelectronic properties into a recombination model shows that grain boundary recombination plays an important role in the maximum achievable solar cell and LED efficiency up to grain sizes approaching a millimeter.

4.2 Grain boundary effects on photoluminescence

To understand how the grain boundaries in $CH_3NH_3PbBr_3$ perovskite films affect photo-generated charge carriers, we recorded photoluminescence (PL) decay profiles on samples each having a different grain size. The PL peak was at 534 nm, which is typical for $CH_3NH_3PbBr_3$ perovskite, and the integrated intensity between 475-600 nm was used for the lifetime curves. **Figure 4.1** shows that when the PL signal, measured locally, is averaged over the entire map, samples with larger grains yield higher PL intensity and longer lifetimes. In the sample with the largest grains, the grain boundaries appear dark (particularly in the lifetime map), which is consistent with their role as a source of non-radiative recombination and would explain the general trend of longer lifetimes in films with larger grains (further discussion regarding the evolution of recombination coefficients, and effects of diffusion are in the Supporting information). Unexpectedly, however, the sample with medium-sized grains (**Figure 4.1b**) shows PL intensity 30 times brighter and lifetimes 3 times longer at the boundaries as compared to the center of the grain. EBSD maps together with nano-XRD analysis indicate that these grain boundaries consist of an amorphous phase (earlier found in **Chapter 3**). Interestingly, the qualitatively different nature of such an amorphous phase at grain boundaries could explain the mysteriously long lifetimes, large local variations and excellent efficiency seen in some small grain halide perovskite thin films devices [14].

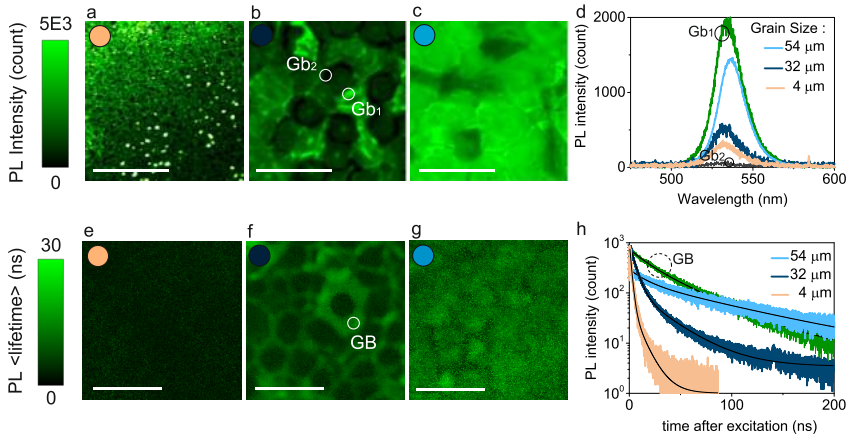

Figure 4.1: Photoluminescence (PL) intensity and lifetime of $CH_3NH_3PbBr_3$ perovskite films with different grain sizes. PL intensity maps with 4 ± 1.7μm (**a**), 32 ± 7 μm (**b**), and 54 ± 17 μm (**c**) grain sizes showing local heterogeneity is more pronounced near the grain boundary for the <32 μm>-grain sample. (**d**) PL spectra showing a similar emission wavelength regardless of the grain sizes; the difference of PL intensity at around the grain boundary for the <32 μm> grain are highlighted (spot Gb1 and spot Gb2). PL effective lifetime maps (integrating time-trace decay that is a convolution of trap-assisted, radiative, and Auger recombination processes) with 4 ± 1.7 μm (**e**), 32 ± 7 μm (**f**), and 54 ± 17 μm (**g**) grain sizes. (**h**) Time-resolved PL decay traces showing a faster PL decay for samples with smaller grain sizes. For the sample with medium-sized grains , the PL lifetime near the grain boundary always exhibits a slower decay (spot GB) compared to its grain interior. The recombination coefficients are extracted by fitting the PL decay traces (black lines). All scale bars (**a-c**, and **e-g**) are 50 μm.

Our PL measurements show that the amorphous phase has higher PL intensity and lifetime than the bulk perovskite; however, the longer lifetime does not necessarily indicate improved photovoltaic performance, which depends on the charge carrier diffusion length that is a function of both carrier lifetime and mobility [16].

4.3 Grain boundary effects on diffusion length

To understand the role of grain boundaries in halide perovskites on electronic transport, we used the steady-state photocarrier grating (SSPG) technique to measure the ambipolar charge-carrier diffusion length within the films [3, 17]. This technique relies on measuring lateral carrier transport in the film in the presence of sinusoidal laser interference (an optical grating) created by two monochromatic lasers (450 nm excitation wavelength) where one laser is weaker than the other. Any carrier diffusion length longer than the interference periodicity will smear out the grating amplitude, and therefore the sample conductivity can be measured. By monitoring how the sample conductivity changes as a function of the period of the grating, the minority carrier diffusion length can be extracted (details in Supporting information) [18, 19]. Using a similar laser excitation wavelength for the SSPG and PL measurements (480 nm), we

expect the distribution of the photo-generated carriers to be similar. We carried out the measurement on the same samples used earlier for the PL studies and observed that the carrier diffusion length increases with grain size (**Figure 4.6**). The diffusion lengths extracted range from 168 nm to 548 nm with increasing grain size from <4 μm> to <54 μm>. It clearly shows that the increased grain size still improves the carrier transport, even if the grain size is two orders of magnitude larger than the diffusion length.

4.4 Statistical correlation of grain sizes and optoelectronic properties

Generally we observed that $CH_3NH_3PbBr_3$ perovskite films with larger grains yield longer PL lifetimes; however, PL lifetimes for the <32 μm> grained film were longer than expected (**Figure 4.1**). For each sample, we collected approximately 20 maps of PL lifetime, each from a different spot, and tabulated the trap-assisted (monomolecular) lifetime as a function of grain size in **Figure 4.2a**. Each data point represents an ~80 x 80 μm^2 PL lifetime map. We find that the mean PL lifetime (see the distribution on the right y-axis, **Figure 4.2a**) of the <32 μm> grain sample is longer than that of the <54 μm> grain sample, which suggests that the grain boundaries in the <32 μm> sample have a different electronic character than those in the other samples. This special electronic character is consistent with the amorphous nature of the grain boundary. **Figure 4.2b** shows that the diffusion length increases with grain size. The absence of the anomaly at <32 μm> grain sample suggests that the increase in PL lifetime is coupled to a decrease in carrier mobility.

To quantify this relationship, we used Fourier decomposition to solve the steady-state diffusion equation and fit this analytical solution to the data (details in the supporting information). We modelled and fit the data numerically; however to obtain an intuitive picture, we can approximate the dependence of carrier diffusion length on grain size by examining the first term in a truncated Fourier expansion [20–28]:

$$L_d = \left(\frac{2S_{GB}}{DG} + \frac{1}{(LA)^2} \right)^{-1/2} \tag{4.1}$$

where L_d is the minority carrier diffusion length (value that is obtained from the SSPG measurement), S_{GB} is grain boundary recombination velocity, D is the asymptotic value of the diffusion coefficient of the polycrystalline thin film, G is the grain size, L is the asymptotic value of the diffusion length of the polycrystalline thin film, and A is defined as:

$$A = \frac{1 + \frac{S_{FB}L}{D} \tanh\left(\frac{W}{L}\right)}{\frac{S_{FB}L}{D} + \tanh\left(\frac{W}{L}\right)} \tag{4.2}$$

where S_{FB} is front or back surface recombination velocity (assumed to be the same), and W is film thickness. G, L, D, L_d and W are known from the experiments, whereas S_{GB} and S_{FB} were used as free fitting parameters. The values of L and D depend on the

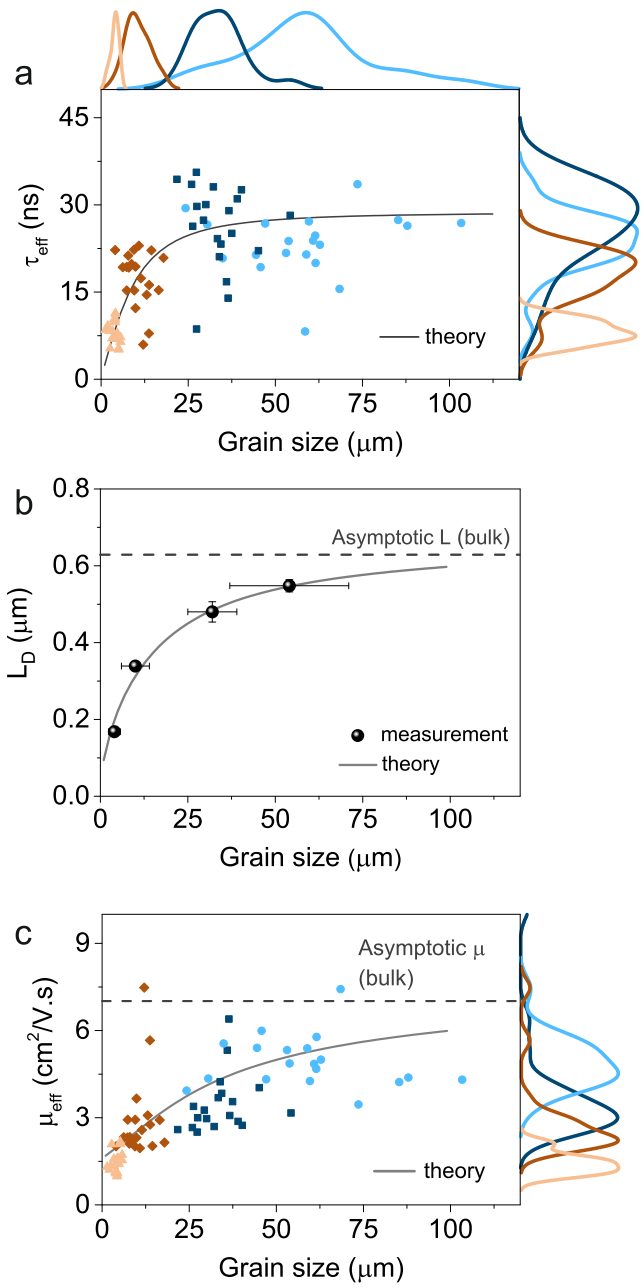

Figure 4.2: Statistical correlation of grain sizes and optoelectronic properties of $CH_3NH_3PbBr_3$ perovskite. (**a**) The effective carrier lifetimes (τ_{eff}) versus grain sizes. The τ_{eff} is extracted from the PL decay traces where each point represents an area mapping of 80 μm × 80 μm size within the same substrate; right y-axis: the Gaussian kernel function [52] (with a bandwidth of h = 0.337) to illustrate the distributions of the extracted τ_{eff}; top x-axis. (**b**) minority carrier diffusion length (L_D) versus grain size; the L_D values are extracted from steady-state photo-carrier grating measurements (SSPG) across scanning areas of ~0.5 cm × 0.5 cm; the y-error bars represent linear propagation of error from the measurement, while x-error bars represent a 95% confidence interval. (**c**) carrier mobility (μ_{eff}) versus grain size; the data is calculated from each data point of τ_{eff} (Figure **a**) and the L_D values (Figure **b**). All measurements were conducted on identical samples with nearly the same spot area.

quality of the bulk perovskite material and are the asymptotic values of the experimental data for L_d and D calculated using the Einstein relation and the asymptotic effective mobility (μ_{eff}) at which the effect of grain boundaries is no longer relevant (**Figure 4.2b-c**). After global optimization, we find the solutions for S_{GB}, S_{FB}, L, and D in our sample are 1670 ± 50 cm/s, 27 ± 1.5 cm/s, 0.61 μm, and 0.18 cm^2/s, respectively. Note that with a surface recombination velocity (S_{FB}) 30 times lower than the grain boundary recombination velocity (S_{GB}), grain boundaries still play a significant role in transport up to a grain size of ~20 μm (35% contribution to L_d). For larger grains, the surface recombination then becomes more influential. Grain boundary recombination accounts for 80% of the reduced L_d when the ratio W/L is 1 (perovskite thickness of 610 nm); much smaller values for W/L (much thinner cells) are needed before surface recombination dominates. The grain boundary recombination velocity in our polycrystalline $CH_3NH_3PbBr_3$ film is comparable to the surface recombination velocity of single crystalline $CH_3NH_3PbBr_3$ reported by Yang et al [42]. The recombination velocity at the grain boundary for halide perovskites has never been reported before, but the values obtained here fall around an order of magnitude higher than that of unpassivated CdTe [30] and similar to mc-Si [31, 32] or CIGS [33, 34].

We can calculate an effective mobility indirectly from the diffusion length measurement (**Figure 4.2b**) and the PL lifetime data (**Figure 4.2a**). We find that, except for the <32 μm> grain sample, the effective mobility increases with grain size (**Figure 4.2c**); a similar trend was previously reported for $CH_3NH_3PbI_3$ films [1]. In the <32 μm> grain-sample, the amorphous grain boundaries appear to limit mobility because this sample diffusion length is unchanged, while its lifetimes are anomalously long. The mobility in our $CH_3NH_3PbBr_3$ samples ranges between ~1.5 to 7.5 cm^2/V.s, similar to the values estimated from PL quenching measurements [35]. The effective mobility presented here is the intrinsic ambipolar transport mobility which will be dominated by the excess carrier with smaller diffusion length, thus isolating any effect from transporting layers.

4.5 Implications for perovskite thin-films, solar cells, and future research

Although some studies have reported that grain boundaries reduce mobility [1], diffusion length [3], and solar cell performance [2] in halide perovskites, they were limited to grain sizes comparable to the film thickness (less than 1 μm) and did not use a crystallographic technique to measure grain size. Furthermore, grain boundary effects in halide perovskite films have been considered negligible when the grain size is much larger than the film thickness [7] and all grain boundaries have been treated as having the same effect on performance. In this report, we have shown in a $CH_3NH_3PbBr_3$ system made from a lead-acetate precursor that grain boundaries still play a dominant role in the optoelectronic properties up to the range of <20 μm> and that crystalline grain boundaries behave qualitatively different than those containing amorphous perovskite. The relatively high surface recombination velocity of $CH_3NH_3PbI_3$ (450 cm/s) [36]

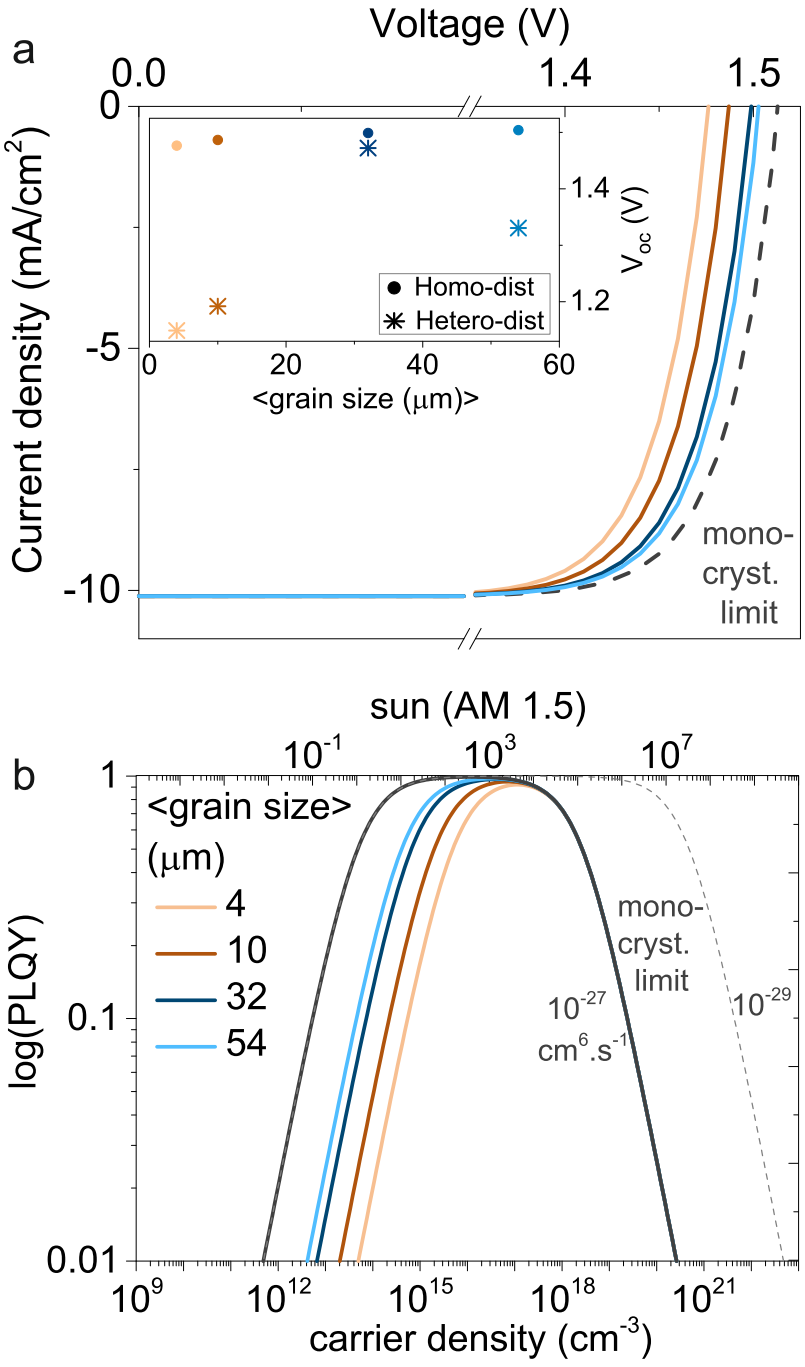

Figure 4.3: Modelling the characteristics of solar cells and photoluminescence quantum yield with different grain sizes of $CH_3NH_3PbBr_3$ perovskite. (a) simulated *J-V* curve showing that larger grain size increases V_{oc}. This correlation becomes randomized when the heterogeneity of grain size (the experimental standard deviation) is introduced into the model (the inset). Colors have the same labels in both panels. (**b**) Simulated *PLQY* as a function of the carrier density for different grain sizes using experimentally determined parameters; the *PLQY* at higher fluence is mainly limited by Auger recombination with two limiting values chosen from the literatures [41, 42].

compared to our films (27 cm/s) suggests that grain boundaries will provide a major source of losses in record devices after future improvements in $CH_3NH_3PbI_3$ surface passivation.

To examine such effects, we model a solar cell and compute the maximum attainable photoluminescence quantum yield (PLQY) based on our film characteristics (S_{GB} = 1670 cm/s, S_{FB} = 27 cm/s, L = 0.61 μm, and D = 0.18 cm^2/s, details in Supporting information). The solar cell consists of a planar polycrystalline $CH_3NH_3PbBr_3$ absorber layer sandwiched between two transporting layers (TiO_2, and NiO_x) and metal contacts (FTO, and Au). **Figure 4.3a** shows simulated *J-V* curves of solar cells with different grain sizes (homogeneous grain size for each). The grain size primarily regulates the open circuit voltage (V_{oc}), with minimal impact on the short-circuit current density (J_{sc}). If we assume a grain size distribution (as observed experimentally), then there is significant heterogeneity of the simulated local voltage of each individual grain. Since the full device can be modelled as a collection of individual grains connected electrically in parallel, the V_{oc} is limited by the smallest grains in this distribution [37]. For example when the width of the distribution is ~30% of the average grain size, the V_{oc} drops from ~1.5 V to ~1.33 V, precluding simple experimental device studies of the effect of grain size, since samples with larger grain sizes also have wider distributions (inset in **Figure 4.3a**). Both the average and the distribution must be taken into account. This heterogeneity effect, however, is almost negligible if the device is stacked laterally resembling an interdigitated back contact solar cell [38]. In this regard, moving toward monocrystalline thin films for solar cells is still necessary for better device performance: completely removing grain boundaries from a 4 micron grain size halide perovskite film would increase V_{oc} by 110 mV (8 %) in a solar cell with ideal contacts (67 mV increase in V_{oc} with simulated contact losses, **Figure 4.3a**). Clearly, minimizing grain boundaries is still required to improve the device performance.

Next, we simulated the photoluminescence quantum yield (PLQY) of our films by assuming that all losses at the grain boundary, on the front/back surface, and in the bulk contribute to monomolecular trap-assisted recombination. The analytical expression of equation 4.1 and 4.2 can be used to convert the minority carrier diffusion length into an effective lifetime that is inversely proportional to monomolecular recombination coefficient as a function of grain size (details in the Supporting information). The carrier density required to reach a PLQY of 1% is reduced by one order of magnitude when we increase the grain size from 4 μm to 54 μm, and by two orders of magnitude when all grain boundaries are removed (monocrystalline film, **Figure 4.3b**). Having relatively large grain sizes up to 54 μm is still not enough to reach the monocrystalline total integrated PLQY. We estimate that a half-millimeter grain size is required to get 96 % of the monocrystalline performance, which is particularly important for 1 sun applications.

4.6 Conclusions

In conclusion, here we show the importance of using true grain size information when studying the effect of grain boundaries in halide perovskite thin films. We find grain boundaries in $CH_3NH_3PbBr_3$ are not benign, but have a recombination velocity of 1670 cm/s ± 50 cm/s, comparable to that of crystalline silicon, where it plays a key role in lowering performance. Our modeling suggests that increasing the average grain size (and uniformity) to close to a millimeter or drastically lowering grain boundary recombination velocity is necessary to approach the limiting efficiency potential. Interestingly, under certain conditions amorphous regions can exhibit enhanced photoluminescence intensity and lifetime without degrading carrier diffusion length. These results can explain the conflicting literature reports of grain boundary effects in halide perovskites: crystalline grain boundaries are very detrimental to performance while amorphous regions can provide excellent passivation and longer lifetimes. Just as in advanced silicon technology, moving towards monocrystalline layers and engineering amorphous/crystalline interfaces are necessary to approach the limiting theoretical efficiency for solar cells and LEDs.

4.7 Supporting information

4.7.1 Photoluminescence characterization

PL intensity measurement

PL intensity was measured using a confocal imaging microscope (WITec alpha300 SR). A 405 nm laser diode (Thorlabs S1FC405) was used as an excitation source where the PL intensity of the $CH_3NH_3PbBr_3$ perovskite film was collected in reflection mode through a NA 0.9 objective using a spectrometer (UHTC 300 VIS, WITec). The intensity was counted within the 475 to 600 nm emission wavelength range.

Time-resolved PL lifetime measurement

PL decays were measured using a time-correlated single-photon counting (TCSPC) method. The setup was equipped with a picosecond pulse driver (PicoQuant PDL 828), an excitation source at 485 nm, <110 ps pulse width, and 5 to 40 MHz repetition rate (PicoQuant LDH-D-C-485), a picosecond time analyzer (PicoQuant HydraHarp 400), and a single photon counting detector (MicroPhoton Devices, MPD-5CTD). A series of neutral density filters was used to attenuate the intensity of the laser source where the measurement was acquired at 0.5×10^{18} cm^{-3} to 2.9×10^{18} cm^{-3} initial carrier density (these values assume that all of the photo-generated carriers are distributed uniformly throughout the thickness of the film). The excitation was focused down to a diffraction-limited spot through a water droplet and coverslip onto the perovskite film using an objective (Nikon, CFI Plan Apochromat VC 60XC WI, NA 1.2). A dichroic mirror (ET500LP, Chroma Tech), and long-pass filter (ET500LP, Chroma Tech) were

used to transmit the emission from the $CH_3NH_3PbBr_3$ perovskite film to the detector, while excluding any contribution from the excitation source. A tube lens (Thorlabs, AC254-030-A-ML, focal length 30 mm and diameter 22 mm) was placed one focal length before the detector to collect the emission. The final magnification of the optical system is therefore 60x × 30 mm/200 mm (reference focal length of Nikon infinity corrected objective), which gives 9x magnification at the 50 × 50 μm^2 detector. Given this magnification, any light within approximately 2.5 μm of the excitation spot would be detected, making this not a true confocal system, which has implications for the effect of diffusion on the measured decays (see below). We kept the count rate of the measurement below 1% of the repetition rate of the laser in order to prevent artifacts from photon pile up. The samples were soaked under the same laser (CW mode) for about 1-2 minutes before the measurement to minimize light-induced dynamics (if any) within the perovskite structures. In fact, over several measurements (time span of ~3 to 6 months), we observed no PL lifetime degradation within the samples presented in this report. All measurements were performed at ambient conditions.

Data fitting

We modelled the photoluminescence decay (PL(t)) of the $CH_3NH_3PbBr_3$ perovskite film as:

$$PL(t) = \phi b n(t)^2 \tag{4.3}$$

where ϕ is the collection efficiency (extraction efficiency), b is the bimolecular recombination coefficient, and *n(t)* is the time-dependent carrier density. We then defined the time-dependent carrier density as the integral of excess carrier density over time:

$$PL(t) = \phi b \left(\int_0^t \frac{dn(\acute{t})}{d\acute{t}} \right)^2 \tag{4.4}$$

by assuming that Auger recombination is not significant within the range of excitation used here, we simplified the total carrier recombination as the parallel contributions of monomolecular trap- assisted and bimolecular radiative recombination:

$$\frac{dn(t))}{dt} = -an(t) - bn(t)^2 \tag{4.5}$$

$$PL(t) = \phi b \left[\int_0^t \left(an(\acute{t}) + bn(\acute{t})^2 \right) d\acute{t} \right]^2 \tag{4.6}$$

$$PL(t) = \phi b \left[\frac{n_0 a}{e^{at}(a + n_0 b) - n_0 b} \right]^2 \tag{4.7}$$

Where a is the monomolecular (trap-assisted) recombination coefficient, b is the bimolecular radiative recombination coefficient, n_0 is the initial carrier density (at t =

0). For the data fitting routine, we normalized the experimental decay trace by setting the PL(t=0) = 1 (not the n_0), and therefore:

$$1 = PL(t=0) = \phi b \left[\frac{n_0 a}{(a + n_0 b) - n_0 b} \right]^2 \tag{4.8}$$

We first removed the background by calculating the average of the data points before the excitation pulse, and then subtracting this value from the data trace. Therefore we obtained the maximum point of the excess carrier density over time which corresponds to the initial excess carrier density used in the experiment. This maximum point was counted after ~0.1 ns (instrumental response function). Before the fitting to determine *a* and *b*, we normalized the PL(t) to 1 and suppressed any noise from the data using Lancos differentiators method [39] with a derivative well fitted through the third-order polynomial. **Figure 4.4** tabulates all recombination coefficients obtained from the data fitting.

Data analysis

Data analysis. The PL peak shifts to slightly longer wavelengths as the grain size increases (up to ~3.1 nm; ~0.013 eV), which might indicate enhanced charge-carrier diffusion that facilites photon reabsorption within the film. The PL decay of polycrystalline films is a convolution of their intrinsic bulk, surface, and grain boundary properties as well as extrinsic variation in film thickness [40] and surface roughness [41]. Our goal was to control for as many of these variables as possible to extract the influence of grain boundaries. To this end, our films were prepared from the same stock solution, and the protocol varied only the spin duration to control the grain size. We found decreased recombination coefficients (both monomolecular and bimolecular) with decreased grain sizes where the monomolecular recombination coefficient decreases by a factor of 3 when the grain size increases from <4 μm> to <54 μm>, and this is consistent with their corresponding increased effective lifetime. All films were less than ~230 nm thick, except the film with largest grains was thicker (~580 nm). According

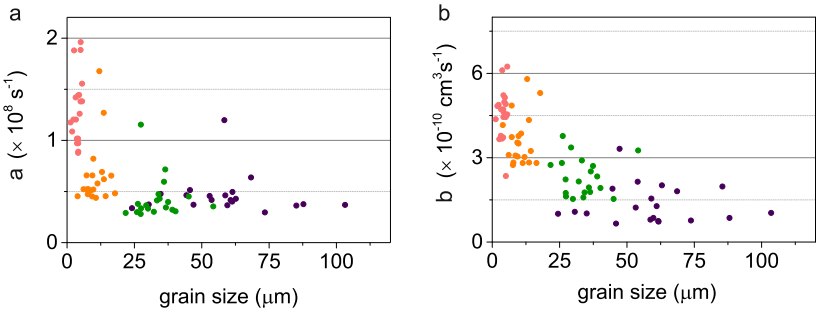

Figure 4.4: Evolution of recombination coefficients as a function of grain size in $CH_3NH_3PbBr_3$ perovskite. (**a**) monomolecular (trap-assisted) recombination coefficient, and (**b**) bimolecular recombination coefficient.

to AFM measurements, the root-mean-square surface roughness of the films with the smallest, and largest grain sizes are 22 nm and 55 nm, respectively. Within these ranges, it seems that the variation of thickness and surface roughness may affect the measured bimolecular recombination coefficient [40]. The bimolecular recombination coefficient value of our samples is within 1.31 to 4.57 × 10^{-10} cm^3s^{-1}, which is similar to the value reported by Yang et al. [42] (7 × 10^{-11} cm^3s^{-1}). The monomolecular recombination coefficient of our samples ranges from 0.43 to 1.31 × 10^8s^{-1}, which is considerably higher than the literature values from Yang et al. [42] (3.68 × 10^4s^{-1}) and Richter et al. [41] (3 × 10^6s^{-1}).

Accounting for effects of diffusion

To evaluate the possibility of excited charges diffusing away from the collection spot, we modelled the evolution of the photoluminescence dynamics in equation (4.4) as a function of transient time (t) and 2-dimensional space domain (x-, y-):

$$\frac{dn(x,y,t)}{dt} = D\left[\frac{d^2}{dx^2} + \frac{d^2}{dy^2}\right] n(x,y,t) - an(x,y,t) - bn(x,y,t)^2 \qquad (4.9)$$

this is a partial differential equation that involves the time derivative with respect to the propagation difection of x-, and y-. For fixed t, the diffusion equation becomes a second-order differential equation in x-, and y-. Solving this into an ordinary differential equation is possible, however to fit the experimental data with the model requires very accurate free-fitting parameter, and therefore finding a unique solution with reliable confidence interval is relatively tedious. We set the initial condition of N_0 (t = 0) for the solution at each x-, and y-, assuming Gaussian excitation beam, and the boundary condition is N = 0 at $x = \infty$, and $y = \infty$. We solve and simulate the equation (4.9) using finite-element analysis [50] using Python code. The inital carrier density (N_0), diffusion coefficient (D), monomolecular recombination coefficient (a), and bimolecular recombination coefficient (b) are set based on our experimental

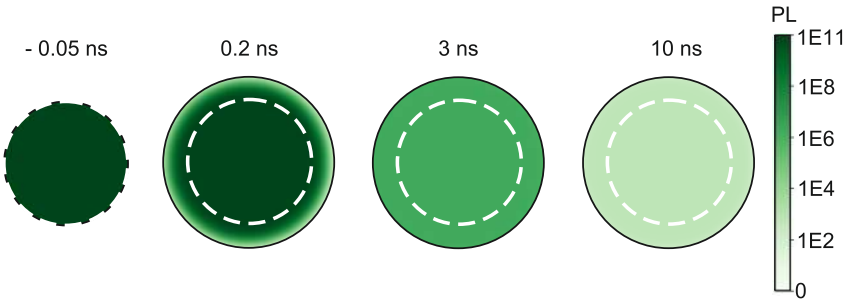

Figure 4.5: Negligible effect of carrier diffusion on PL lifetime. Simulated time dependent PL intensity on symmetric 2-dimensional space showing the diffusion outside the collection spot (white dashed-circle) occurs at ultrafast timescale (0.2 ns), then the spatial PL intensity becomes more diluted and homogeneous at slower timescale.

conditions of 2.9 × 10^{18} cm^{-3}, 0.18 cm^2/s, 0.46 × 10^8 s^{-1}, 1.34 × 10^{-10} cm^3s^{-1}, respectively. **Figure 4.5** shows the simulated evolution of the spatiotemporal PL, where carrier diffusion outside the collection spot (the white dashed-circle) is visible at around sub-nanoseconds timescales. The PL becomes more homogeneous (diluted) at timescales longer than 0.2 ns with reduced PL intensity. This ultrafast transient regime cannot be detected within our measurement accuracy. The pin-hole size of our photodiode detector is 50 μm with a total system magnification of 9x, so the spatial PL counts that can be collected during the measurement come from an area of 30.8 μm^2 (= 50 × 50 μm/9) around the excitation beam [51]. Given the minority carrier diffusion lengths in our samples are less than 0.5 μm, all carriers will recombine before leaving our collection range, such that our setup can be seen as using local excitation with wide-field collection. This suggests that our measurement collects all of the PL emission, even though our actual excitation area could increase slightly from carrier diffusion. In such a case, the spatial variation in PL intensity we measure cannot be explained variations in carrier mobility, as has been suggested for truly confocal system [54].

4.7.2 Steady-state photocarrier grating (SSPG)

Measurement setup

The SSPG is a home-built system developed at AMOLF reviving a method originally developed back in 1980s by Ritter, Zeldov, and Weiser [18]. It is equipped with a CW diode pump solid-state laser (CPS450, Thorlabs) used as an excitation laser source at 450 nm wavelength. The source was first polarized using a linear polarizer (LPVISE 100-A, Thorlabs) before split into two-coherent beams using a beam splitter (CM1-BS013, Thorlabs) creating two optical path lengths. The first path passed through a broadband neutral density filter (NEK01, Thorlabs) and an optical chopper (MC1F10, Thorlabs), and the second passed to a broadband half-wave plate (AHWP05M-600, Thorlabs), both of which were directed toward the sample. The half-wave plate regulates the polarization state of the second path relative to the first path. When the two paths are in the same polarization state, they create an optical interference pattern on the sample surface, whereas no interference is created when the two paths are orthogonally polarized to each other. The period of this optical interference is determined by the angle between the two path beams. We used a controlled rotational stage (CR1-Z7, Thorlabs) and a linear stage (ZLW-1080-02-S-10-L-1500-MK, Igus Drylin, Elcee) to change the angle and maintain the two beams to be continuously overlapping. We monitored the measured ratio of a change in conductivity of the sample as a function of optical grating periods using a lock-in technique (SR830 Stanford dual phase lock-in amplifier). We used a final formulation, as suggested by Balberg [19], to correlate the change of conductivity as a function of grating periods [3, 17]:

$$\left(\frac{1}{1-\beta}\right)^{1/2} = \frac{(2\pi L_D)^2}{(2Z)^{1/2}}\left(\frac{1}{\Lambda^2}\right) + \frac{1}{(2Z)^2} \tag{4.10}$$

where β is the measured ratio of photoconductivity ratio of the sample with and without grating, Λ is the grating period, Z is the grating quality factor, and L_D is the minority carrier diffusion length.

Accounting for depolarization correction

Since sufficient quality of the optical grating depends on the polarization state between the two overlapping beams, we corrected possible influences that could arise from instrumental propagation errors, Fresnel reflection on the sample, and the roughness of the sample surface. First, the instrumental propagation error was estimated by calculating the total error contributions from the PID controller of the linear stage, and rotational stage. We find that the resulting diffusion length (L_D) could drift by fourth-power of the error in the rotational stage angle (θ_R):

$$\Delta L_D = \frac{1}{2} L_D \left[\frac{64 \sin^2\theta}{\cos^8\theta} + \frac{16 \cos^2\left(\frac{\theta}{2}\right)}{\sin^8\left(\frac{\theta}{2}\right)} \right] (\Delta\theta_R)^4 \tag{4.11}$$

where θ is the angle between two beams, ΔL_D is the drifted diffusion length by the error range of the rotational stage ($\Delta\theta_R$). The instrumental errors could be problematic for angles smaller than 1°, corresponding to a grating size of more than ~25 μm (materials with diffusion length of ~2.5 μm). Next, the Fresnel correction was considered because

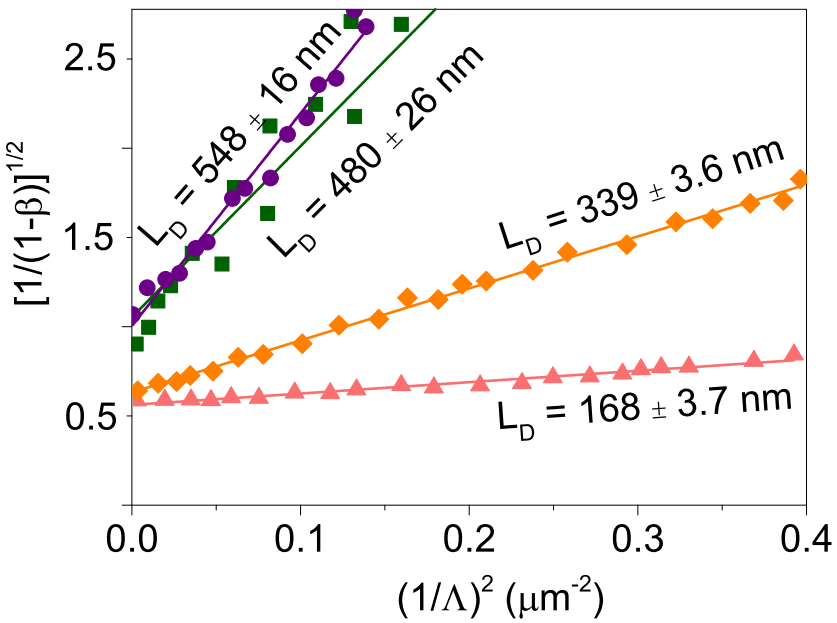

Figure 4.6: Minority carrier diffusion lengths of $CH_3NH_3PbBr_3$ perovskite films with different grain sizes: <54 μm> (purple), <32 μm> (green), <10 μm> (orange), and <4 μm> (pink). Experimental data of a transformation of the photoconductivity ratio (β) as a function of the optical grating size (Λ); known as (inverse) Balberg plot. The L_D values are extracted from the linear fitting of each corresponding dataset

the grating intensity could be reduced as a consequence of the transmittance/reflectance losses of the two beams on the sample [43]. We incorporated this correction into the steady-state transport equation, and final ratio of change in conductivity under grating should be corrected as:

$$\beta_{corr} = \beta \left[\cos^2(\theta_i - \theta_r)\right]^{\alpha-1} \tag{4.12}$$

where the β_{corr} is the corrected conductivity ratio of the sample, and β is the measured conductivity ratio, θ_i is the incident angle, and θ_r is the reflection angle of the beam relative to the normal of the sample surface, and α is the absorption coefficient of the $CH_3NH_3PbBr_3$ perovskite sample. A significant reduction of the conductivity ratio (~8.9 % reduction of grating amplitude) occurs when the angle is more than ~30° between the two beams which corresponds to ~1 micron optical grating period. If not fully corrected, this could be problematic for a sample with less than ~100 nm carrier diffusion length. Finally, to account for the surface roughness effect, we used Müller-Stokes matrix for depolarized light, and the polarization state of the optical grating is the Stokes shift of this matrix [44]. The effect was accounted for an effective medium approximation into the equation (4.12). For a given surface roughness, the maximum deviation of the change in conductivity ($d\sigma$) will be proportional to the fraction of polarized light (f):

$$d\sigma = f\left[I_0\left(1 - \sin\left(2\varphi\delta\cos\Delta\right)\right) - I_B\right] \tag{4.13}$$

where φ, and Δ are the difference in amplitude, and phase component, respectively of the reflectance at normal incident beam (I_0), and at Brewster angle incident beam (I_B). The Brewster angle in our measurement is ~67°. The δ is the film thickness. The largest possible deviation of the change in sample conductivity is ~3% for 250 ± 36 nm $CH_3NH_3PbBr_3$ perovskite film (not sensitive to surface roughness).

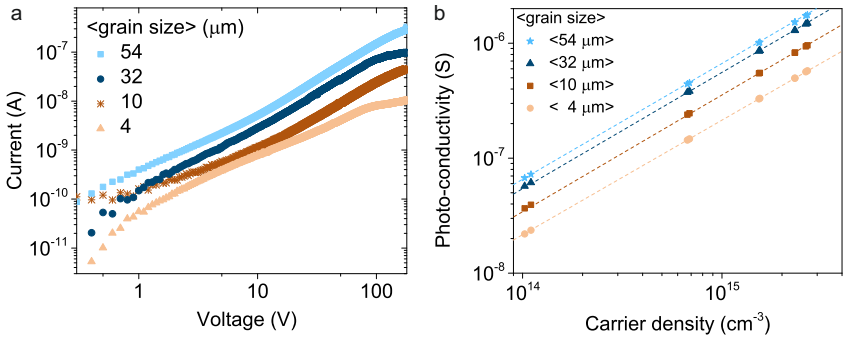

Figure 4.7: (**a**) *I-V* response, and (**b**) photo-conductivity measured on $CH_3NH_3PbBr_3$ perovskite thin-films with different grain sizes.

Conductivity measurement

This is done to determine the net-doping concentration ($|N_e - N_h|$) across the samples with different grain sizes where N_e, and N_h is electron, and hole concentration, respectively. We used a collinear four-probe measurement geometry in the dark to measure the *J-V* curve response of each sample (**Figure 4.7a**) from which we can extract the net-doping concentration as:

$$| N_e - N_h | = \frac{\ln 2}{\pi} \left[\frac{I}{q\mu W V} \right] \tag{4.14}$$

where q is the electrical charge (1.60218×10^{-19} C), μ is the mobility (data in **Figure 4.2c**), W is sample thickness, V is the applied voltage (V), and I is the measured current (A). We found that the net doping concentration is (2.19 to 3.16) × 10^{12} cm^{-3}, (2.28 to 2.92) × 10^{12} cm^{-3}, (2.04 to 2.92) × 10^{12} cm^{-3}, and (1.95 to 2.88) × 10^{12} cm^{-3} for <4 μm>, <10 μm>, <32 μm>, <54 μm> grain size samples, respectively. The precise knowledge of the effective mobilities is required, otherwise the estimation of doping density becomes useless. All films have similar background carrier concentration.

Mobility-lifetime products

The SSPG when coupled with a steady-state photoconductivity measurement can reveal the mobility-lifetime products of the minority- and majority-carriers upon which ambipolar transport of $CH_3NH_3PbBr_3$ thin-film is based [17, 47, 48]. The products can be evaluated by solving the following two coupled equations:

$$\sigma_{photo} = qG\left(\mu_{min}\tau_{min} + \mu_{maj}\tau_{maj}\right) \tag{4.15}$$

$$L_d^2 = C\frac{kT}{q}\frac{\mu_m in\tau_{min}\mu_{maj}\tau_{maj}}{\mu_{min}\tau_{min} + \mu_{maj}\tau_{maj}} \tag{4.16}$$

where σ_{photo} is the sample photo-conductivity, q is the elementary charge, G is the photogenerated charge density (after subtraction with dark conductivity), *kT/q* is thermal voltage at 300 K, C is a proportionality constant (typically 1; see the slope

Table 4.1: Mobility-lifetime products of the minority- and majority-carrier on $CH_3NH_3PbBr_3$ perovskite thin-films with different grain sizes.

<grain size> μm	L_d (nm)	$\mu_{min}\tau_{min}$ (cm^2V^{-1})	$\mu_{maj}\tau_{maj}$ (cm^2V^{-1})
< 4 ± 1.7 >	168 ± 3.7	(1.1 ± 0.5)×10^{-8}	(1.3 ± 0.3)×10^{-5}
< 10 ± 4 >	339 ± 3.6	(2.7 ± 1.8)×10^{-8}	(2.3 ± 0.3)×10^{-5}
< 32 ± 7 >	480 ± 26	(3.4 ± 0.4)×10^{-8}	(3.5 ± 0.5)×10^{-5}
< 54 ± 17 >	548 ± 16	(3.8 ± 0.23)×10^{-8}	(4.1 ± 0.2)×10^{-5}

Figure 4.7b), and L_d is the effective diffusion length measured from the SSPG. The σ_{photo} was obtained based on the generated carrier concentration from *CW* laser excitation at 450 nm, which is equivalent to background carriers from the SSPG measurement. The $\mu_{min}\tau_{min}$, and $\mu_{maj}\tau_{min}$ are the mobility-lifetime product of minority-, and majority- carriers, respectively. Table 4.1 lists the the mobility-lifetime products for minority and majority carriers in our $CH_3NH_3PbBr_3$ thin-films with different grain sizes. Clearly the ratio between $\mu_{min}\tau_{min}$, and $\mu_{maj}\tau_{min}$ is up to three-orders of magnitude, indicating a large asymmetry between electron and hole transport. Therefore unlike $CH_3NH_3PbI_3$ [49], the electrons and holes in $CH_3NH_3PbBr_3$ thin-films do not have similar diffusion lengths. Therefore the diffusion lengths given from SSPG are for the minority carrier, but the measurements are not capable of determining if that is the electron or hole.

4.7.3 Modelling grain size effect

Assumptions

(1) all grains are identical rectangular pillars without any voids (unity filing fraction), so the boundary conditions are always periodic, (2) the grain is uniformly doped inside the pillar volume, (3) the carrier diffusion is regulated by the excess of minority carriers, (4) the grain boundary space charge region is negligible compared to the grain size (no generation current at the grain boundary).

Fourier decomposition

We first describe the 3D steady-state transport equation within one single grain including carrier generation ($\grave{G}$), diffusion ($\grave{D}$), and recombination ($\grave{R}$) terms:

$$\grave{G} - \grave{D} - \grave{R} = 0 \tag{4.17}$$

$$\alpha(\lambda).I_{ph}(\lambda).\exp[-\alpha(\lambda).z] - D\left[\frac{\delta^2\Delta n}{\delta x^2} + \frac{\delta^2\Delta n}{\delta y^2} + \frac{\delta^2\Delta n}{\delta z^2}\right] - \frac{\Delta n}{\tau} \tag{4.18}$$

where Δn is excess of minority carriers (m^{-3}), D is the diffusion coefficient of the minority carrier (m^2/s), x, y, z are the Cartesian coordinate system, $\alpha(\lambda)$ is the wavelength dependence of the absorption coefficient of the $CH_3NH_3PbBr_3$ perovskite, $I_{ph}(\lambda)$ is the incoming photon density (AM 1.5 standard) as a function of wavelength that hits the system at a normal angle (parallel to the z vector), and τ is the minority carrier lifetime. We set the boundary conditions as follow:

$$2D\left[\frac{\delta\Delta n}{\delta x}\right]_{x=\pm G/2} = \pm S_{GB}.\Delta n\left(\pm G/2, y, z\right) \tag{4.19}$$

$$2D\left[\frac{\delta\Delta n}{\delta y}\right]_{y=\pm G/2} = \pm S_{GB}.\Delta n\left(x, \pm G/2, z\right) \tag{4.20}$$

$$2D\left[\frac{\delta\Delta n}{\delta z}\right]_{z=\pm W/2} = \pm S_{FB}.\Delta n\left(x, y, \pm W/2\right) \tag{4.21}$$

where S_{GB} is surface recombination at the grain boundary (m/s), S_{FB} is surface recombination velocity at the top or bottom surfaces that are assumed to be the same (m/s), W is the thickness of the film (m), and G is the grain size (m). The origin of the coordinate system is placed in the center of the square pillar grain (with the dimension of $G \times G \times W$). Physically, the excess carrier density (Δn) always decreases whether it propagates to the plus or minus relative coordinates. We used Fourier decomposition to solve equation (4.18) [20, 21, 26]:

$$\begin{aligned}\Delta n\left(x, y, z\right) = n_0 \int_0^N \int_0^N \left[\frac{A_i A_j\left[\cosh\left(m_{ij}z\right) - C_{ij}\sinh\left(m_{ij}z\right)\right]}{4\sin\left(B_i/2\right)\sin\left(B_j/2\right)}\right] \\ \times\left[B_i B_j \cos\left(B_i x\right)\cos\left(B_i y\right)\right] didj\end{aligned} \tag{4.22}$$

where n_0 is the initial carrier injection which diffuses orthogonally toward x, and y boundaries; the n_0 is not isotropic. The A_i, A_j, C_{ij}, and m_{ij} are coupled Fourier components, all of which contain B_i and B_j as their solution where i and j are indices for x and y directions.

$$A_i = \frac{8\left[\sin\left(B_i G/2\right)\right]^2}{B_i G\left[B_i G + \sin\left(B_i G\right)\right]} \tag{4.23}$$

$$C_{ij} = \frac{Dm_{ij}\sinh\left(2m_{ij}W\right) + S_{FB}\cosh\left(2m_{ij}W\right)}{Dm_{ij}\cosh\left(2m_{ij}.W\right) + S_{FB}\sinh\left(2m_{ij}W\right)} \tag{4.24}$$

$$m_{ij} = \sqrt{\left(B_i^2 + B_j^2 + L^{-2}\right)} \tag{4.25}$$

$$B_i = \tan^{-1}\left(\frac{B_i G}{2}\right)\left(\frac{S_{GB}}{2D}\right) \tag{4.26}$$

Simultaneously, j mode components were obtained by replacing i with j. The L is the bulk diffusion length of $CH_3NH_3PbBr_3$ perovskite (the asymptotic values of measured diffusion lengths). Finally, the effective diffusion length (L_{eff}) was obtained from the inverse proportional product of the whole Fourier components:

$$L_{eff} = \left[\int_0^N \int_0^N \left(A_i A_j C_{ij} m_{ij}\right) didj\right]^{-1} \tag{4.27}$$

Up to the first term in a truncated Fourier expansion, we can approximate a dependence of carrier diffusion length to grain size as [21, 24]:

$$L_v = L\left[\frac{1 + \frac{S_{FB}L}{D}.\tanh\frac{2W}{L}}{\frac{S_{FB}L}{D} + \tanh\left(\frac{2W}{L}\right)}\right] \tag{4.28}$$

$$L_h = \frac{L_v}{\sqrt{1 + \frac{2S_{GB}L_v^2}{DG}}} \tag{4.29}$$

Here L_v and L_h can be associated with the diffusion lengths in the vertical and horizontal directions, respectively, which are coupled. By knowing such correlation between the effective diffusion length (L_{eff}) and grain size (G), we can estimate the correlation between grain size and carrier lifetime (τ), and mobility (μ). To find the dependence of τ and μ on grain size, we used either of those two as a free fitting parameter whose initial values were fitted to the experimental data points.

J-V Solar cell modelling

We modelled the solar cell *J-V* curve using 2 diode equations both of which differ not only in their ideality factors but also in their dark-current recombination. Under illumination, the *J-V* relation is expressed as [45]:

$$J_L = J_{01}\left[\exp\left[\frac{V}{n_{01}V_t}\right] - 1\right] + J_{02}\left[\exp\left[\frac{V}{n_{02}V_t}\right] - 1\right] - J_{sc} \tag{4.30}$$

$$J_{01} = \frac{qD(n_i)^2}{N_A}\frac{1}{L_{eff}} \tag{4.31}$$

$$J_{02} = \frac{\pi D n_i V_t}{\sqrt{\frac{2N_D V_{bi}}{q\epsilon_s}}}\frac{1}{L_{eff}^2} \tag{4.32}$$

where V_t is the thermal voltage at 300 K (0.02586 V), D is the diffusion coefficient of the minority carrier (m^2/s), n_i is the intrinsic carrier concentration (m^{-3}), N_A is the acceptor doping density in the bulk grain (m^{-3}), N_D is the acceptor doping density at the grain boundary (m^{-3}), V_{bi} is the built-in potential near the space charge region of the grain boundary (V), ϵ_s is the static dielectric constant of the $CH_3NH_3PbBr_3$ perovskite, q is the electronic charge (1.6022×10^{-19} C), and L_{eff} is the effective diffusion length as described in equation (4.27). The first diode represents the recombination current inside the grain (J_{01}), and the second is at the grain boundary (J_{02}). The J_{sc} is the short-circuit current density of the solar cell which was separately determined using a finite element simulation (Lumerical, DEVICE) [38, 46] The hypothetical solar cell structure is composed of FTO/TiO_2/$CH_3NH_3PbBr_3$/NiO_x/Al layers.

PLQY modelling

We modelled the photoluminescence quantum yield (PLQY) based on its own definition as the ratio of the number of photons emitted to the number of photons absorbed:

$$PLQY = \frac{bn^2}{an + bn^2 + cn^3} \tag{4.33}$$

where a, b, and c are the recombination coefficient for the monomolecular, radiative bimolecular, and Auger processes ($\sim 10^{-27}$ - 10^{-29} cm^6/s) [41, 42], respectively, where n is the volume averaged electron-hole concentration in a 250 nm thickness $CH_3NH_3PbBr_3$ film. The total effective carrier lifetime is determined by a convolution of bulk, top-bottom surface, and grain boundary interface recombination, and therefore we formulate the monomolecular recombination coefficient (a) as a function of grain size (G) effect as based on the first order limit of the Fourier coefficient:

$$\frac{1}{\tau_{eff}} = \frac{2S_{GB}}{G} + \frac{D}{(LA)^2} = a \tag{4.34}$$

$$A = \frac{1 + \frac{S_{FB}L}{D}\tanh\left(\frac{W}{L}\right)}{\frac{S_{FB}L}{D} + \tanh\left(\frac{W}{L}\right)} \tag{4.35}$$

by plugging equations (4.34) and (4.35) to equation (4.33), we find:

$$PLQY = \frac{1}{1 + \left(\frac{2S_{GB}}{G} + \frac{D}{(LA)^2}\right)\left(\frac{1}{b}\right)n^{-1} + \left(\frac{c}{b}\right)n} \tag{4.36}$$

The peak of the *PLQY* is determined by the second term of the denominator, while the range of *PLQY* broadening is determined by the third term of the denominator.

References

[1] O. G. Reid, M. Yang, N. Kopidakis, K. Zhu, and G. Gumbles, *Grain-size-limited mobility in methylammonium lead iodide perovskite thin films*, ACS Energy Lett. **1**, 5 (2016).

[2] H. D. Kim, H. Ohkita, H. Benten, and S. Ito, *Photovoltaic performance of perovskite solar cells with different grain sizes*, Adv. Mater. **28**, 6 (2016).

[3] G. W. P. Adhyaksa, L. W. Veldhuizen, Y. Kuang, S. Brittman, R. E. I. Schropp, and E. C. Garnett, *Carrier diffusion lengths in hybrid perovskites: processing, composition, aging, and surface Passivation Effects*, Chem. Mater. **28**, 5 (2016).

[4] M. Yang, Y. Zeng, Z. Li, D. H. Kim, C-S. Jiang, J. v. d. Lagemaat, and K. Zhu *Do grain boundaries dominate non-radiative recombination in $CH_3NH_3PbI_3$ perovskite thin films?*, Phys.Chem.Chem.Phys. **19**, 8 (2017).

[5] D. Fisher, F. Saouma, J. Jang, and T. P. Dhaka *The effect of grain improvement on carrier lifetime in perovskite solar devices*, Photovoltaic Specialists Conference (PVSC), 2016 IEEE 43rd **43**, 5 (2016).

[6] X. Ren, Z. Yang, D. Yang, X. Zhang, D. Cui, Y. Liu, Q. Wei, H. Fana, and S. (F). Liu *Modulating crystal grain size and optoelectronic properties of perovskite films for solar cells by reaction temperature*, Nanoscale **8**, 7 (2016).

[7] W. Nie, H. Tsai, R. Asadpour, J-C. Blancon, A. J. Neukirch, G. Gupta, J. J. Crochet, M. Chhowalla, S. Tretiak, M. A. Alam, H-L. Wang, and A. D. Mohite *High-efficiency solution-processed perovskite solar cells with millimeter-scale grains*, Science **347**, 5 (2015).

[8] J. S. Yun, A. Ho-Baillie, S. Huang, S. H. Woo, Y. Heo, J. Seidel, F. Huang, Y-B. Cheng, and M. A. Green, *benefit of grain boundaries in organic?inorganic halide planar perovskite solar cells*, J.Phys.Chem.Lett. **6**, 875 (2015).

[9] J. Haruyama, K. Sodeyama, L. Han, and Y. Tateyama *Termination dependence of tetragonal $CH_3NH_3PbI_3$ surfaces for perovskite solar cells*, J. Phys. Chem. Lett. **16**, 7 (2014).

[10] T. J. Jacobsson, J-P. Correa-Baena, E. H. Anaraki, B. Philippe, S. D. Stranks, M. E. F. Bouduban, W. Tress, K. Schenk, J. Teuscher, J. E. Moser, H. Rensmo, and A. Hagfeldt *Unreacted PbI_2 as a double-edged sword for enhancing the performance of perovskite solar cells*, JACS. **138**, 13 (2016).

[11] Q. Chen, H. Zhou, T-B. Song, S. Luo, Z. Hong, H-S. Duan, L. Dou, Y. Liu, and Y. Yang *Controllable self-induced passivation of hybrid lead iodide perovskites toward high performance solar cells*, Nano Lett. **14**, 6 (2014).

[12] G. E. Eperon, D. Moerman, and D. S. Ginger *Anticorrelation between local photoluminescence and photocurrent suggests variability in contact to active layer in perovskite solar cells*, ACS Nano **10**, 9 (2016).

[13] S. Y. Leblebici, L. Leppert, Y. Li, S. E. Reyes-Lillo, S. Wickenburg, E. Wong, J. Lee, M. Melli, D. Ziegler, D. K. Angell, D. F. Ogletree, P. D. Ashby *Facet-dependent photovoltaic efficiency variations in single grains of hybrid halide perovskite*, Nature Energy **1**, 16093 (2016).

[14] D. W. deQuilettes, S. M. Vorpahl, S. D. Stranks, H. Nagaoka, G. E. Eperon, M. E. Ziffer, H. J. Snaith, D. S. Ginger, *Impact of microstructure on local carrier lifetime in perovskite solar cells*, Science **348**, 683 (2015).

[15] D. Shi, V. Adinolfi, R. Comin, M. Yuan, E. Alarousu, A. Buin, Y. Chen, S. Hoogland, A. Rothenberger, K. Katsiev, Y. Losovyj, X. Zhang, P. A. Dowben, O. F. Mohammed, E. H. Sargent, O. M. Bakr, *Low trap-state density and long carrier diffusion in organolead trihalide perovskite single crystals*, Science **347**, 519 (2015).

[16] R. J. Stoddard, F. T. Eickemeyer, J. K. Katahara, and H. W. Hillhouse, *Correlation between photoluminescence and carrier transport and a simple in situ passivation method for high-bandgap hybrid perovskites*, J. Phys. Chem. Lett. **8**, 10 (2017).

[17] L. W. Veldhuizen, G. W. P. Adhyaksa, M. Theelen, E. C. Garnett, and R. E. I. Schropp, *Benchmarking photoactive thin-film materials using a laser-induced steady-state photocarrier grating*, Prog.in Photovolt. **25**, 9 (2017).

[18] D. Ritter, E. Zeldov, K. Weiser, *Steady-state photocarrier grating technique for diffusion length measurement in photo-conductive insulators*, Appl. Phys. Lett. **53**, 992 (1988).

[19] I. Balberg, A. E. Delahoy, and H. A. Weakliem, *Ambipolar diffusion length measurements on hydrogenated amorphous silicon p-i-n structures*, App. Phys. Let. **53**,1949 (1988).

[20] N. C. Halder and T. R. Williams, *Grain boundary effects in polycrystalline silicon solar cells II: numerical calculation of the limiting parameters and maximum efficiency*, Solar Energy Materials and Solar Cells **8**,23 (1983).

[21] J. Dugas, *3D modelling of a reverse cell made with improved multicrystalline silicon wafers*, Solar Energy Materials and Solar Cells **18**,71 (1994).

[22] S. Banerjee and H. Saha, *Grain boundary effects in polycrystalline silicon solar cells*, Solar Cells **28**,77 (1990).

[23] A. B. Sproul, *Dimensionless solution of the equation describing the effect of surface recombination on carrier decay in semiconductors*, J.Appl.Phys. **76**,4 (1994).

[24] A. B. Sproul and C. H. Seager *The dc voltage dependence of semiconductor grain-boundary resistance*, J.Appl.Phys. **50**,9 (1978).

[25] D. P. Joshi and D. P. Bhatt *Theory of grain boundary recombination and carrier transport in polycrystalline silicon under optical illumination*, IEEE Trans. Elect. Dev. **37**,13 (1990).

[26] R. Brendel, *Thin-Film Crystalline Silicon Solar Cells Physics and Technology*, Willey-VCH Verlag GmbH, Weinheim, 2003.

[27] S. M. Sze and K. K. Ng, *Physics of Semiconductor Devices*, John Wiley-Sons, Inc., New Jersey, 2007.

[28] W. Shockley, *Electron and Holes in Semiconductors*, D.Van Nostrand Company, Inc., New York, 1950.

[29] Y. Yang, Y. Yan, M. Yang, S. Choi, K. Zhu, J. M. Luther, and M. C. Beard, *Low surface recombination velocity in solution-grown $CH_3NH_3PbBr_3$ perovskite single crystal*, Nature Comm.**6**,7961 (2015).

[30] B. G. Mendis, L. Bowen, and Q. Z. Jiang, *A contactless method for measuring the*

recombination velocity of an individual grain boundary in thin-film photovoltaics, Appl. Phys. Lett. **97**, 3 (2010).

[31] J. Qualid, C. M. Singal, J. Dugas, J. P. Crest, and H. Amzil, *Influence of illumination on the grain boundary recombination velocity in silicon*, Appl. Phys. Lett. **55**, 11 (1984).

[32] H. C. Sio, S. P. Phang, and D. Macdonald, *Imaging surface recombination velocities of grain boundaries in multicrystalline silicon wafers via photoluminescence*, Sol. RRL. **1**, 4 (2017).

[33] M. Gloeckler, J. R. Sites, and W. K. Metzger, *Grain-boundary recombination in Cu(In,Ga)Se_2 solar cells*, Appl. Phys. Lett. **98**, 10 (2005).

[34] W. K. Metzger, I. L. Repins, M. Romero, P. Dippo, M. Contreras, R. Noufi, and D. Levi, *Recombination kinetics and stability in polycrystalline Cu(In,Ga)Se2 solar cells*, Thin Sol. Films **517**, 5 (2009).

[35] R. Sheng, A. Ho-Baillie, S. Huang, S. Chen, X. Wen, X. Hao, and M. A. Green, *Methylammonium lead bromide perovskite-based solar cells by vapor-assisted deposition*, JPCC **7**, 5 (2015).

[36] Y. Yang, Y. Mengjin, D. T. Moore, Y. Yan, E. M. Miller, K. Zhu, and M. C. Beard, *Top and bottom surfaces limit carrier lifetime in lead iodide perovskite films*, Nature Energy **2**, 7 (2017).

[37] Y. Su, C. Liu, S. Brittman, J. Tang, A. Fu, N. Kornienko, Q. Kong, and P. Yang, *Single-nanowire photoelectrochemistry*, Nature Nano. **11**, 4 (2016).

[38] G. W. P. Adhyaksa, E. Johlin, and E. C. Garnett, *Nanoscale Back Contact Perovskite Solar Cell Design for Improved Tandem Efficiency*, Nature Lett. **17**, 7 (2017).

[39] C. Lanczos, *An iteration method for solution of the Eigenvalue problem of linear differential and integral operators*, J. Res. The Nat. Bureau of Stand. **45**, 28 (1950).

[40] T. W. Crothers, R. L. Milot, J. B. Patel, E. S. Parrott, J. Schlipf, P. Müller-Buschbaum, M. B. Johnston, and L. M. Herz *Photon reabsorption masks intrinsic bimolecular charge-carrier recombination in $CH_3NH_3PbI_3$ perovskite*, Nano Lett. **17**, 8 (2017).

[41] J. M. Richter, M. Abdi-Jalebi, A. Sadhanala, M. Tabachnyk, J. P. H. Rivett, L. M. Pazos-Outon, K. C. Godel, M. Price, F. Deschler, and R. H. Friend *Photon reabsorption masks intrinsic bimolecular charge-carrier recombination in $CH_3NH_3PbI_3$ perovskite*, Nature Comm. **8**, 13941 (2016).

[42] Y. Yang, M. Yang, Z. Li, R. Crisp, K. Zhu, and M. C. Beard *Comparison of recombination dynamics in $CH_3NH_3PbBr_3$ and $CH_3NH_3PbI_3$ perovskite films: influence of exciton binding energy*, J. Phys. Chem. Lett. **6**, 5 (2015).

[43] J. P. Nicholson *Fresnel Correction to measurements of ambipolar diffusion length*, J. App. Phys. **88**, 4 (2000).

[44] H. Tomkins and E. A. Irene, *Handbook of Ellipsometry*, William Andrew, New York 2005.

[45] K. Taretto, U Rau, and J. H. Werner *Method to extract diffusion length from solar cell parameters?Application to polycrystalline silicon*, J. App. Phys. **93**, 9 (2003).

[46] Lumerical Inc., *DEVICE CT Solution*, Lumerical, Canada 2017.

[47] N. Beck, N. Wyrsch, Ch. Hof, and A. Shah*Mobility lifetime product-A tool for correlating a-Si:H film properties and solar cell performances*, J. App. Phys. **79**, 9361 (1996).

[48] I. Levine, S. Gupta, T. M. Brenner, D. Azulay, O. Millo, G. Hodes, D. Cahen, and I. Balberg*Mobility-lifetime products in $MAPbI_3$ films*, J. Phys. Chem. Lett. **7**, 5219 (2016).

[49] G. Xing, N. Mathews, S. Sun, S. S. Lim, Y. M. Lam, M. Gätzel, S. Mhaisalkar, and T. C. Sum*Long-range balanced electron- and hole-transport lengths in organic-inorganic*

$CH_3NH_3Pb_3$, Science **342**, 344 (2013).

[50] A. Logg, K-A. Mardal, and G. Wells, *Automated Solution of Differential Equations by the Finite Element Method*, Springer, Amsterdam 2012.

[51] S. Wilhelm, B. Grõbler, M. Gluch, and H. Heinz, *Confocal Laser Scanning Microscopy*, Carl Zeiss, Jena 2017.

[52] B. W. Silverman*Kernel density estimation using the fast Fourier transform*, J.Royal.Statis.Soc. **31**, 7 (1982).

[53] T. Myint-U and L. Debnath, *Linear Partial Differential Equations for Scientists and Engineers*, Printice Hall, New Jersey 1987.

[54] D. W. deQuilettes, S. Jariwala, S. Burke, M. E. Ziffer, J. T. W. Wang, H. J. Snaith, and D. S. Ginger *Tracking photoexcited carriers in hybrid perovskite semiconductors: trap-dominated spatial heterogeneity and diffusion*, ACS Nano **11**, 11488 (2017).

5

Nanoscale Back Contact Perovskite Solar Cells for Improved Tandem Efficiency

Tandem photovoltaics, combining absorber layers with two distinct band gap energies into a single device, provide a practical solution to reduce thermalization losses in solar energy conversion. Traditionally, tandem devices have been assembled using two-terminal (2-T) or four-terminal (4-T) configurations; the 2-T limits the tandem performance due to the series connection requiring current matching, while the standard 4-T configuration requires at least three transparent electrical contacts, which reduce the total collected power due to unavoidable parasitic absorption. Here, we introduce a novel architecture based on a nanoscale back-contact for a thin-film top cell in a three terminal (3-T) configuration. Using coupled optical-electrical modelling, we optimize this architecture for a planar perovskite-silicon tandem, highlighting the roles of nanoscale contacts to reduce the required perovskite electronic quality. For example, with an 18 % planar silicon base cell, the 3-T back contact design can reach 32.9 % tandem efficiency with a 10 μm diffusion length perovskite material. Using the same perovskite quaility, the 4-T and 2-T configurations only reach 30.2 % and 24.8 %, respectively. We also confirm that the same 3-T efficiency advantage applies when using 25 % efficient textured silicon base cells. Furthermore, because our design is based on the individual subcells being back-contacted, further improvements can be readily made by optimizing the front surface, which is left free for additional antireflective coating, light trapping, surface passivation, and photoluminescence outcoupling enhancements.

5.1 Introduction

Thermalization of hot electrons to the band edge is the largest source of power loss (~40 %) in photovoltaic solar energy-conversion [1]; reducing this loss provides the largest opportunity to reach ultrahigh efficiency solar cells. Although many strategies have been proposed, only multijunction concepts have currently led to efficiency values above the single junction Shockley-Queisser (S-Q) limit [2–7]. Unfortunately, tandem solar cells are currently too expensive to use without light concentration, which requires expensive optics, solar tracking, and often active cooling. The rise of high efficiency, inexpensive thin-film solar cells with band gaps suitable for tandem solar cells (e.g., halide perovskites) have renewed interest in making tandem solar cells for 1-sun application [7–13].

Traditionally, tandem solar cells have been fabricated in either 2- or 4-terminal configurations [14], representing different extrema in the space of optical and electronic coupling. The 2-terminal (2-T) design is monolithic and requires series interconnected cells, while the 4-terminal (4-T) design is mechanically stacked and enables independently connected cells. While 2-T configurations can benefits from optically coupling the top and bottom cells to prevent loss and reflections between the devices, they remain electronically coupled as well, forcing the two cells to be current matched. Even with an optimal design, this current matching condition can only be reached for a single optical spectrum; under diffuse light conditions, the large shifts in illumination spectrum can cause large efficiency losses (e.g., up to ~11% relative in energy-yield disadvantage [15, 16]). Conversely, 4-T devices benefit from electronically decoupling the two cells, alleviating the need for current matching, but thick spacer layers generally cause the tandem to lose the optical benefits of the monolithically stacked 2-T tandems, and the additional contact again introduces a ~10 % relative efficiency loss [17]. The 3-terminal (3-T) configurations present a possibility for allowing the tandem cells to be optically coupled but electrically decoupled, gaining the advantages of both standard configurations, while avoiding their main drawbacks [18–23].

Here, we introduce a new design for a perovskite solar cell using embedded nanoscale back contacts in tandem with interdigitated back contact (IBC) silicon cells, coupled in a 3-T configuration (**Figure 5.1**). Because of the double back contact design, only one (infrared) transparent contact is required (located between the perovskite and silicon cells), reducing reflection and parasitic absorption losses. Because the top of our tandem cell does not require a contact, this design can leave the front surface free for texturing, anti-reflection coating, and surface passivation. These effects are not optimized in our current analysis but could lead to higher absorption due to reduced reflection, and large gains in open circuit voltage due to enhanced light outcoupling or directional emission [24–26]. We use coupled optical-electrical simulations to compare the performance of planar and textured tandem cells in 2-, 3-, and 4-T configurations. The 3-T and 4-T planar tandem cells have the potential to exceed the single junction S-Q efficiency limit of ~33 % using a perovskite with minority carrier diffusion length, L_D, of at least 12 and 24 μm for 3-T and 4-T tandems, respectively. The 2-T configuration cannot reach such high efficiency values even for perfect perovskite quality (optical

limit). More significantly, using a lower quality perovskite material with $L_D = 0.8\mu$m, only our 3-T configuration is able to surpass the 26.3 % world record [27] for a single junction (textured/nonplanar) crystalline silicon solar cell. The improved performance of our design relies on the embedded nanowire grid back contact that benefits from three main effects. First, enhanced charge generation near the nanogrid contact due to nanophotonics effects relaxes the diffusion length constraint for high efficiency tandems. Second, decoupling the carrier collection of the two devices removes the need for current matching (as in 2-T). And third, eliminating the front transparent electrode increases the current, particularly in the top cell. This design can be used as a furture building block to create multijunction back contact photovoltaics.

5.2 Theory

The 3-T design considered here is composed of a perovskite cell with embedded nanoscale back contacts as the top cell, and an interdigitated back contact (IBC) silicon cell as the bottom cells, as depicted in **Figure 5.1**. Our top cell design differs from previous works reported on back contact perovskite [28] and thin film [18, 29] solar cells because it incorporates only a single patterned contact (an embedded nanogrid network) and uses a carrier-selective layer on the front surface of the bottom silicon cell as the second contact. For all simulations, we use a top surface of fused-SiO_2 representative of the front glass layer on a finished module. The nanogrid network is composed of an insulating layer (100 nm thick Al_2O_3) and a metal contact (100 nm thick Au) coated with metal oxide hole transporting layer (10 nm thick NiO_x). The grid width is 60 nm with pitch sizes from 0.25 to 6 μm. This can be fabricated lithographically [30, 31] or using random nanowire mesh [32, 33] structures as a self-aligned etch mask [34]. We use a $CH_3NH_3PbI_3$ perovskite (E_g ~1.55 eV) absorber, where the thickness is optimized between 0.05 and 1 μm for all configurations. Although the bandgap of this perovskite is not ideal (~1.55 eV *versus* the ~1.78 eV ideal E_g) for tandem with silicon (E_g ~1.12 eV), all high-efficiency single junction perovskite devices to date have consisted of the $CH_3NH_3PbI_3$ material or a variation with a nearly identical band gap [35].

The electrons generated from the perovskite cell are collected by a metal oxide electron transporting layer (10 nm thick TiO_2) and transferred to the IBC silicon cell via a tunneling layer. In this case, the electron contact of the IBC silicon cell will receive electrons both from the perovskite and silicon cells. Holes from the perovskite will be collected directly by the metal nanowire contact grid, via the hole transporting layer. The efficiency of electron transmission from the top to the bottom cell depends on the quality of the tunneling layer composed of n^{++}Si layers (called front floating emitter/FFE); this design is just one possibility mirroring the original design of FFE [36, 37]. The FFE can be thought of as the negative electrode representing a common ground between the devices, with the potential of the two cells being determined by their positive electrodes. As a result, the working principle of the 3-T IBC is equivalent to a 4-T, in which the two cells are electrically decoupled. This thereby

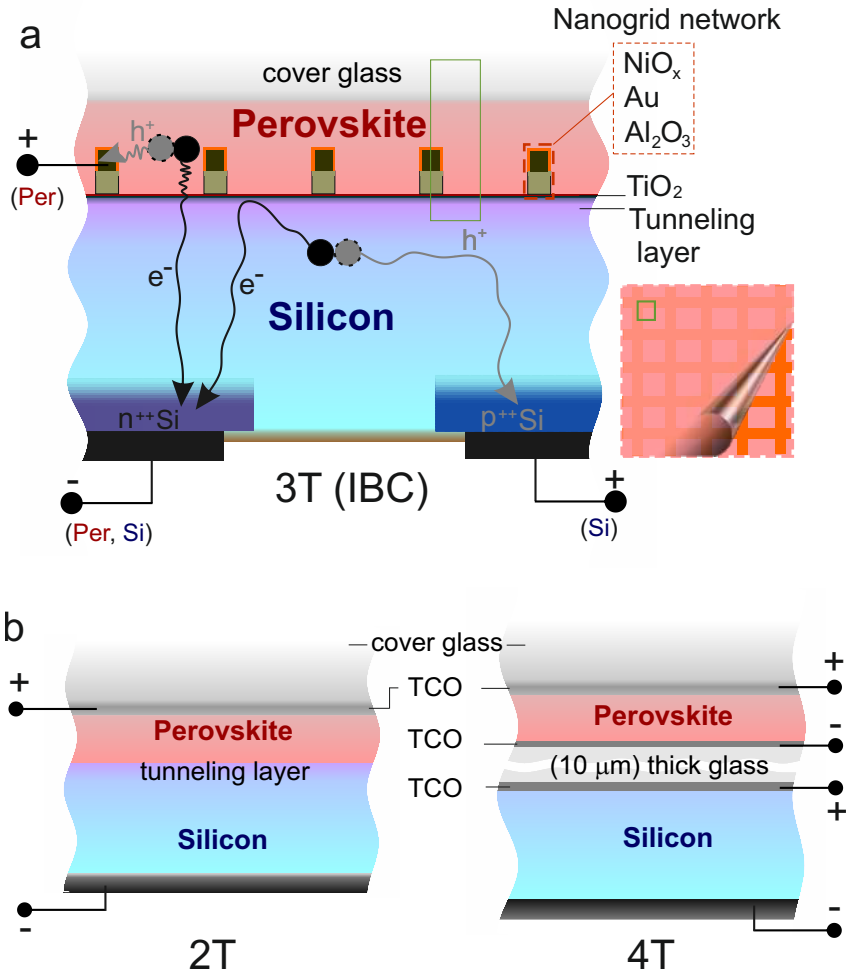

Figure 5.1: Schematic designs of perovskite-silicon tandem solar cells. (**a**) Double back contact with three-terminal configuration (3-T (IBC)). The top open space (cover glass) is free providing opportunities for light-trapping, anti-reflective coating, surface passivation, directional emission or enhanced photoluminescence outcoupling. The nanoscale embedded grid is composed of NiO_x hole-transporting layer (orange), Au metal contact (dark-brown), and Al_2O_3 dielectric-insulating layer (light-brown). The negative polarity is shared between the perovskite (Per.) and Silicon (Si.) cells in the n++Si (emitter) back contact silicon cell. Minority carriers from the silicon cell (e^-) are collected then re-injected by the tunnel layer containing $n^{++}Si$ (front-floating emitter). The inset shows a schematic top view with 3D simulated unit cell indicated as a light-green box (half-pitch square size). (**b**) Traditional tandem configurations with two-terminal (2-T) and four-terminal (4-T) configurations; details in the Supporting information. These cross-sectional views are not drawn to scale (perovskite thickness ranges between 0.05 to 1 μm, and the silicon is 180 μm).

removes the current matching condition (present in 2-T design), while still allowing for monolithic fabrication. The presence of a nanogrid network optically couples the top and bottom cells, while also modifying the generation profile in the perovskite material, which when optimized can reduce the diffusion length requirements, and increase the optical path length in the silicon cell.

To assess the potential device performance, and hence the benefits of our architecture, we construct an optoelectronic model that couples the device optical and electrical response, as schematically described in **Figure 5.2**. We first simulate the optical response of the subcells and then use the output of the optical generation rate response as an input for our electronic modeling. The optical input is the standard solar spectrum (AM 1.5) from 300 to 1300 nm with 1 nm spectral resolution. For the perovskite cell, the light propagation is computed with a wave optics approach with all optical interference in the interlayer structures simulated using three-dimensional (3D) finite-difference time-domain calculations (FDTD, Lumerical Solutions software [38]). The optical transmission from the top cell is used as the optical input to the bottom cell, which due to the large thickness is simulated based on a ray-optics approach, using a rigorous polarization ray tracing (PV lighthouse, OPAL [39]). The values of the optical constants for all materials were obtained either from spectroscopic ellipsometry measurements or taken from the literature (Supporting information). From the optical constants and computed electric field, we can calculate the charge generation rate as a function of position and use that as an input to solve electrostatic and drift-

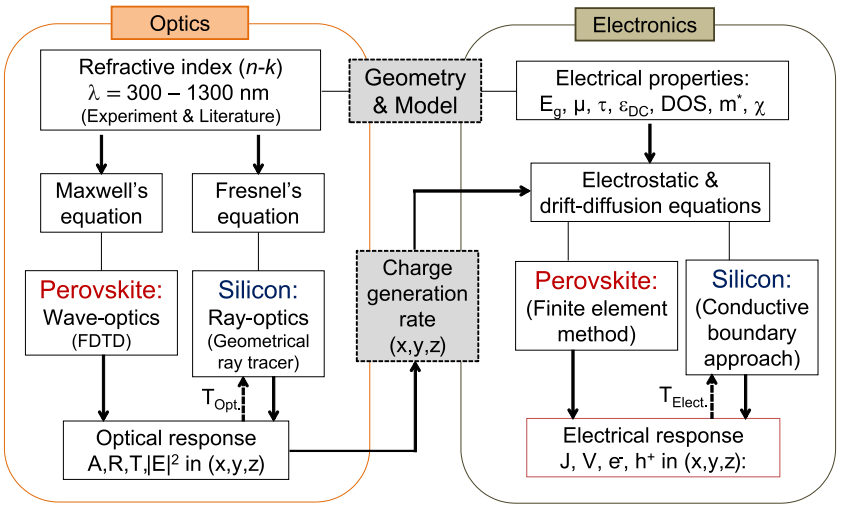

Figure 5.2: Coupled optical-electrical simulation setup. The output of the optical responses, via spatial information on charge generation rate, is used as the input for the electronics modeling. A is absorption, R is reflection, T is transmission, $|E|^2$ is electric field intensity, E_g is electronic bandgap, μ is charge mobility, ϵ_{DC} is DC permittivity, DOS is density of states, m^* is charge effective mass, χ is work function, J is current, V is voltage, e^- is number of electrons, h^+ is number of holes, and (x, y, z) is three-dimensional spatial information. Unless specified, all optoelectronic modeling is based on 3D simulation.

diffusion transport equations for each material. Realistic values of electrical bandgaps, dielectric permittivity, electron/hole effective mass, electron affinity, mobility, lifetime, density of states, and equivalent resistivity of all materials are provided as input to the simulation (Supporting information). For computational efficiency, we solved the transport equation using a 3D finite element method (Lumerical Solutions, Device Multiphysics [40]) for the perovskite cell using a conductive boundary approach (PV lighthouse, Quokka [41]) for IBC silicon cell. Unless specified, the coupled optical-electrical simulations were fully conducted in 3D (see Supporting information for further details).

To benchmark the 3-T double-IBC perovskite-silicon tandem solar cell performance, we compare it with standard 2-T and 4-T configurations using commensurate material selections (details in schematic designs, proven compatibility of all materials involved are described in Supporting information). The 2-T is composed of a transparent conductive oxide (TCO) as a top contact, a tunnel junction (between the perovskite and silicon), and a high quality planar silicon cell (front and back contact) with an 18.8 % power conversion efficiency (the equivalent of 25 % efficiency with an optimized textured front surface and an SiN_x antireflective coating). The 4-T is composed of three TCO layers (two for the perovskite cell, and one for Si top contact), a 10μm thick glass insulating layer between the perovskite and silicon, and an identical silicon cell as used in the 2-T. All configurations use metal oxide layers both for electron and hole transporters (as opposed to organic layers, e.g. Spiro-OMeTAD, PCBM, PEDOT:PSS) in order to minimize the parasitic absorption.

5.3 Optically limited performance

We begin by investigating the purely optical performance of the three configurations, equivalent to setting the diffusion length for all materials to infinity (internal quantum efficiency of 100 %, **Figure 5.3a-c**). As the perovskite thickness increases, the absorption shifts from the silicon to perovskite. For electrically decoupled devices, this is uniformly beneficial as the wider band gap of perovskite allows an increased power generation, but for current-matched devices a clear optimal thickness is visible. For the 2-T tandem (**Figure 5.3a**), we see that the tandem device exceeds the Si limit (~29.4 % Auger-limited efficiency [42]) for perovskite layers from ~200 to 400 nm thick with the maximum efficiency of 31.7 % with a 250 nm thick perovskite layer. The falloff in efficiency above 400 nm is due to the current matching condition required for the 2-T series connection (total current is limited by the cell having lower current).

The limiting efficiency is higher for the 4-T configuration because the top and bottom cells are electrically decoupled. For the 4-T tandem (**Figure 5.3b**), the Si limit can be exceeded if the perovskite thickness is greater than ~100 nm (with a TCO thickness of 100 nm). The TCO in the 4-T tandem also acts as an antireflective coating, as the TCO thickness was optimized to minimize reflection (Supporting information). The maximum 4-T tandem efficiency is 36.5 % within the 1 μm perovskite thickness limit chosen for practical feasibility (and comparison with diffusion-limited devices

later on). The asymptotic efficiency for the 4-T tandem is 36.6 %.

The 3-T IBC tandem (**Figure 5.3c**) improves further the maximum tandem efficiency, reaching 37.9 % at 5.125 μm pitch and 1 μm perovskite thickness (also the asymptotic limit). The efficiency oscillates with thickness for both the 2- and 3-T, showing that in these cases, unlike the 4-T configuration, the perovskite and silicon are optically coupled, which improves the tandem performance. However, unlike the 2-T, the two cells are electrically decoupled in the 3-T IBC with additional optical coupling benefits, which enables the higher efficiency.

5.4 Coupled optoelectronic simulation

To evaluate the realistic performance of the three configurations, we examine two different scenarios for perovskite material quality by varying the minority carrier diffusion length (**Figure 5.3d-f**); we use diffusion lengths for the $CH_3NH_3PbI_3$ of 0.5 μm and 10 μm representing a realistic and optimistic perovskite quality, respectively. The corresponding efficiency values of the perovskite materials optimized as single junction devices are 11.6 % and 24.5 % with 0.5 and 10 μm diffusion lengths and perovskite film thickness of 0.45 and 1 μm, respectively. The tandem performance is computed with high quality planar single-junction Si cells of 18.8 % single-junction efficiency; these correspond to simulated efficiency values of textured devices (with optimized antireflective coatings) of 23.3 % for front and rear contacted Si and 25 % for IBC Si.

For the 2-T configuration (**Figure 5.3d**), the tandem efficiency does not exceed the planar Si (18.8 %) unless the high quality perovskite is used. Additionally, as the diffusion length is reduced, the maximum efficiency is shifted to configurations with thicker perovskite films due to the current matching constraint, a trend that optical simulation alone cannot predict, demonstrating the importance of coupled optoelectronic simulations in tandem devices. The maximum 2-T tandem efficiency using 0.5 μm and 10 μm perovskite diffusion lengths are 18.5 % (at 400 nm thick), and 24.8 % (at 300 nm thick), respectively.

Similarly, for the 4-T configuration (**Figure 5.3e**), the tandem efficiency does not exceed the single junction planar Si limit (18.8 %), unless a high quality perovskite is used. The maximum 4-T tandem efficiency using 0.5 μm, and 10 μm perovskite carrier diffusion lengths are 18.8 % (at 450 nm thick), and 30.2 % (at 950 nm thick), respectively.

In the 3-T tandem configuration (**Figure 5.3f**), the lower quality perovskite (0.5 μm diffusion length) can be used to exceed the efficiency of planar IBC Si of 18.9 %, which is in contrast to the 2-T and 4-T tandems. In this case, the simulated tandem efficiencies are well above the planar IBC Si limit for perovskite thickness up to 850 nm. Thickness below 250 nm are not considered here, as the nanogrid contact would be outside of the perovskite in the 3-T tandem depends on the depth of the nanogrid contacts inside the perovskite, controlled by the insulator (Al_2O_3) thickness. The efficiency values presented here are based on an optimal insulator thickness of 100 nm; as a general rule,

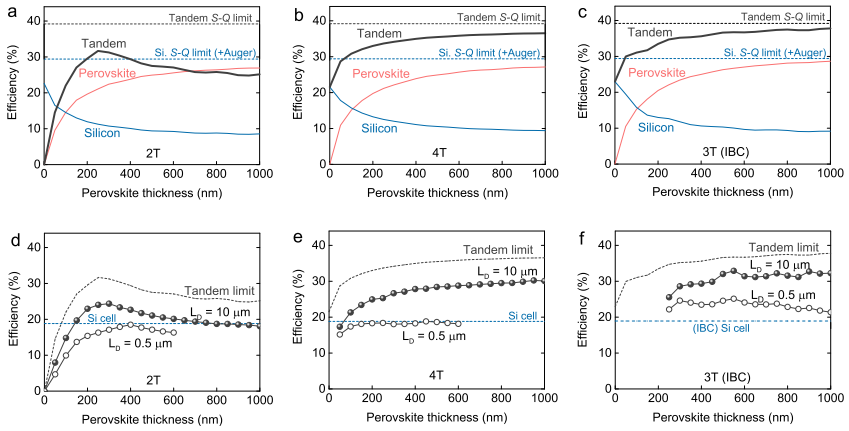

Figure 5.3: Limiting and realistic performance. Limiting tandem power conversion efficiency as a function of perovskite thickness on (**a**) 2-terminal, (**b**) 4-terminal, and (**c**) 3-terminal (IBC). The limiting efficiency is modeled by assuming infinite minority carrier diffusion length in perovskite and silicon cells; benchmarked with their respectively calculated S-Q limit (39.2 %; 1.55 eV perovskite with 1.12 eV Si bandgaps), and single junction Si limit (29.4 %; corrected for Auger recombination). The contribution of the Si and perovskite materials to the tandem efficiency are indicated. Similarly, in the realistic case on (**d**) 2-terminal, (**e**) 4-terminal, and (**f**) 3-terminal (IBC), by assuming finite minority carrier diffusion length in perovskite (L_D) and Si, benchmarked with simulated planar single junction standard front-rear contacted and interdigitated back-contact (IBC) Si cell efficiency. At L_D = 0.5 μm, the data points are missing in panels **d**, **e** because the perovskite cells are too resisitve to simulate (as the thickness increases) in contrast to panel **f**. Some data, however, are limited (below 250 nm perovskite thickness) in panel **f**, because of a thickness restriction by the embedded nanogrid contacts. In panel **f**, the realistic tandem efficiency is plotted at global optimum pitch sizes: 5.125 μm (for L_D = 10 μm), and 1.6 μm (for L_D = 0.5 μm). All PV parameters (J_{sc}, V_{oc}, and FF) are tabulated in **Figure 5.9** (Supporting information).

the nanogrid contact should be embedded around <40 % of the perovskite thickness (Supporting information). The global maximum 3-T (IBC) tandem efficiencies for the 0.5 and 10 μm diffusion lengths are 25.1 % (at 550 nm thick with 1.6 μm pitch), and 32.9 % (at 550 nm thick with 5.125 μm pitch), respectively.

To date, the world record efficiency of single junction Si photovoltaics is 26.3 %. These cells use nonplanar front-side texturing with antireflection coatings. Unless a very high quality perovskite is used (greater than ~2 μm minority carrier diffusion length), a planar perovskite-silicon tandem using a standard 2-T or 4-T configuration will not exceed the ~26.3 % textured single junction Si efficiency. We demonstrate that the 3-T (IBC) can overcome the limitation even using lower quality perovskite (e.g., with ~0.8 μm minority carrier diffusion length). In terms of the efficiencies of the individual layers, this difference means that a > 21.7 % equivalent single junction perovskite cell is needed to bring a 18.8 % planar Si cell above 26.3 % in a 2-T or 4-T configuration, whereas only a > 18.8 % equivalent single perovskite cell is needed using our 3-T (IBC) configuration.

5.5 The roles and limitations of nanowire grid contacts

To elucidate the performance improvements of the 3-T (IBC) tandem design relative to the standard 2-T and 4-T tandem configurations, we investigate the influence of parasitic absorption and reflection, absorption path length enhancements, and nanophotonic effects from the nanowire grid.

We begin by first identifying losses from the device spectral response curves, shown in **Figure 5.4a**. The external quantum efficiency (EQE) spectra of the tandems are simulated in their highest steady-state performance configurations (24.8 %, 30.2 %, and 31.2 %, for 2-T, 4-T, and 3-T, respectively), corresponding to the 10 μm diffusion length. Note that the 31.2 % efficiency corresponds to 1 μm pitch size to demonstrate more clearly the nanophotonic cavity effects in the 3-T (IBC) configuration but an optimized 3-T configuration gives 32.9 % efficiency.

The 3-T configuration shows improved EQE most significantly in the wavelength range below 500 nm and to a lesser degree above 500 nm. We attribute the short wavelength improvements to the use of nanowire grid contacts embedded inside the perovskite. The free front surface allows blue photons, typically parasitically absorbed by the TCOs present at the front of the 2-T and 4-T geometries, to be absorbed instead in the perovskite and collected in the 3-T (IBC) tandem. Although the 4-T has three TCO layers, its performance surpasses that of the 2-T design near the perovskite band edge, due to difference in the optimized perovskite layer thickness (950 and 300 nm for 4-T and 2-T, respectively). The near band-edge EQE (~780 nm; 1.58 eV) for 3-T (IBC) is higher than that of the 4-T, even with a thinner perovskite layer (550 and 950 nm, respectively). This can be explained by a higher charge generation rate from ~700 to 800 nm due to a cavity effect provided by the nanowire grid (Supporting information).

The EQEs for the Si bottom cells in 2-T and 3-T designs show similar behavior, suggesting that the top and bottom cells in the 2-T and 3-T tandems share a similar optical-coupling mechanism. However, the EQE for the Si cell in the 2-T is lower than that in 3-T tandem, partly due to near-IR parasitic absorption of the top TCO in the 2-T (Supporting information) in addition to a shorter optical path length enhancement (the optical interaction length normalized to the absorber thickness) in the 2-T Si cells (**Figure 5.4b**). The presence of the nanowire grid increases the optical path length enhancement inside the Si cell at longer wavelengths (~900 to 1100 nm) due to two features: first, scattering from the nanowire grid changes the angular distribution of light (a maximum at 1100 nm wavelength with 15°) effective angle (see details in Supporting information) thereby increasing the interaction length. Second, this scattering additionally improves the light trapping inside the device, further improving the effective optical path length in the silicon.

Having examined the influences responsible for modification of the total optical generation in the three configurations, to further understand the efficiency improvements we examine the electrical contributions by comparing the drift-diffusion transport in our 3-T (IBC) with the 4-T tandem, as both configurations similarly share electrically

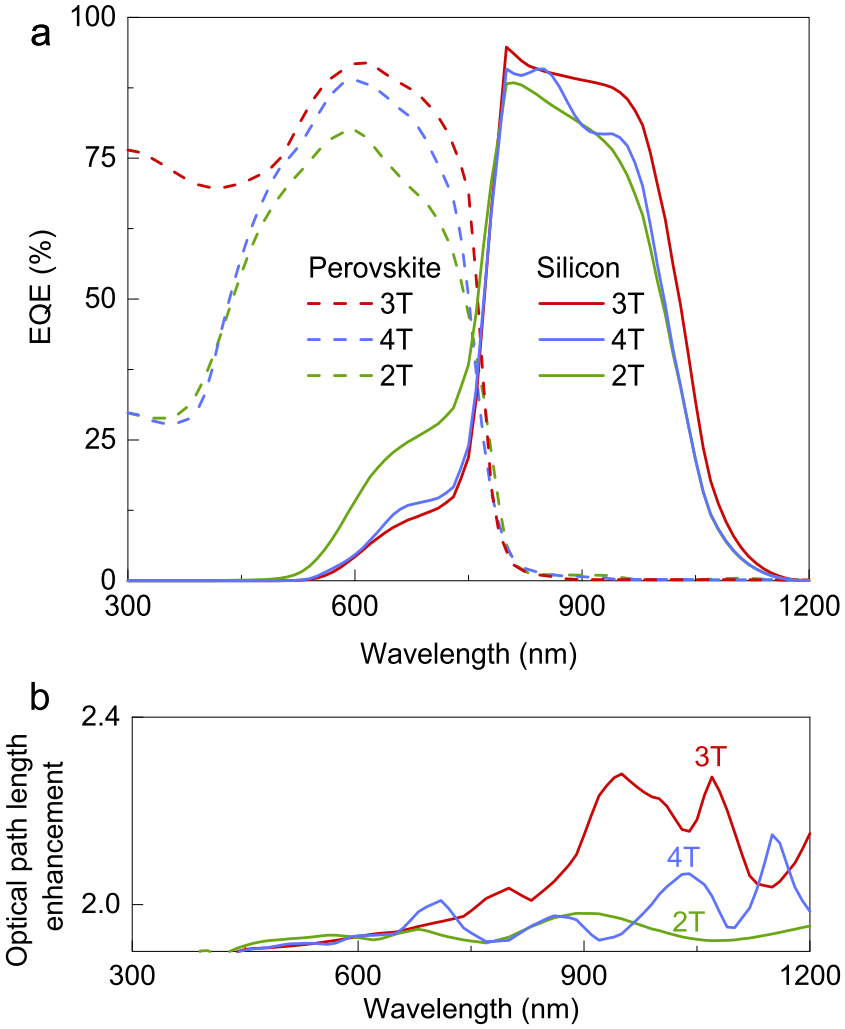

Figure 5.4: Coupled optical-electrical spectra response. (**a**) Simulated EQE of perovskite (dashed lines) and silicon (solid lines) cells for 2-T, 4-T, and 3-T (IBC) configuration at their optimum performances according to the **Figure 5.3** (at perovskite thickness of 300, 950, and 550 nm for 2-T, 4-T, and 3-T (IBC), respectively with perovskite minority carrier diffusion length of 10 μm). (**b**) Optical path length enhancement showing significant enhancement in the 3-T (IBC) at long wavelength range that is beneficial for the bottom Si cell.

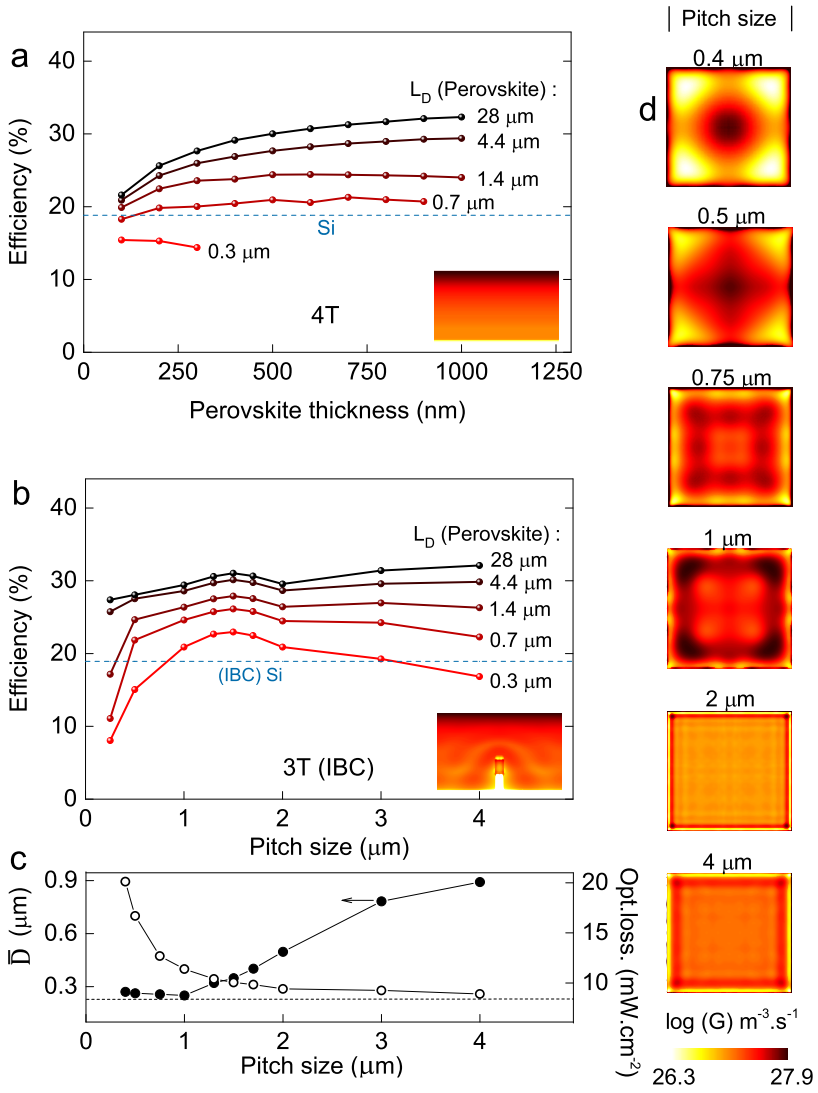

Figure 5.5: Transport and charge collection using the embedded nanoscale back contacts. (**a**) Tandem power conversion efficiency of the 4-T as a function of perovskite thickness; the omitted data points are due to a high (transport) resistance as the perovskite thickness increases. (**b**) Tandem power conversion efficiencyof the 3-T (IBC) as a function of pitch size of the nanogrid; carried out at 500 nm perovskite thickness. The insets in (**a**, **b**) show cross-sectional charge generation rates that are distinct between 4-T and 3-T (IBC). The tandem performance is examined using different qualitiy perovskites based on their minority carrier diffusion length values (L_D). (**c**) Calculated effective collection distance ($\overline{D}$) and total optical losses (reflection and parasitic absorption) as a function of pitch size. (**d**) Top view of charge generation rate in 3-T (IBC) showing most of charges are concentrated toward the contact (edges of the squares) as the pitch size increases (the values indicate different pitch sizes); the generation rate values are averaged over the perovskite thickness inside the cavity.

decoupled schemes. In the 4-T, the tandem efficiency increases with the perovskite thickness and diffusion length (**Figure 5.5a**). The tandem efficiency starts to decrease as the perovskite thickness approaches its minority carrier diffusion length due to the trade-off between the distance charges have to travel (before nonraditative recombination) and the amount of absorbed photons in the perovskite, which in the 4-T configuration is simply governed by Beer-Lambert exponential decay (see the charge generation rate decaying profile in the inset **Figure 5.5a**).

The drift-diffusion transport in the 3-T (IBC) is more complex, as the charges have to travel simultaneously in vertical and lateral directions. Similar to the influence of perovskite thickness, there is a trade-off between increased reflection at small pitches and increased transit distances at large pitches. The incorporation of the nanowire grid network, however, provides optical resonances near the metal nanowire contact that enhance the charge generation rate at the depth of the nanowire grid (inset in **Figure 5.5b**), while also modifying the lateral generation rate. Using a 500 nm thick perovskite layer, we study the tandem efficiency as a function of the nanowire grid pitch (**Figure 5.5b**). We observed a drop in tandem efficiency of the 3-T when the pitch is below 1 μm due to increased reflection and thus lower transmission of light into the Si bottom cell. A reduced reflection and higher transmission into the Si bottom cells results in an increase in the tandem efficiency when the pitch size is above 2 μm. This simple trend does not hold for a pitch size from 1 to 2 μm, where the tandem efficiency is slightly reduced. We correlate this with cavity resonance effects of the pitch on lateral generation profiles of the 3-T (IBC).

To further understand the cavity effect of the pitch on the lateral generation, we calculate the mean distance to collection ($\overline{\mathrm{D}}$) by integrating the shortest distance to the further of the two contacts at all points in the absorber volume, weighted by the total generation rate at that location (Supporting information). The length $\overline{\mathrm{D}}$ thus represents the average distance generated charges have to travel before being collected (**Figure 5.5c**); configurations with a shorter $\overline{\mathrm{D}}$ will show higher total collection, particularly for materials with lower diffusion lengths. Remarkably, $\overline{\mathrm{D}}$ actually becomes smaller as the pitch increases from 400 nm up to 1000 nm. This indicates that by utilizing photonic cavity effects, we can double the distance between the contacts while reducing the average distance a charge carrier must traverse to be collected. To visualize this photonic cavity effect, we plot the charge-generation rate integrated over the perovskite thickness as a function of lateral position (**Figure 5.5d**). For smaller nanowire grid pitches (400 - 500 nm), the charge generation rate is highest far from the nanowire contact grid, whereas for larger grid pitches (>750 nm), charge generation is increasingly localized near the metal contact. This not only allows us to break from the trade-off between increasing collection probability and increasing absorber material but also partially explains the observed improvement in the 3-T perovskite EQE in the moderate wavelength region for perovskites (500 nm > λ > 780 nm, where TCO absorption is small), relative to the 4-T design. While we examine gold here, this effect holds for other common contact metals (Ag, Al) as well (**Figure 5.15**).

5.6 Conclusion and outlook

Herein we have demonstrated the potential of a nanoscale back contact embedded in a thin film solar cell to improve tandem efficiency and relax requirements on the thin film diffusion length. We investigate a perovskite-silicon tandem to build a double back contact tandem design in a three-terminal configuration. On the basis of coupled optical and electronic simulations, we show that our design has the potential to overcome the limits of the traditional two- and four-terminal tandem configurations, in particular reducing the constraints on perovskite quality. Using even moderate-quality perovskite materials with minority carrier diffusion lengths of 0.8 μ, the 3-T IBC shows tandem power conversion efficiency surpassing the single junction silicon efficiency record of 26.3 %, when used with an 18 % efficiency planar silicon cell. Comparatively, achieving this performance in a 4-T tandem design requires at least a 2 μm diffusion length in the perovskite. Perhaps more dramatically with the same 18 % silicon base cell, the 3-T IBC design can reach 32.9 % tandem efficiency with an optimistic 10 μm diffusion length perovskite material. Using the same perovskite quality the 4-T and 2-T configurations only reach 30.2 % and 24.8 %, respectively. Furthermore, in order to surpass the single junction Shockley-Queisser efficiency limit (~33 %), our design halves the requirement on the perovskite carrier diffusion length from 24 μm for a 4-T tandem to 12 μm for our nanostructured 3-T design. The improved performance of our 3-T configuration is attributable to the significant reduction of parasitic absorption/reflection and enhanced charge generation near the embedded nanowire grid contacts, reducing the necessary carrier diffusion distances.

We also confirm the same efficiency benefits of the 3-T configuration apply when using a 25 % efficient textured IBC silicon bottom cell, where the 3-T tandem efficiency can reach 35.2 % efficiency compared to only 32.8 % for the 4-T configuration (**Figure 5.14**). Additionally, the higher absolute efficiency (32.9 %) of the planar 3-T design relative to the 4-T textured configuration indicates the potential to reach high tandem efficiencies while using planar thin film devices. This suggests further benefits are attainable with the recent "electrically flat, optically textured" Si device configurations that improve light trapping using dielectric scattering patterns but still allow for the low surface recombination losses of planar cells [43, 44].

Finally, because our current design is fully based on planar tandem structures, further improvements can be readily made by optimizing the front surface of the 3-T IBC, which is left free for light-trapping, surface passivation, antireflective coating, directional emission or enhanced photoluminescence out-coupling. The presence of nanowire grid contacts in the 3-T IBC design should allow one to fabricate devices monolithically without the need for current matching present in the 2-T tandem and is also compatible with the 26.3 % record efficiency interdigitated back contact (IBC) silicon cells.

5.7 Supporting information

5.7.1 Optical modelling

Acquiring optical constants

We acquired complex optical constants (*n-k*) of the materials from a combination of spectroscopic ellipsometry (SE) measurements and literature values. All *n-k* values used in our simulation are plotted in **Figure 5.6**. For the TiO_2, NiO_x, Al_2O_3, and fused SiO_2, the *n-k* values are based on SE measurements, whereas the *n-k* values for the FTO, $CH_3NH_3PbI_3$, and Si are taken from the literature. The TiO_2 and Al_2O_3 films were grown using atomic layer deposition (ALD) at 250°C, while NiO_x film was deposited by a plasma-enhanced ALD. The films were further thermally annealed up to 480°C (for TiO_2 and Al_2O_3), and 300°C (for NiO_x) in ambient air for 60 minutes. This post-annealing treatment enhances the metal oxide crystallinity which is important to get a high efficiency device. For example, the TiO_2 was converted from a resistive semi-amorphous phase to anatase crystalline films, with enhanced *n* values from ~1.7 to ~2.2 after the post-annealing. Using ALD, we could get a conformal, compact, and smooth films compared to the typical solution based process (e.g. sol-gel, chemical bath deposition, spray-coating) which minimizes surface roughness, simplifying our SE model.

We used the *n-k* values for $CH_3NH_3PbI_3$ reported by Löper [45], which have an extremely sharp onset and small Urbach energy [46] (comparable to GaAs), and thus exclude any traces from an indirect bandgap contribution of $CH_3NH_3PbI_3$. For c-Si, FTO (Pelkington TEC 15), a-Si:H (i), and SiN_x the *n-k* values were taken from reported data by Green [47], Ball [48], Pierce [49], and Baker-Finch [50], respectively. For the metals in the nanogrid (Au), and rear-contact (Ag), we used the *n-k* values from Palik [51], and Johnson & Christy [52], respectively. The optical constant for $n^{++}Si$ (front floating emitter, and rear-emitter), and $p^{++}Si$ (back surface field) are set to be identical with standard c-Si. However, their free carrier absorption effects are fully

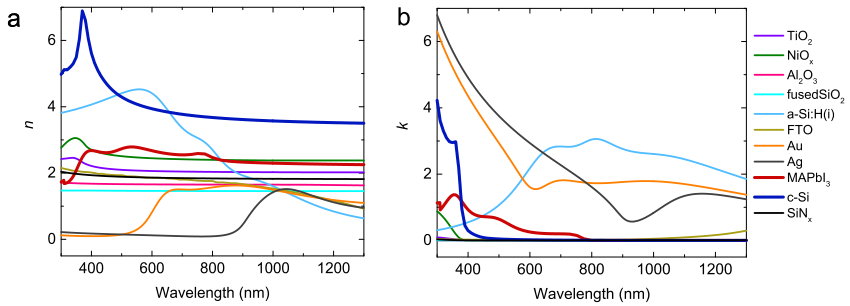

Figure 5.6: Refractive index of all materials used for the simulations: (**a**) the real part (*n*), and (**b**) the imaginary part (*k*). The *n-k* for a-Si:H (i), FTO, Au, Ag, $MAPbI_3$, c-Si, and SiN_x are reported values from the literatures [47–52], while values for TiO_2, NiO_x, Al_2O_3, and fused-SiO_2 are obtained from ellipsometry measurements.

taken into account in our electrical simulations, as well as our optical path length calculations (details discussed below).

Optical simulation setup

Interface and data processing. The optical simulations were performed in two different modules using (1) full-field electromagnetic wave calculations based on a finite-difference time-domain method (FDTD, Lumerical, Inc [38]) for the perovskite cell, and (2) a rigorous polarization ray tracing solver (OPAL2, PV Lighthouse Pty. Ltd [53]) for the Si cell. The two different methods are implemented due to the thickness difference between the two cells (< 1 μm for perovskite *vs*. 180 μm for Si). As a consequence, light propagations in both cells are computed differently (coherent *vs*. incoherent for perovskite *vs* Si cells, respectively). The two methods are coupled by using output from the FDTD (optical transmission modes weighted over AM 1.5 spectrum) as an input/filter for the ray tracing solver.

To get an accurate result of all optical interferences between the top and bottom cell interfaces, we extend the simulation ~1 μm down to the Si for the 2-T and 3-T (IBC) tandems. This is important, because the perovskite and silicon cells in both cases are optically coupled. However, for the 4-T tandem, the two cells are optically decoupled, but we still included an interference contribution from the SiO_2 spacer (framed down to ~1 μm out of 10 μm from its actual thickness). A weighted transmission modes from this SiO_2 spacer (~ 10 % of the thickness) is used as the input for the ray tracing calculation in the 4-T tandem, and in this case SiO_2 spacer is used as a superstrate.

Besides the original packages provided by the FDTD and ray tracer modules, we carried out our computational routines using Python codes to couple results from those two packages. The routine includes calculations of charge generation rate inside cavities, effective collection distance, optical path length enhancement, total reflectance, and sweeping PV parameters.

Perovskite solar cell. One unit cell is defined as a square with side lengths of the nanowire grid spacing, centered at the grid intersection. We use anti-symmetric boundary conditions for the *x*-axis, symmetric boundary conditions for *y*-axis, and

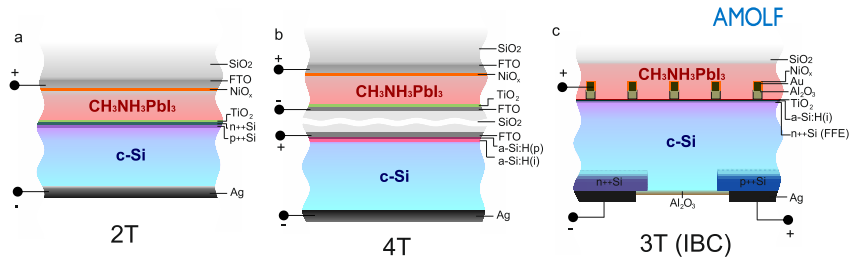

Figure 5.7: Schematic (cross-section view) of planar perovskite-silicon tandem architectures used in this work. (**a**) 2-T, (**b**) 4-T, and (**c**) 3-T (IBC). The schematics are drawn not to scale.

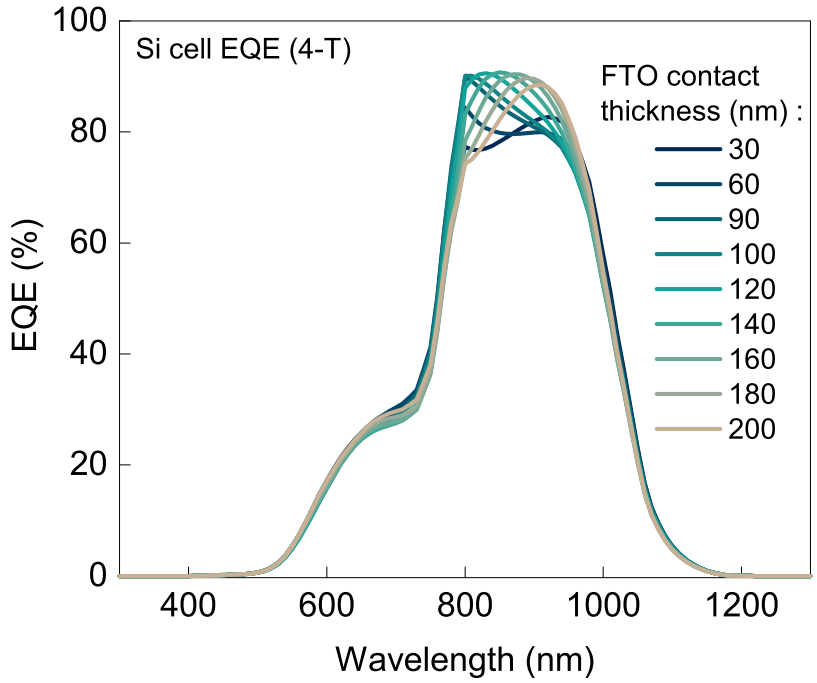

Figure 5.8: Silicon cell EQE in the 4-T with different FTO thickness. It shows the FTO contacts can act as anti-reflective coating on the Si cell in the 4-T.

perfectly matched layers (MPLs) for z-axis, allowing us to simulate a quarter of the unit cell area. A broadband plane wave (λ = 300 - 1300 nm; 1 nm interval) at normal incident (propagating toward the structure along the z-axis) is launced from the top of the structure as incident source, with polarization either from x- or y-axis. The simulation employs a cubic mesh with a mesh size of 5 nm, and to obtain a sub-accuracy, a 1 nm refinement is employed along the grid-perovskite and TiO_2 perovskite interfaces. Prior to running the simulation, all of the optical constants are imported into the materials database, and modelled by multi-coefficient fitting (λ = 300 - 1300 nm) until reaching a global minimum RMS error. For the perovskite, the multi-coefficient fitting provided by the FDTD gives a slightly larger error after 900 nm wavelength which deviates the k-optical constant to be above zero which physically does not exist. So, we manually set the k values to be 0 above 900 nm.

A frequency profile monitor is used to detect the electric field across the structures. Transmission is monitored with power monitor placed below the structure (TiO_2/a-Si:H(i) interfaces for 3-T, NiO_x/a-Si:H(i) interfaces for 2-T, and rear-FTO (perovskite)/glass (spacer) interface for 4-T); see schematic tandem structure (**Figure 5.7**). Absorption is computed by calculating a ratio of power absorption from each electric field vector component integrated over the volume of the material. An optical charge generation rate (G) can be computed spatially over the $CH_3NH_3PbI_3$ structures by multiplying the electric field intensity ($|E|^2$), and imaginary part of permittivity (ϵ") of the $CH_3NH_3PbI_3$ over twice angular frequency Plank constant ($2\hbar$); G(ω) =

$[\epsilon"|E|^2]/2\hbar$.

Reflection is monitored with power monitored placed on top of the structure and behind the source. Note that, this is just a reflection mainly contributed by the perovskite cells structures only, and partially (but not fully) by the Si cells (since we also incorporated interference ~1 μm down to the Si cells). Reflections from the Si back interface are incorporated in the following section.

Silicon solar cell. For the Si bottom cell, the source of illumination is computed by weighting the optical transmission through the top perovskite cell with AM 1.5 solar spectrum at normal incidence. In addition to this, for 4-T tandem, the fused SiO_2 spacer (10 μm), and FTO (Si top contact) are incorporated by calculating the transfer matrix from the perovskite to the FTO and Si cell. This FTO acts as an anti-reflective coating (**Figure 5.8**) for the Si bottom cells in the 4-T, and later on explains why the EQE of Si cell is higher in the 4-T compared to the 2-T; given the fact that perovskite thickness used in the 4-T (950 nm thick) is thicker than the 2-T (300 nm thick) at their optimum efficiency. We calculated the reflection, transmission, and absorption of the (planar) Si cell by taking into account an opticla path length enhancement (Z) dependent over the broadband range (λ = 300 - 1300 nm).

The optical path length enhancement inside the Si cell mainly occurs because of non-negligible specular reflection both from the rear Ag metal contact and scattering from the nanoscale metal grid contact within the perovskite (increasing the average angle of incident light on the silicon interface). These effects cause the optical path length to be greater than the actual Si cell thickness; where Z is defined as the ratio of the optical thickness and actual thickness ($Z = t_{opt}/t$). Using our computational routine, we solved the $Z(\lambda)$ analytically for each tandem configuration by taking into account the reflectance (in both sides) based on the actual structures obtained from FDTD simulations. Free-carrier absorption losses from the front-floating emitter (FFE), back-surface field (BSF), and rear-emitter (detail characteristics described in the electrical modelling part) were also incorporated into the $Z(\lambda)$ calculation.

The generation rate ($G(\lambda)$) for Si cell can be directly calculated as a Beer-Lambert decay of the optical transmission modes ($T(\lambda)$) multiplied by the absorption coefficient ($\alpha(\lambda)$) over the Si optical thickness: $G(\lambda) = \alpha(\lambda).T(\lambda).\exp[-\alpha(\lambda).z(\lambda).t]$. The total generation rate (G) is calculated by accumulating the $G(\lambda)$ over the simulated wavelength range λ = 300 - 1300 nm.

For the limiting case (heretofore is essentially the actual optical limit taking into account all of the optical interference), we used PV parameters calculated based on our optical simulation: (1) the optical short-circuit current (J_{opt}) is directly calculated by multiplying the total generation rate (G) with elementary charge constant (q) by assuming 100 % collection efficiency and infinitely long diffusion length; (2) the optical open-circuit voltage (V_{opt}) is calculated based on the standard diode equation using ideality factor (n) of 1, and 2 for perovskite, and silicon cells, respectively. For perovskite cell, there are some variants of the diode ideality factor reported in literatures depending on the materials quality and device architectures. In this optical simulation, the n = 1 is used to emphasize that the main recombination is purely through radiative

recombination; (3) the optical fill-factor (FF_{opt}) is determined according to a well-known empirical equation [54]. All PV parameters obtained in this optical simulations are tabulated and compared together with the coupled optical-electrical ones in **Figure 5.9**.

Optical path length enhancement for planar Si cells. The optical path length enhancement is defined as a ratio between the optical thickness and the actual thickness of the Si cells. The optical thickness becomes more than the actual Si thickness when the photon experiences multiple reflections from the front and rear surfaces of the Si cells. Although our tandem configurations are planar without any use of texturing/light trapping schemes, the enhancement is still significant, in particular for 3-T (IBC) tandem case where we have nanogrid network (containing Au metal), and metal rear contact (Ag back reflectior) on top and bottom of the Si cells, respectively, thus resulting multiple internal reflections inside the Si cells. The influence of the nanowire mesh is incorporated through the calculations of the electric field immidiately after propagation into the silicon layer, which are then transformed to the far-field, providing the angluar distribution of the incident irradiation. From the angular distribution, an effective angle, φ, for the light entering the silicon later is computed, and the path length is then adjusted by $Z(\lambda)_{scat} = 1/\cos(\varphi)$. We formulate the optical path length enhancement for each wavelength $Z(\lambda)$ as:

$$\begin{aligned} \mathrm{Z}(\lambda) =& \mathrm{Z}(\lambda)_{scat} . \sum_{i=1}^{\infty} \left[I_0(\lambda) + \left[I_{i-1}^{D}(\lambda) \left(R(\lambda)_{Ag} \right) - L(\lambda)_{BSF} - L(\lambda)_{Emit} \right] \right. \\ & \left. + \left[I_{i-1}^{U}(\lambda) . (R(\lambda)_{Grid}) - L(\lambda)_{FFE} \right] \right]. \end{aligned} \tag{5.1}$$

where $\mathrm{Z}(\lambda)_{scat}$ is effective path length enhancement due to scattering from the nanogrid network towards Si cells, $I_0(\lambda)$ is coming photon towards Si cells (or transmission from the top cells), $I_{i-1}^{D}(\lambda)$ is incoming photon facing *down* toward the rear of Si surfaces, $I_{i-1}^{U}(\lambda)$ is incoming photon facing *up* toward the front of Si surfaces, $R(\lambda)_{Ag}$ is the reflection from the silver surfaces toward Si, $R(\lambda)_{Emit}$ is losses from the rear-emitter, $L(\lambda)_{FFE}$ is losses from the front-floating emitter. These losses are due to free-carrier absorption from the highly and heavily doped Si, and modelled using classical Drude's model absorption [55]. The iteration is repeated until either $I_{i-1}^{D}(\lambda)$ or $I_{i-1}^{U}(\lambda)$ is $<$ 0.0001.

Total reflection losses fro the 3-T (IBC) tandem. Simulating total reflection (**Figure 5.10**) in the 3-T (IBC) is not as straight forward as in the 2-T and 4-T tandem configurations, because we need to take into account the effect of optical path length enhancement from the Si cell that intuitively should reduce the reflectance obtained from FDTD. However, we can formulate the upper bound of the total reflection $\mathrm{R}_{tot}(\lambda)$ as:

$$R_{tot}(\lambda) = R_{top}(\lambda) + R_{bottom}(\lambda) \tag{5.2}$$

$$R_{bottom}(\lambda) = T_1(\lambda).[1 - A_{Si}(\lambda)].T_2(\lambda) \tag{5.3}$$

$$A_{Si}(\lambda) = \left(1 - e^{-\alpha(\lambda).Z(\lambda).t}\right).T_1(\lambda) \tag{5.4}$$

where $R_{top}(\lambda)$ is the reflection contributed by the perovskite top cell (with all grid lines involved), $\alpha(\lambda)$ is the absorption coefficient of the Si, $Z(\lambda)$ is the optical path length enhancement (calculated from the **equation 5.1**), t is the Si thickness (180 μm), $T_1(\lambda)$ is transmission from the perovskite to the Si cell, and $T_2(\lambda)$ is transmission from Si back into the perovskite. $R_{bottom}(\lambda)$ is reflection contributed by the Si cell, calculated from the transmission ($T_1(\lambda)$ and $T_2(\lambda)$) and attenuated by the losses from the Si cell absorption ($A_{Si}(\lambda)$). The total reflectance loss in the 3-T (IBC) is 12.4 mW/cm^2, which is less than the 2-T, and 4-T configurations (13.7 mW/cm^2 and 12.9 mW/cm^2 for 2-T and 4-T, respectively). The reflectance loss in the 4-T is quite similar to the 3-T (IBC), due to optimized FTO layer, which serves as anti-reflective coating for Si bottom cell (**Figure 5.8**).

5.7.2 Electrical modelling

Determining the electrical properties

All electrical parameters are listed in **Table 5.1**. These values were modelled based on values reported in literature. For the perovskite ($CH_3NH_3PbI_3$), we assume that the charge transport is equal for electron and holes, although asymmetric transport is possible (e.g. by chloride addition into the iodide mixture; $CH_3NH_3PbI_{3-x}Cl_x$) [63]. We assume that the dominant recombination pathways are trap-assisted (Shockley-Read-Hall) and electron-hole radiative recombination, whereas Auger recombination process is assumed to be less competitive in our simulation (which is valid at the steady-state 1 sun illumination) [56]. The electron (TiO_2), hole (NiO_x) transporting layers, and the dielectric insulator (Al_2O_3) are modelled as semiconductors with doping profiles simulated using a selective junction model (Helmholtz Zentrum, AFORS-HET) [57]. The profile basically depends on the density-of-states (DOS) of materials set in the simulation inputs.

For Si cells, parameters of electron (and hole) mobility, lifetime, dark-current, sheet, and base resistances are modelled based on doping concentration (computed using calculator provided by PV lighthouse); doping profile is simulated using classical Drude model. Auger recombination is included in our calculations for both planar and textured Si cells. The effect becomes higher in the textured cells because of higher excess carrier concentration. For example, on the front surface of Si the Auger recombination rate is $\sim 10^{32}$ cm$^{-3}S^{-1}$ for the textured device, and $\sim 10^{26}$ cm$^{-3}S^{-1}$ for the planar Si cell.

Table 5.1: Materials properties used for the electrical simulation.

Material	E_g †	m_h* ‡	m_e* ‡	ϵ_{DC} ♭	χ §	μ_h ⋆	μ_h ⋆	τ_n #	τ_p #	R_S *	J_0 ⊥
$CH_3NH_3PbI_3$	1.55	0.104	0.104	6.5	3.9	30	30	$< 10^4$	$< 10^4$	-	1.7 x 10^{-20}
TiO_2	3.2	-	-	9	3.92	0.2	0.1	5	1	-	-
NiO_x	3.25	-	-	11.9	1.46	0.1	0.2	1	5	-	-
Al_2O_3	6.7	-	-	9.34	4.02	0.1	0.1	1	1	-	-
Au grid	-	-	-	37	5.1	-	-	-	-	0.85 - 13	-
FTO	3.5	-	-	9.0	4.1	-	-	-	-	6	-
a-Si:H (i)	1.8	0.34	0.34	7.2	3.95	20	5	0.32	1.28	-	-
n^{++}Si FFE	1.09	1.18	0.809	11.7	4.62	150	150	6 x 10^4	6 x 10^4	70	6 x 10^{-11}
(p-type) c-Si	1.12	1.18	0.809	11.7	4.59	470	1471	3 x 10^6	4 x 10^6	1000	3 x 10^{-7}
n^{++}Si (emitter contact)	1.09	1.18	0.809	11.7	4.62	150	-	6 x 10^4	-	55	3 x 10^{-7}
p^{++}Si (BSF contact)	1.09	1.18	0.809	11.7	4.62	-	150	-	6 x 10^4	40	1.5 x 10^{-7}

† Effective electronic bandgap at 300 K that is modelled using Varshni's coefficient. For Si, doping dependent is also modelled that account for narrowing the bandgap.

‡ Effective mass which is used to calculate the density of states (DOS). at valence and conduction band using the Fermi-Diract statistics.

♭ Relative dielectric constant (relative permittivity) at zero frequency (DC).

§ Work-function (*vs.* vacuum level).

⋆ Charge mobility.

Charge lifetime where the values are varied (with fixed mobility) to obtain different values of minority carrier diffusion length (L_D); where $L_D = [(k_bT/q).\mu.\tau]^{1/2}$. For c-Si, the Auger recombination model was also taken into account.

* Sheet resistance; we also incorporated a shunt resistance (R_{SH}) in the external circuit to be 10^5 Ω/cm^2. For the Au, the sheet resistance is calculated based on equivalent resistivity ranging across the different pitch sizes. For Si cell, to optimize the FFE performance, the base resistance of the c-Si should be higher than the n^{++}Si

⊥ Dark-saturation current density where the ideality factors are 1 and 2 for perovskite and Si cells, respectively.

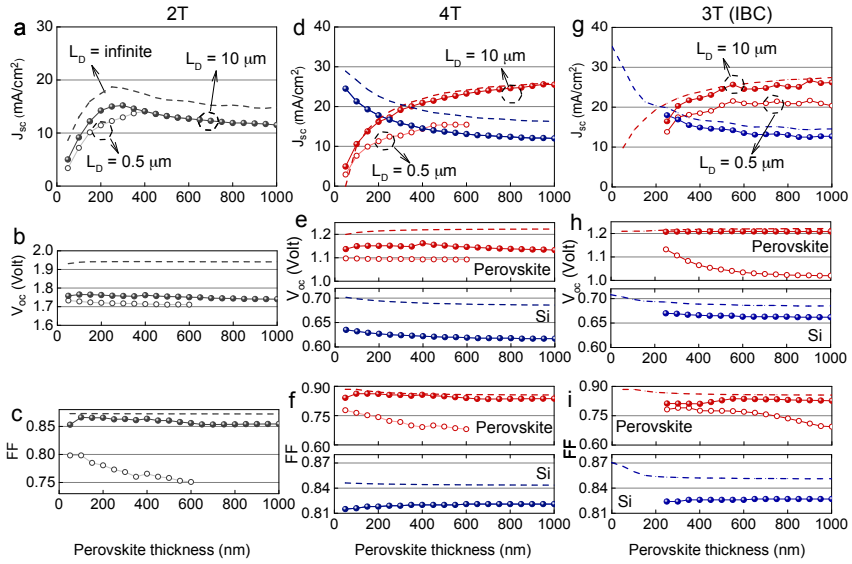

Figure 5.9: PV parameters of the perovskite-silicon tandem obtained from the optoelectronics simulations. The performance is examined using two different qualities of perovskite minority carrier diffusion lengths (indicated as L_D = 0.5 μm and 10 μm). For the 2-T configuration, the current-matching condition (series connection) is applied with 100 % tunneling efficiency from top to bottom cells, and so only the tandem performances is plotted here (**a**-**c**). For the 4-T, the top-bottom cells are operated independently where contribution from perovskite (red lines) and silicon (blue lines) cells are shown (**d**-**f**). In the 4-T with the 0.5 μm diffusion length, perovskite cells with a thickness above 600 nm are not simulated due to limited charge collection. For 3-T (IBC) configuration, the two cells are treated to be electrically decoupled with 100 % tunneling efficiency from top to the bottom cell where the respective two cell performances are presented (**g**-**i**). In the 3-T (IBC), cells with perovskite thickness less than 250 nm were not simulated due to thickness restriction of the internal nanowire grid network. All of these optoelectronics PV parameters (solid lines) are compared with the PV parameters obtained purely from the optical simulation (curves with dashed lines); indicating the limiting performances. The tandem efficiencies for the 2-T, 4-T, and 3-T (IBC) are presented in **Figure 5.3**.

Electrical simulation setup

Interface and data processing. The electrical simulation was performed by numerically solving the electrostatic potential and drift-diffusion transport equations under finite-element based method using two different simulation modules (1) DEVICE CT (Lumerical, Inc [40]) for perovskite cells, and (2) Quokka2 (PV Lighthouse, Pty, Ltd [41]) for Si cells. The treatments were due to the large different thickness in the two cells (< 1 μm for perovskite *vs*. 180 μm for Si). We used spatial charge carrier distributions (generated from the optical simulation above) as inputs for our electrical simulations. While complex behaviour of the CH_3NH_3 ions has been shown to create hysteresis in current-voltage response curves of perovskite materials, most high efficiency perovskites actually do not pose such behaviour [58], and so this

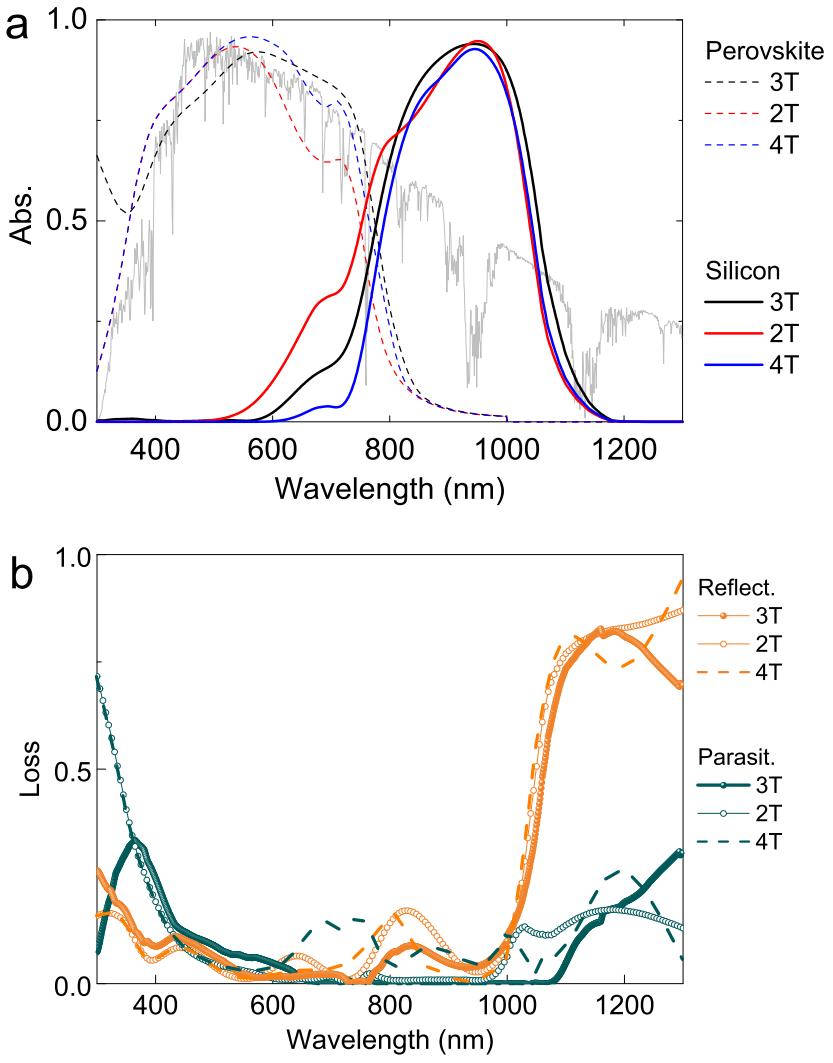

Figure 5.10: Spectra response of the perovskite-silicon devices with 2-T, 4-T, and 3-T (IBC) tandem configurations. (**a**) Absorption (compared with AM 1.5 standard spectrum; grey line), and (**b**) Losses (reflection and parasitic absorption). These spectra responses were simulated at optimum conditions for each tandem configuration (at perovskite thickness of 300 nm, 950 nm, and 550 nm for 2-T, 4-T, and 3-T (IBC), respectively). Note that the parasitic absorption of both 2-T and 4-T tandem increases up to ~0.74 at 300 nm wavelength.

influence is neglected here. For the Si cells, we also consider optical path length enhancement in the charge generation rate calculation (see the Si cells discussion below). Note that both modules themselves currently are not able to model a tunnel junction, because the provided tunnel model is based on a quantum-mechanical process (band-to-band tunneling models of Hurkx-Schenk [59]). So, we computed analytically the electrical transmission from the top to the bottom cells by adopting Ebers-Moll model of bipolar transistor with a unity gain (the non-unity gain is also examined, see **Figure 5.11**). We used identical geometrical tandem devices as described in the optical simulation. All simulations are conducted at a temperature of 300 K.

Perovskite solar cells. We applied a tetrahedron 3D coarse mesh (with 20 nm length constraints), and auto mesh refinement across a change in doping density (typically ~10 times smaller than the geometrical sizes). A boundary condition controlling the bias is set on both Au metal nanowire grid (emitter) and n^{++}Si (base) where a steady-state DC sweep is run from -0.2 to 1.6 applied voltage (0.02 V interval). We used Gummel's numerical method for a self-consistent control for the calculation, iterating between calculating the drift-diffusion equation and used it as an input to solve Poisson's (electrostatic equation) equation, *vice versa*. This iteration was carried out until absolute tolerance < 10^{-6} V to reach the convergence. We used the output containing the spatial information of the electrostatic potential, the electron-hole distribution, recombination rates, and mobility in order to compute the perovskite PV characteristics (*J*, *V*, *FF*), and *EQE* (in this case using multistep single frequency generation rate rather than broadband plane wave input on the FDTD optical simulation). All PV parameters for perovskite cells can be seen in the **Figure 5.9**; all of which are in a good agreement with experimental values of high efficiency perovskite solar cells.

Silicon solar cells. For the silicon cells, we used 1D charge generation rate profiles as the inputs into the electrical simulations. These were calculated by first multiplying the optical transmission (from the perovskite cells after passing through all layers before reaching the c-Si interface, and weighed over the AM 1.5 spectrum) with absorption coefficient of the c-Si, and multiplied by the Beer-Lambert exponential decay of absorption coefficient with the distance over the Si thickness. For the 3-T (IBC) tandem, since the nanowire grids (on perovskite) and metal back contact (on Si) can create internal reflection increasing the optical path, we compute the optical path length enchancement as a function of wavelength and then incorporated it into the generation rate matrix of Beer-Lambert calculation. Finally, the matrix of generation rate is integrated over 300 - 1300 nm wavelength across the distance of Si thickness.

An orthogonal conformal mesh is used for domain discretization to solve the drift-diffusion and electrostatic transport equation in 3-D simulations for 3-T (IBC) tandem, and 2-D simulations for 2-T and 4-T tandems (2-D simplification offers faster computational time, while yields only < 0.01 % deviation compared to the 3-D; likewise, it is not possible for the 3-T (IBC)). A conductive boundary approach is used in the simulation meaning that the diffusive transport at the space-charge regions

(e.g interface between c-Si and BSF, emitter, or FFE) is treated as recombination losses, while outside of these regions the transport is in quasi-neutral state. At the space-charge regions the surface recombination velocity, non-ideal dark saturation current densities, and contact resistivity are obtained using an analytical calculator provided by PV Lighthouse Pty. Ltd (EDNA2). According to a suggestion provided by Fell, et al [41], for self-consistency check, we run the simulation using different mesh refinement qualities ("coarse", "medium", "fine"), and relatively no mesh dependency is observed (less than 0.2 % variation). We calculate the PV parameters of the Si cells by running a DC-sweep from 0 to 0.7 V with 0.05 V interval. All PV parameters for Si cells obtained in this simulation are tabulated in **Figure 5.9**. The EQE of the Si cells is calculated using monochromatic (instead of broadband) generation calculations. This assumes 100 % injection efficiency, and even with a 15 % loss in the injection, the 3-T (IBC) tandem performance reduces by < 2 % absolute power conversion efficiency (**Figure 5.11**).

5.7.3 Tunnel junction for 3-T (IBC) tandem

The tunnel junction is one of the critical components in our 3-T (IBC) tandem architectures. It is composed of interfaces from TiO_2/a-Si:H (i)/n^{++}Si front floating

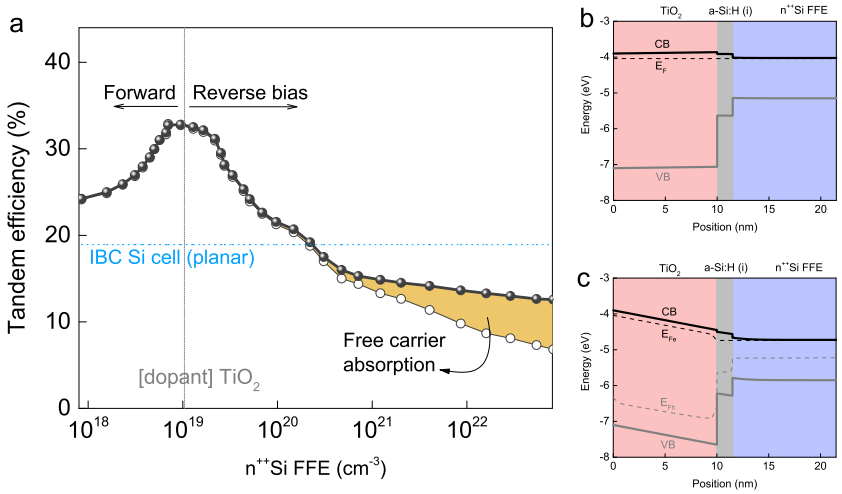

Figure 5.11: Tandem efficiency dependence on the tunneling layer. (**a**) Tandem efficiency (perovskite L_D = 10 μm) versus doping concentration of n^{++}Si front floating emitter. The doping concentration determines the direction of minority carrier flow (in this case electron); forward or reverse bias. The tandem efficiencies were calculated with (open circles) and without (filled circles) the free carrier absorption effect of n^{++}Si FFE which is more significant at higher concentrations. It shows two regimes of successful forward tunneling from perovskite-Si cells, and reverse tunneling from n^{++}Si FFE to the perovskite cells. Simulated band diagram across the tunnling layer at (**b**) thermal equilibrium, (**c**) forward bias condition.

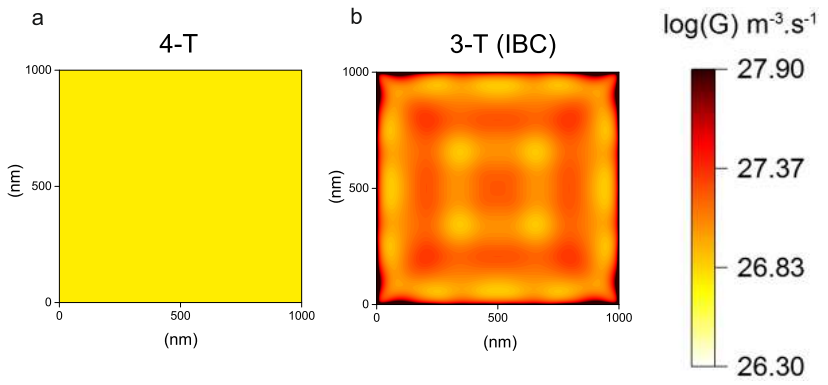

Figure 5.12: Charge generation rate near the perovskite bandgap (700 - 800 nm). (**a**) 4-T, and (**b**) 3-T (IBC), both of which are at their maximum performances (with perovskite thickness of 950 nm, and 550 nm (1 μm pitch) for 4-T and 3-T (IBC), respectively). The generation are values are averaged over the perovskite thickness showing uniform generation on the 4-T, whereas a quadrupole generation toward the grid corners emerged on the 3-T (IBC). This is associated with the origin of the increased EQE in the 3-T (IBC) near the perovskite bandgap (**Figure 5.4**).

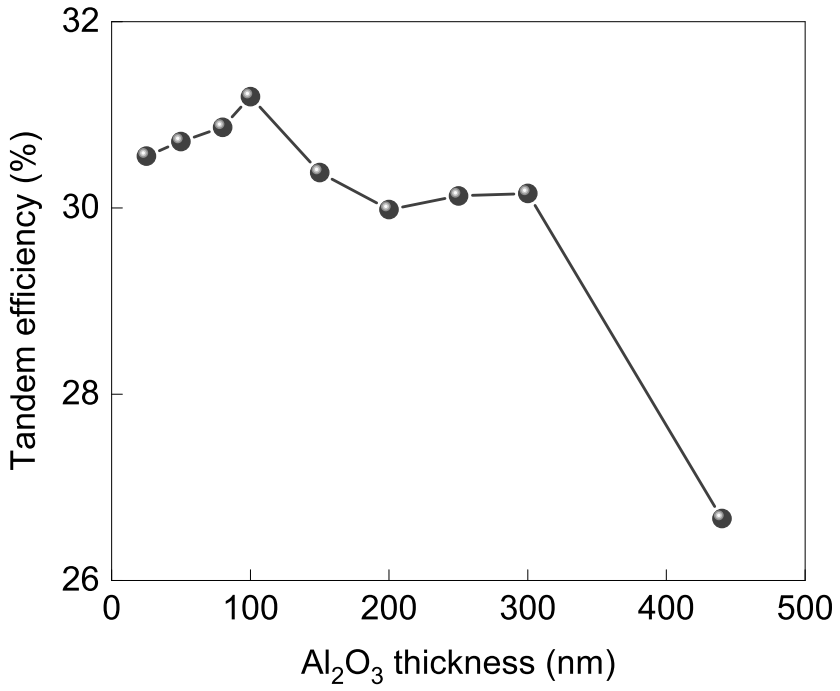

Figure 5.13: Positioning dependence of the nanogrid contact on 3-T (IBC) tandem efficiency (by varying insulator thickness). The simulation is performed using the optimized condition (550 nm perovskite thickness with 1 μm pitch). The tandem efficiency reaches maxima at 100 nm thick Al_2O_3 which further used on all of our simulations.

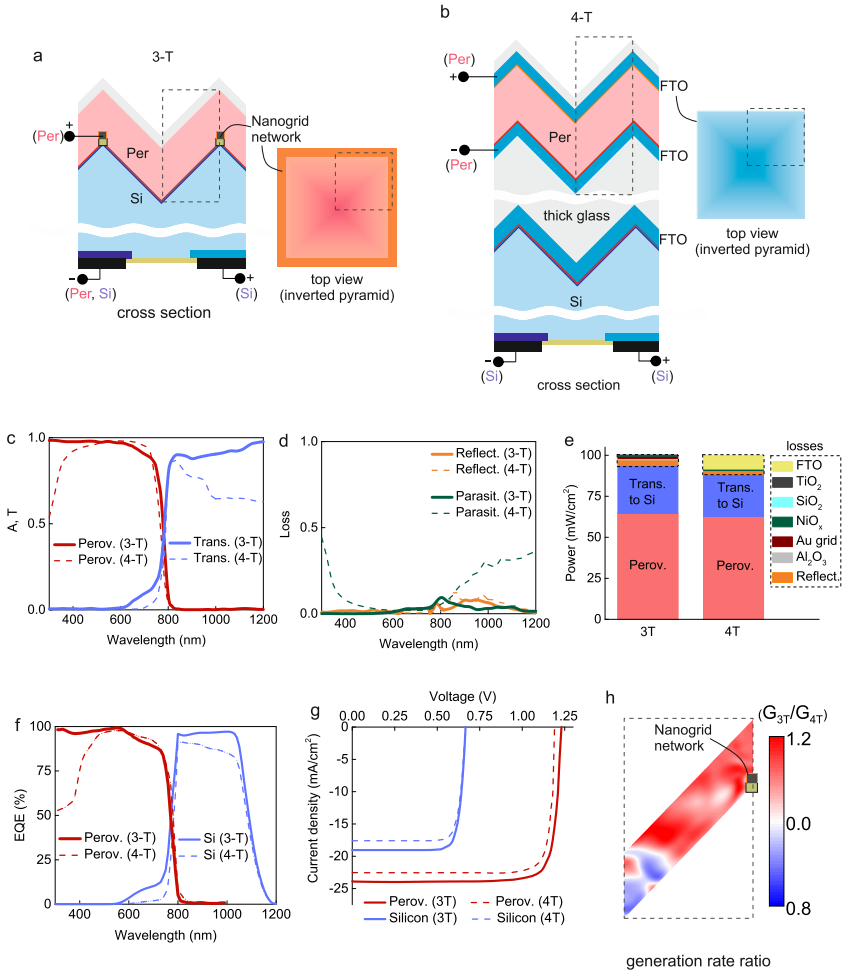

Figure 5.14: Textured cell simulation: perovskite-silicon tandem with 3-T (with nanoscale back contact perovskite) and 4-T configuration. (**a**) Schematic of the textured 3-T tandem with nanoscale back contact perovskite. (**b**) Schematic of the textured 4-T tandem. The dashed-green boxes represent the unit cell of our 3D coupled optical-electrical simulations. Note that both configurations use an optimized IBC-Si cell (25.03 % efficiency with pitch size of 1.6 μm or equivalent to characteristic angle of 54.7 $\circ o$) and the same perovskite thickness (550 nm) for an equivalent comparison. (**c**) Absorption spectra of the perovskite, and transmission through to the silicon cell. (**d**) Total loss spectra due to reflection and parasitic absorption. (**e**) Total optical power contribution of each layer integrated over AM 1.5 standard spectrum. (**f**) I-V curve independently extracted from the perovskite and silicon cells (corresponding values are tabulated in **Table 5.2**). (**g**) EQE spectra independently extracted from the perovskite and silicon cells. (**h**) cross-section view of generation rate ratio between 3-T and 4-T (G_{3T}/G_{4T}) within a unit cell of the textured perovskite, showing the generation rate is enhanced toward the nanogrid contact. This generation rate is integrated over the AM 1.5 standard spectrum. The electrical simulation was done with a 10 μm diffusion length perovskite, with all coupled optical-electrical simulation carried out in 3D.

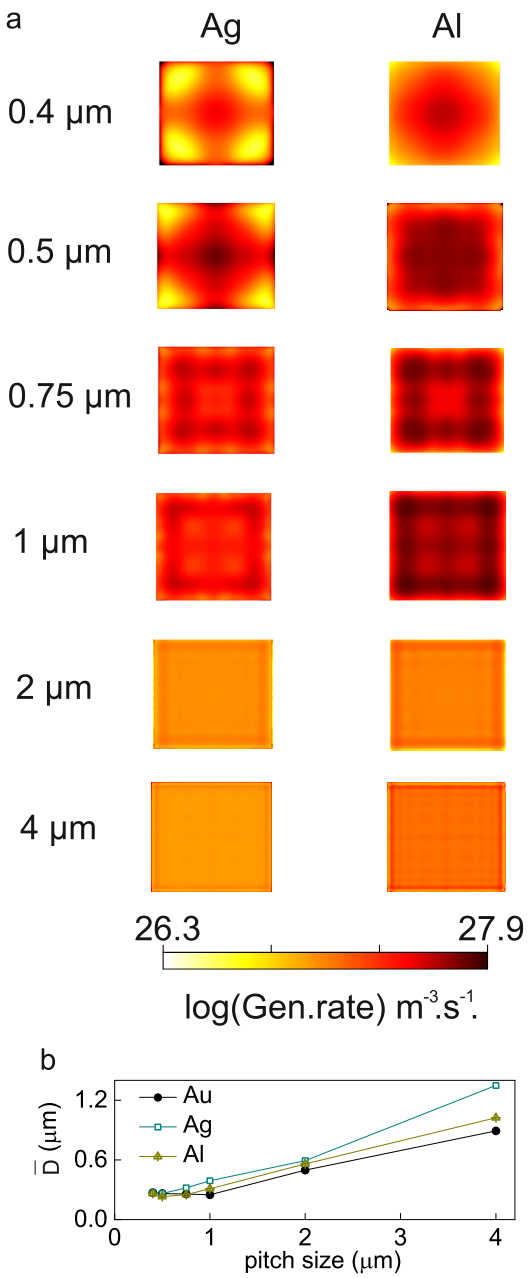

Figure 5.15: Photonic cavity effect using different grid metals. (**a**) Top view of charge generation rate in 3-T (IBC) showing charge concentratin toward the contact (edges of the squares) as the pitch size (values indicated on the most left) increases. Similar to **Figure 5.5c-d**, the generation rate profiles presented here are already integrated over the AM 1.5 solar spectrum, and averaged over the perovskite thickness inside the cavity. (**b**) Calculated effective collection distance ($\overline{D}$) as a function of pitch size. There is a slight shift of the minimum $\overline{D}$ using different metal, however the general trend is the same regardless of metal used, indicatig the effect is due more to the creation of a photonic cavity than plasmonic enhancement.

Table 5.2: PV parameters for the simulated textured cells.

Device	V_{oc} (V)	J_{sc} (mA/cm^2)	FF	PCE (%)
Perovskite 3-T	1.23	23.86	0.84	24.77
Perovskite 4-T	1.19	22.53	0.86	23.17
Silicon 3-T	0.67	19	0.83	10.5
Silicon 4-T	0.66	17.6	0.83	9.67
Tandem 3-T	-	-	-	35.27
Tandem 4-T	-	-	-	32.84

emitter (FFE). The FFE is saturated with electron injected from perovskite to TiO_2/a-Si:H (i), and from n^{++}Si back surface field (BSF)/p-Si base. Additionally, the generated electron (minority carriers) from the p-Si base will first diffuse to n^{++}Si and then will be injected back to the p-Si base [37].

We used Ebers-Moll model [60, 61] to describe how this tunnel junction works (e.g. using SPICE circuit simulation). In our simulation, we identify four criteria to ensure a successful electron tunneling from perovskite to the silicon cell: (1) forward bias injection for both perovskite and silicon cells, (2) Fermi level alignment across the depletion region, (3) thickness (doping profile depth) of the n^{++}Si FFE, (4) doping concentration of the n^{++}Si FFE.

We simulate two main junctions involved between perovskite and silicon layer, both of which should be forward biased and saturated in the n^{++}Si FFE for successful tunneling process (100 % injection efficiency). Both junctions are $CH_3NH_3PbI_3$/TiO_2/a-Si:H (i)/n^{++}Si FFE (for the perovskite cell), and p-Si base/n^{++}Si FFE (for the Si cell). Any reverse injection occurring within the depletion region could potentially drop the injection efficiency.

We need to prevent this reverse charge injection (electron back flow) across the depletion region n^{++}Si FFE/a-Si:H(i)/TiO_2/perovskite interfaces. The main requirement is to maintain a rectification of charge injection by Fermi level alignment through the depletion region. In our simulations, this is clearly visible from a large valence band offset within the depletion region. As a result the tunnel layer will block any hole transport (majority carrier) from the p-Si base to the perovskite cell, hence the n^{++}Si rear emitter contact.

This condition alone does not prevent the possibility of reverse charge injection. This happens when there is a "cut-off" decay between n^{++}Si FFE relative to n^{++}Si rear emitter. In other words, a proper thickness of the n^{++}Si FFE with a proper doping concentration relative to the fixed p-Si base doping concentration is required. to maintain 100 % injection, we use a 10 - 44 nm n^{++}Si FFE thickness, where the thickness less than 10 nm would give undesired excess carrier to be stored the n^{++}Si FFE instead of fully injected toward p-Si base. Any stored charge can be translated

further as a reverse charge injection (theoretical details are well explained by Hu [61], and Datta [59]).

Once we optimize the n^{++}Si FFE decay width (thickness), we need to ensure that the doping concentration of the n^{++}Si FFE is much higher than the p-Si base, but less than the n^{++}Si rear emitter contact. Shortly, this implies a lower potential difference in the n^{++}Si FFE/p-Si base interface than in the n^{++}Si rear emitter/p-Si base interface, and as a result the minority carrier (electron) generated on the p-Si base (on top of the n^{++}Si rear emitter) will tend to diffuse toward n^{++}Si FFE rather than being collected on the n^{++}Si rear emitter contact.

Conversely, electron charge injection in the depletion region between n^{++}Si FFE to the p-Si base interface is necessary for transporting the electrons (minority carriers) generated in region above the p^{++}Si FFE to the p-Si base interface is necessary for transporting the electrons (minority carriers) generated in region above the p^{++}Si BSF contact, through n^{++}Si FFE, and to the n^{++}Si rear emitter and contact for collection. This allows one to make the n^{++} and p^{++} back contact regions equally sized and spaced as originally proposed in the (Mercury cell) [37] IBC-Si used in our simulations. In order to achieve this condition alone, we set the resistivity of the p-Si base to be ~13.5 to 15 times higher than that of the n^{++}Si FFE. In other words, the doping concentration of n^{++}Si FFE should be much higher than the p-Si base for a successful "re-pumping" injection, but lower than the n^{++}Si rear emitter to prevent a reverse charge injection.

In addition to the minimum required decay width for electron transition time from n^{++}Si FFE to the p-Si base, the doping concentration of n^{++}Si FFE also contributes to a free-carrier (parasitic) absorption that reduces the tandem efficiency. We computed the influence of a range of doping concentrations of n^{++}Si FFE on this effect (**Figure 5.11**).

References

[1] A. Polman and H. A. Atwater, *Photonic design principles for ultrahigh-efficiency photovoltaics*, Nature Mat. **11**, 174 (2012).

[2] G. Connibeer, *Third-generation photovoltaics*, Mater. Today **10**, 42 (2007).

[3] A. D. Vos, *Detailed balance limit of the efficiency of tandem solar cells*, Journal of Physics D: Applied Physics **13**, 839 (1980).

[4] W. Shockley and H. J. Queisser, *Detailed balance limit of efficiency of p-n junction solar cells*, J.Appl.Phys. **32**, 510 (1961).

[5] A. Polman, M. Knight, E. C. Garnett, B. Ehrler, and W. C. Sinke, *Photovoltaic materials: present efficiencies and future challenges*, Science **352**, 4424 (2016).

[6] M. C. Beard, J. M. Luther, and A. J. Nozik, *The promise and challenge of nanostructured solar cells*, Nature Nano. **9**, 951 (2014).

[7] C. D. Bailie, M. G. Christoforo, J. P. Mailoa, A. R. Bowring, E. L. Unger, W. H. Nguyen, J. Burschka, N. Pellet, J. Z. Lee, M. Grätzel, R. Noufi, T. Bounassisi, A. Salleo, and M. D. McGehee, *Semi-transparent perovskite solar cells for tandem with silicon and CIGS*, Energy & Environmental Science **8**, 956 (2015).

[8] J. P. Mailoa, C. D. Bailie, E. C. Johlin, E. T. Hoke, A. J. Akey, W. H. Nguyen, M. D. McGehee, and T. Buonassisi, *A 2-terminal perovskite/silicon multijunction solar cell enable by a silicon tunnel junction*, Appl. Phys. Lett. **106**, 121105 (2015).

[9] S. Albrecht, M. Saliba, J. P. C. Baena, F. Lang, L. Kegelmann, M. Mews, L. Steier, A. Abate, J. Rappich, L. Korte, R. Schlatmann, M. K. Nazeeruddin, A. Hagfeldt, M. Grätzel, and B. Recha, *Monolithic perovskite/silicon-heterojunction tandem solar cells processed at low temperature*, Energy & Environmental Science **9**, 81 (2016).

[10] J. Werner, C-H. Weng, A. Walter, L. Fesquet, J. P. Seif, S. D. Wolf, B. Niesen, and C. Ballif *Efficient monolithic perovskite/silicon tandem solar cell with cell area >1 cm^2*, J.Phys.Chem.Lett. **7**, 161 (2016).

[11] B. Chen, Y. Bai, Z. Yu, T. Li, X. Zheng, Q. Dong, L. Shen, M. Boccard, A. Gruverman, Z. Holman, and J. Huang *Efficient semitransparent perovskite solar cells for 23.0%-efficiency perovskite/silicon four-terminal tandem cells*, Adv.Energy.Mat. **6**, 1601128 (2016).

[12] D. P. McMeekin, G. Sadoughi, W. Rehman, G. E. Eperon, M. Saliba, M. T. Hörantner, A. Haghighirad, N. Sakai, L. Korte, B. Rech, M. B. Johnston, L. M. Herz, and H. J. Snaith *A mixed-cation lead mixed-halide perovskite absorber for tandem solar cells*, Science **351**, 151 (2016).

[13] J. Werner, L. Barraud, A. Walter, M. Bräuninger, F. Sahli, D. Sacchetto, N. Tétreau, B. Paviet-Salomon, S-J. Moon, C. Allebé, M. Despeisse, S. Nicolay, S. D. Wolf, B. Niesen, and C. Ballif *Efficient near-infrared transparent perovskite solar cells enabling direct comparison of 4-terminal and monolithic perovskite/silicon tandem cells*, ACS Energy Lett. **1**, 474 (2016).

[14] J. M. Gee *A comparison of different module configurations for multi-band-gap solar cells*, Sol. Cells **24**, 147 (1988).

[15] J. P. Mailoa, M. Lee, I. M. Peters, T. Buonassisi, A. Panchula, and D. N. Weiss *Energy-yield prediction for II-VI-based thin-film tandem solar cells*, Energy Environ. Sci. **9**, 2644 (2016).

[16] M. H. Futscher and B. Ehrler *Efficiency limit of perovskite/Si tandem solar cells*, ACS Energy Lett. **1**, 863 (2016).

[17] M. W. Rowell and M. D. McGehee *Transparent electrode requirements for thin film solar cell modules*, Energy Environ. Sci. **4**, 131 (2011).

[18] T. Nagashima, K. Okumura, K. Murata, and Y. Kimura *Three-terminal tandem solar cells with a back-contact type bottom cell*, IEEE PV. Specialists conference **15**, 1193 (2000).

[19] A. Marti and A. Luque *Three-terminal heterojunction bipolar transistor solar cell for high-efficiency photovoltaic conversion*, Nature Comm. **6**, 6902 (2015).

[20] S. Sista, Z. Hong, M-H. Park, Z. Xu, and Y. Yang *High-efficiency polymer tandem solar cells with three-terminal structure*, Adv. Mater. **22**, 77 (2010).

[21] D. Bahro, M. Koppitz, A. Mertens, K. Glaser, J. Mescher, and A. Colsmann *Understanding the external quantum efficiency of organic homo-tandem solar cells utilizing a three-terminal device architecture*, Adv. Mater. **5**, 1501019 (2015).

[22] M. A. Steiner, M. W. Wanlass, J. J. Carapella, A. Duda, J. S. Ward, T. E. Moriarty, and K. Emery *A monolithic three-terminal GaInAsP/GaInAs tandem solar cell*, Prog. Photovoltaics **17**, 587 (2009).

[23] M. Dürr, A. Bamedi, A. Yasuda, and G. Nelles *Tandem dye-sensitized solar cell for improved power conversion efficiencies*, Prog. Photovoltaics **84**, 3397 (2004).

[24] S. A. Mann, R. R. Grote, R. M. Osgood Jr, A. Alu, and E. C. Garnett *Opportunities and limitations for nanophotonic structures to exceed the Shockley-Queisser limit*, ACS Nano **10**, 8620 (2016).

[25] Y. Cui, D. van Dam, S. A. Mann, N. J. J. van Hoof, P. J. Veldhoven, E. C. Garnett, E. P. A. M. Bakkers, and J. E. M. Haverkort *Boosting solar cell photovoltage via nanophotonic engineering*, Nanolett. **16**, 6467 (2016).

[26] W. Ko, T. T. D. Tran, I. Bhattacharya, K. W. Ng, H. Sun, and C. Chang-Hasnain *Illumination angle insensitive single indium phosphide tapered nanopillar solar cell*, Nano Lett. **15**, 4961 (2015).

[27] M. A. Green, K. Emery, Y. Hishikawa, W. Warta, E. D. Dunlop, D. H. Levi, and A. W. Y. Ho-Baillie *Solar cell efficiency tables (version 49)*, Prog. Photovoltaics. **15**, 3 (2017).

[28] A. N. Jumabekov, E. Della Gaspera, Z. -Q. Xu, A. S. R. Chesman, J. van Embden, S. A. Bonke, Q. Bao, D. Vak, and U. Bach *Back-contact hybrid organic-inorganic perovskite solar cells*, J. Mater. Chem. C **4**, 3125 (2016).

[29] C. M. Hangarter, R. Debnath, J. Y. Ha, M. A. Sahiner, C. J. Reehil, W. A. Manners, and D. Josell *Photocurrent mapping of 3D CdSe/CdTe windowless solar cells*, ACS Appl. Mater. Interfaces **5**, 9120 (2013).

[30] J. van de Groep, P. Spinelli, and A. Polman *Transparent conducting silver nanowire networks*, Nano Lett. **12**, 3138 (2012).

[31] B. Sciacca, J. van de Groep, A. Polman, and E. C. Garnett *Solution-grown silver nanowire ordered arrays as transparent electrodes*, Adv. Mater. **28**, 905 (2016).

[32] E. C. Garnett, W. Cai, J. J. Cha, F. Mahmood, S. T. Connor, M. G. Christoforo, Y. Cui, M. D. McGehee, and M. L. Brongersma *Self-limited plasmonic welding of silver nanowire junctions*, Nature Mater. **11**, 241 (2012).

[33] J-Y. Lee, S. T. Connor, Y. Cui, and P. Peumans *Solution-processed metal nanowire mesh transparent electrodes*, Nano Lett. **8**, 689 (2008).

[34] J. Bai, X. Duan, and Y. Huang *Rational fabrication of graphene nanoribbons using a nanowire etch mask*, Nano Lett. **9**, 2083 (2009).

[35] X. Li, D. Bi, C. Yi, J-D. Decoppet, J. Luo, S. M. Zakeeruddin, A. Hagfeldt, and M. Grätzel *A vacuum flash-assisted solution process for high-efficiency large-area perovskite solar cells*, Science **353**, 58 (2016).

[36] A. R. Burgers, N. Guilevin, A. A. Mewe, A. Suvvi, P. Spinelli, A. W. Weeber, and I. Cesar *FFE IBC cells: impact of busbars on cell performance with circuit modelling*, Energy Procedia **77**, 21 (2015).

[37] I. Cesar, N. Guillevin, A. R. Burgers, A. A. Mewe, M. Koppes, J. Anker, L. J. Geerligs, and A. W. Weeber *Mercury: a back junction back contact front floating emitter cell with novel design for high efficiency and simplified processing*, Energy Procedia **55**, 633 (2014).

[38] FDTD Solutions, http://www.lumerical.com (access date March 12 (2017).

[39] K. R. McIntosh and S. C. Baker-Finch *Rapid optical simulation of silicon solar cells*, Proceedings of the 38th IEEE Photovoltaic Specialists Conference, Austin, Texas (2012).

[40] DEVICE CT Solutions, http://www.lumerical.com (access date March 12 (2017).

[41] A. Fell, K. C. Fong, K. R. McIntosh, E. Franklin, and A. W. Blakers *3-D Simulation of interdigitated-back-contact silicon solar cells with Quokka including perimeter losses*, IEEE Journal of Photovolt. **4**, 1040 (2014).

[42] A. Richter, M. Hermle, and S. Glunz *Reassessment of the limiting efficiency for crystalline silicon solar cells*, IEEE Journal of Photovolt. **3**, 1184 (2013).

[43] J. Eisenlohr, G. B. Lee, J. Benick, F. Feldmann, M. Drieβen, N. Milenkovic, B. Bläsi, J. C. Goldschmidt, and M. Hermle *Rear side sphere gratings for improved light trapping in crystalline silicon single junction and silicon-based tandem solar cells*, Sol. Energy Mater. Sol. Cells. **142**, 60 (2015).

[44] J. Eisenlohr, N. Tucher, H. Hauser, M. Graf, J. Benick, B. Bläsi, J. C. Goldschmidt, and M. Hermle *Efficiency increase of crystalline silicon solar cells with nanoimprinted rear side gratings for enhanced light trapping*, Sol. Energy Mater. Sol. Cells. **155**, 288 (2016).

[45] P. Löper, M. Stuckelberger, B. Niesen, J. Werner, M. Filipič, S. J. Moon, J. H. Yum, M. Topič, S. D. Wolf, and C. J. Ballif *Complex refractive index spectra of $CH_3NH_3PbI_3$ perovskite thin films determined by spectroscopic ellipsometry and spectrophotometry*, J. Phys. Chem. Lett. **6**, 66 (2015).

[46] S. D. Wolf, J. Holovsky, S. J. Moon, P. Löper, B. Niesen, M. Ledinsk, F. J. Haug, J. H. Yum, and C. J. Ballif *Organometallic halide perovskites: sharp optical absorption edge and its relation to photovoltaic performance*, J. Phys. Chem. Lett. **5**, 1035 (2014).

[47] M. A. Green *Self-consistent optical parameters of intrinsic silicon at 300 K including temperature coefficients*, Sol. Energy Mat. & Solar Cells **92**, 1305 (2008).

[48] J. M. Ball, S. D. Stranks, M. T. Hörantner, S. Hüttner, W. Zhang, E. J. W. Corssland, I. Ramirez, M. Reide, M. B. Johnston, R. H. Friend, and H. J. Snaith *Optical properties and limiting photocurrent of thin-film perovskite solar cells*, Energy & Environ. Sci. **8**, 602 (2015).

[49] D. T. Pierce and W. E. Spicer *Electronic structure of amorphous Si from photoemission and optical studies*, Phys. Rev. B **5**, 3017 (1972).
[50] S. C. Baker-Finch and K. R. McIntosh *Reflection of normally incident light from silicon solar cells with pyramidal texture*, Prog. in Photovolt: Research and App. **19**, 406 (2011).
[51] E. Palik, *Handbook of Optical Constants of Solids*, Academic Press, Orlando, 1985.
[52] P. B. Johnson and R. W. Christy *Optical constants of the noble metals*, Phys. Rev. B **6**, 4370 (1972).
[53] S. C. Baker-Finch and K. R. McIntosh *A freeware program for precise optical analysis of the front surface of a solar cell*, Proceedings of the 35th IEEE Photovoltaic Specialists Conference, Honolulu, Hawai (2010).
[54] M. A. Green *Solar cell fill factor - general graph and empirical expressions*, Phys. Rev. B **24**, 788 (1981).
[55] S. C. Baker-Finch, K. R. McIntosh, D. Yan, K. C. Fong, and T. C. Kho *Near-infrared free carrier absorption in heavily doped silicon*, J. App. Phys. **116**, 116 (2014).
[56] I. Almansouri, M. A. Green, and A. Ho-Ballie, *The ultimate efficiency of organolead halide perovskite solar cells limited by Auger*, J. Mat. Research **31**, 2197 (2016).
[57] R. Varache, C. Leendertz, M. E. Gueunier-Farret, J. Haschke, D. Muñoz, and L. Korte, *Investigation of selective junctions using a newly developed tunnel current model for solar cell applications*, Sol. Energy Mat. & Solar Cells **141**, 14 (2015).
[58] J. P. Correa-Baena, M. Anaya, G. Lozano, W. Tress, K. Domanski, M. Saliba, T. Matsui, T. J. Jacobsson, M. E. Calvo, A. Abate, M. Grätzel, M. Míguez, and A. Hagfeldt *Unbroken perovskite: interplay of morphology, electro-optical properties, and ionic movement*, Adv. Mater. **28**, 5031 (2016).
[59] S. Datta, *Electronic Transport in Mesoscopic System*, Cambridge University Press, New York, 1995.
[60] S. M. Sze, *Physics of Semiconductor Devices*, John Wiley & Sons, Canada, 1981.
[61] C. C. Hu, *Modern Semiconductor Devices for Integrated Circuits*, 351 Prentice Hall, New Jersey, 2010.
[62] A. D. Yaghijan, *Internal energy, Q-energy, poynting's theorm, and the stress dyadic in dispersive material*, IEEE Trans. Antennas. Propag. **55**, 14955 (2007).
[63] S. D. Stranks, G. E. Eperon, G. Grancini, C. Menelaou, M. J. P. Alcocer, T. Leijtens, L. M. Herz, A. Petrozza, and H. J. Snaith, *Electron-hole diffusion lengths exceeding 1 micrometer in an organometal trihalide perovskite absorber*, Science **342**, 341 (2013).

Summary

Semiconductors have been an integral element in our 21st century society. We find semiconductors at the heart of every electronic device such as microprocessor chip, transistor, as well as light-emitting diode (LED). Although, the seminal theory of semi-conductors was proposed by A.H. Wilson in 1931 after the birth of quantum mechanics, the main impetus of the fast development of semiconductors for devices, perhaps only came after several ground breaking experiments in transistors by W.B. Shockley, J. Bardeen, and W.H. Brattain who received the Nobel prize in 1956. Rapid progress in techniques to deposit and study semiconductor interfaces in the 1980s helped close the gap between our knowledge in solid-state physics semiconductor and light science, most recently exemplified by the LED. An energy-efficient LED can reduce electricity consumption by about 75%. High-efficiency LEDs are enabled by high quality GaN semiconductor films, firstly introduced by I. Akasaki, H. Amano, and S. Nakamura who received the Nobel prize in 2014. They introduced a growth technique to make uniform nucleation, non-selective growth, and good coalescence that leads to reduce defect density in GaN.

On the other hand, advances in thin-film semiconductor technology will also find applications in highly efficient and low-cost photovoltaics. Hybrid-halide perovskites have emerged over the unprecedented timeframe over the last 6 years as a promising class of materials for such applications. Most notably, their solar cells have achieved power conversion efficiencies above 20 % in the laboratory, even though many fundamental questions still remain unanswered. Therefore for halide perovskite thin-films to have an impact beyond the laboratory requires a systematic understanding and eliminating sources of losses.

In Chapter 1 we outline the methodology used in this thesis to improve our understanding, while pointing the way forward to eliminate the losses and ultimately design even better devices. Technically the development cycle involves controlled and clean experimental systems along with careful measurements and full optoelectronic modelling/theory to verify, and quantify the losses in halide perovskite thin-films. By quantifying and considering all of the losses, the ultimate goal is directed at designing a novel architecture device that potentially exceeds the performance and relaxes the limitations of traditional solar cell configurations.

In Chapter 2 we report experimental values of carrier diffusion lengths in halide perovskite thin films and describe how processing, composition, aging and surface passivation affect the results. Considering the many possibilities for all three ions in the halide perovskite structure, hundreds of distinct compositions have already been reported. Such compositional changes can alter the carrier diffusion length - a key parameter for solar cell performance. Given the large compositional and processing parameter space, a rapid and simple technique for directly measuring diffusion length is needed. Here we use a laser grating technique to screen the diffusion length in perovskite materials. First, in pure $CH_3NH_3PbI_3$ we observe the diffusion length is largely dependent on the controlled processing conditions. Next, we partially replace iodide (I) with bromide (Br) and show that surprisingly, the diffusion length increases after aging for 1 month in air. Finally, we use a 4-nm Al_2O_3 layer (atomic layer deposition) to passivate the surface of $CH_3NH_3PbBr_3$, leading to a remarkable increase in diffusion length from 201 nm to 532 nm. The correlation that we have established between materials processing and diffusion length offers guidance in how to improve materials for devices.

In Chapter 3 we describe the use of electron backscattering diffraction (EBSD) to properly determine the grain boundary locations in halide perovskite thin-films. Grain boundaries play a key role in the performance of thin-film optoelectronic devices and yet their effect in halide perovskite materials is still not understood. The biggest factor limiting progress is the inability to identify grain boundaries; the gold standard - EBSD - destroys halide perovskite thin films. Non-crystallographic techniques commonly misidentify grain boundaries, leading to conflicting literature reports about their influence. Here we solve this problem using a solid-state EBSD detector with 6,000 times higher sensitivity than the traditional phosphor screen and camera. We used the crystal misorientation data set from the EBSD to model the characteristics of grain boundary interface energy in $CH_3NH_3PbBr_3$ thin-films, and show that the halide perovskite grains do not exhibit twinning. In addition, we find a peculiar case, where the grain boundary very likely consists of amorphous halide perovskites.

In Chapter 4 we attempt to correlate the true grain size with photoluminescence lifetime, carrier diffusion length, and mobility in halide perovskites. We find that the grain boundaries are not benign as is often claimed, but have a recombination velocity of 1670 cm/s, comparable to that of crystalline silicon. However, as with silicon, amorphous perovskite can passivate crystalline boundaries, leading to brighter photoluminescence and longer carrier lifetime without reducing diffusion length. This variable grain boundary character explains the mysteriously long lifetime and record efficiency achieved in small grain halide perovskite thin films, while pointing the way forward to even better performance.

In Chapter 5 we use our understanding of the losses to design a novel device architecture - nanoscale back-contact perovskite solar cell to improve tandem efficiency. Using coupled optical-electrical modelling, we optimize this architecture for a planar perovskite-silicon tandem, highlighting the roles of nanoscale contacts to reduce the required perovskite electronic quality such as minority carrier diffusion length. We discuss the advances of our design over the traditionally used two- (2-T) and four-

terminal tandem (4-T), and point the way towards further improvements enabled by our design such as surface texturing, surface passivation and photoluminescence outcoupling.

Samenvatting

Halfgeleiders zijn onmisbaar in onze 21e-eeuwse maatschappij. We kunnen halfgeleiders vinden in de kern van elk elektronisch apparaat, zoals de microprocessor chip, transistors en licht-emitterende diodes (LED). Hoewel de rudimentaire theorie van de halfgeleiders al was voorgesteld in 1931 door A.H. Wilson na de geboorte van de kwantummechanica, kwam de voornaamste impuls voor de snelle ontwikkeling van halfgeleiders voor apparaten kwam pas na verscheidene baanbrekende experimenten met transistors door W.B. Shockley, J. Bardeen, en W.H. Battain, die daarvoorde in 1956 de Nobelprijs hebben ontvangen. Razendsnelle technologische ontwikkelingen tussen 1980 en 1990 om halfgeleiders te deponeren en de grensvlakken te bestuderen hielpen om de kloof te dichten tussen onze kennis van vaste-stof halfgeleiderfysica en de wetenschap van het licht ("fotonica"). Een goed voorbeeld hiervan is de LED. Een energiezuinige LED kan het elektriciteitsverbruik met ongeveer 75 % verminderen. LEDs met een hoge efficiëntie zijn mogelijk door het gebruik van een dunne laag gallium nitride (GaN) van hoge kwaliteit. Deze zijn voor het eerst geïntroduceerd door I. Akasaki, H. Amano, en S. Nakamura, die daarvoor in 2014 de Nobelprijs in ontvangst namen. Deze wetenschappers introduceerden een kristalgroeitechniek waarmee uniforme nucleatie, non-selectieve groei en goede samensmelting mogelijk werden wat vervolgens leidde tot een vermindering in de defectendichtheid in GaN.

Anderzijds zal de vooruitgang in dunne-film halfgeleidertechnologie ook toepassingen vinden in fotovoltaïca met hoge efficiëntie en lage kosten. Hybride-halide perovskieten zijn een categorie materialen welke in een uitzonderlijk korte tijdspanne van 6 jaar een enorme opkomst hebben gemaakt voor dergelijke toepassingen. Hybride-halide perovskiet zonnecellen hebben een elektriciteitsopwekkingefficiëntie van 20 % bereikt in het laboratorium, ondanks dat vele fundamentele vragen nog steeds onbeantwoord zijn. Om dunne-film halide perovskite ook buiten het laboratorium een impact te laten hebben is het nodig om systematisch ons begrip te vergroten en oorzaken van energieverlies te elimineren.

In hoofdstuk 1 wordt de onderzoeksmethodologie van deze thesis geschetst. Hierin verbeteren wij onze kennis en wijzen wij de weg naar het elimineren van verliezen om uiteindelijk betere apparaten te ontwerpen. Vanuit een technisch oogpunt heeft het

ontwikkelingsproces gecontroleerde en schone experimentele systemen nodig, gecombineerd met zorgvuldige metingen en volledige optisch-elektronische modellering en bijbehorende theorie om de verliezen in halide-perovskiet dunne films te kunnen verifiÃ«ren en kwantificeren. Door alle verliezen te kwantificeren en doorgrondig te onderzoeken wordt het uiteindelijke doel gestuurd richting het ontwerpen van een apparaat met een nieuwe architectuur, die mogelijk de prestaties en beperkingen overtreft van traditionele zonnecelconfiguraties.

In Hoofdstuk 2 rapporteren wij experimentele waarden van energiedragerdiffusielengtes in halide perovskiee dunne films en beschrijven we hoe de verwerking, samenstelling, veroudering en oppervlaktepassivering invloed heeft op de resultaten. Omdat er veel verschillende samenstellingsmogelijkheden zijn voor de drie ionen in de halogenide perovskietstructuur zijn er al honderden verschillende samenstellingen gerapporteerd. Dergelijke wijzigingen in de samenstelling kunnen de energiedragerdiffusielengte veranderen - dit is een kernparameter voor zonnecelprestaties. Aangezien er vele mogelijkheden zijn voor de samenstelling en de verwerking is een snelle en eenvoudige techniek voor het direct meten van de diffusielengte nodig. Wij hebben gebruik gemaakt van een laser-traliewerk techniek om de diffusielengtes van perovskieten door te lichten. Ten eerste, in zuiver $CH_3NH_3PbI_3$ observeren we dat de diffusielengte grotendeels afhankelijk is van de vervaardigingsomstandigheden. Vervolgens vervangen we gedeeltelijk de jodide (I) ionen met bromide (Br). Verrassend genoeg observeren wij dat de diffusielengte toeneemt na blootstelling aan de lucht gedurende één maand. Ten slotte deponeren wij een 4-nm Al_2O_3-laag (door middel van atomaire laag depositie; ALD) op het oppervlak van $CH_3NH_3PbBr_3$ om deze te passiveren. Dit zorgde voor een opmerkelijke toename in diffusielengte van 201 nm naar 532 nm. De correlatie die we hebben vastgesteld tussen materiaalvervaardiging en diffusielengte biedt richtlijnen voor toepassing in apparaten.

In hoofdstuk 3 beschrijven we het gebruik van elektron-terugverstrooiingdiffractie (EBSD) om de korrelgrenslocaties in halide perovskite dunne films nauwkeurig te bepalen. Korrelgrenzen hebben een grote invloed op de prestaties van dunne film opto-elektronische apparaten en toch wordt hun effect in halide perovskieematerialen nog steeds niet begrepen. De grootste voortuitgangsbeperkende factor is het onvermogen om korrelgrenzen te identificeren; de gouden standaard - EBSD - vernietigt halogeen perovskiet dunne films. Niet-kristallografische technieken lijden onder het vaak misidentificeren van korrelgrenzen, wat leidt tot tegenstrijdige experimentele data in de literatuur over de invloed van deze korrelgrenzen. Dit probleem lossen wij op met behulp van een vaste-stoft EBSD-detector met een 6000 maal hogere gevoeligheid dan een traditioneel fosforscherm met een camera. Wij maken gebruik van de kristalmisoriëntatiedataset van de EBSD om de kenmerken van de korrelgrens grensvlak-energie in $CH_3NH_3PbBr_3$ dunne films te modelleren. Deze gegevens laten zien dat halogenide perovskiet korrels geen tweelingeffecten vertonen. Verder vonden wij een bijzondere situatie waarbij de korrelgrens van dit geval zeer waarschijnlijk bestaat uit amorfe halogenide perovskieten.

In Hoofdstuk 4 proberen we de ware korrelgrootte te correleren met fotoluminescentielevensduur, de energiedragerdiffusielengte en -mobiliteit in halogenide perovskieten.

Verder ontdekken we dat de korrelgrenzen niet onschuldig zijn zoals vaak wordt beweerd. Deze korrelgrenzen hebben namelijk een recombinatie snelheid van 1670 cm/s. Dit is vergelijkbaar met de recombinatiesnelheid van kristallijn silicium. Echter kan amorf perovskiet, net als silicium, kristallijne grenzen passiveren, wat leidt tot helderdere fotoluminescentie en een langere levensduur van de ladingsdragers zonder de diffusielengte te verminderen. Dit variabele karakter van de korrelgrenzen verklaart de verrassend lange levensduur en recordefficiëntie welke bereikt wordt in klein-korrelige halide perovskiet dunne films. Verder wijst het ook de weg voorwaarts naar nog betere prestaties.

In hoofdstuk 5 gebruiken we ons begrip van de verliezen om een apparaat met een nieuwe architectuur te ontwerpen: perovskietzonnecellen met een nanoschaal contact aan de achterkant om zo de tandemefficiëntie te verbeteren. Met behulp van gekoppelde optisch-elektrische modellering, optimaliseren we deze architectuur voor een vlakke perovskiet-silicium tandem. Hierbij leggen we de nadruk op de rol van de nanoschaal contacten om de vereiste elektronische kwaliteit van perovskiet te verminderen, zoals de diffusielengte van minderheidsenergiedragers. Ook wordt de vooruitgang van ons ontwerp ten opzichte van de traditioneel gebruikte twee- (2-T) en vier-contacten (4-T) tandem zonnecellen besproken en wijzen we de weg naar verdere verbeteringen die mogelijk zijn met ons ontwerp zoals oppervlaktetextureren, oppervlaktepassivering en fotoluminescentieuitkoppelingsefficiëntie.

Ringkasan

Semikonduktor sudah menjadi kesatuan utuh dalam kehidupan manusia abad-21. Kita menemukan semikonduktor dalam setiap komponen alat elektronik seperti mikroprosesor, transistor, termasuk didalamnya lampu LED. Dasar teori lahirnya semikonduktor pertama kali diajukan oleh A.H. Wilson pada tahun 1931 setelah lahirnya mekanika kuantum, meski dari itu penerapan semikonduktor itu sendiri baru berkembang pesat setelah beberapa eksperimen terobosan pada transistor yang dilakukan oleh W.B. Shockley, J. Bardeen, dan W.H. Brattain (penerima hadiah Nobel 1956). Perkembangan pesat berikutnya terjadi ditahun 1980an dimana pengetahuan tentang cara memproses, dan pengkarakterisasian semiconductor telah membantu kita dalam menjembatani dua bidang penting yaitu dasar fisika struktur dan ilmu cahaya. Contoh paling penting yaitu lahirnya lampu LED yang mampu mengurangi konsumsi listrik sebesar 75 %. Faktor keberhasilan utamanya terletak pada penggunaan GaN semikonduktor material berkualitas tinggi, yang pertama kali di pelopori oleh I. Akasaki, H. Amano, dan S. Nakamura (penerima hadiah Nobel 2014). Dimana mereka berhasil memperkenalkan cara membuat lapisan tipis GaN dengan proses pembibitan atom secara merata, tidak terlokalisasi, dan membentuk kesatuan kristal yang mampu mengurai jumlah cacat material.

Pada sisi lain, kemajuan dalam teknologi lapisan tipis semikonduktor sudah terbukti untuk menghasilkan sel surya yang sangat efisien namun murah. Hibrida-halogen perovskait adalah jenis mineral baru, yang dalam waktu singkat 6 tahun sudah membuktikan diri memenuhi kriteria diatas. Terbukti dengan efisiensi sel surya yang dihasilkan sudah diatas 20 % di skala laboratorium, meskipun banyak dasar-dasar sains yang belum diketahui mengapa material ini begitu efisien. Maka dari itu agar Hibrida-halogen perovskait ini bisa berdampak lebih luas dibutuhkan pemahaman sains mendasar yang sistematis, serta cara untuk mengurai jumlah cacat material yang dimilikinya.

Pada Bab 1 kami menjelaskan metodelogi yang digunakan di disertasi ini untuk memahami sains mendasar tersebut. Sekaligus memberikan saran penting bagaimana mengurai jumlah cacat material, yang pada akhirnya kami mengajukan terobosan desain baru untuk merancang solar cell yang lebih efisien. Secara teknis ini mencakup pembangunan ide bagaimana membuat sistem penelitian yang bersih, terpercaya dan teliti, yang kemudian menggabungkannya dengan teknik permodelan serta teori yang

utuh dengan tujuan untuk memverifikasi, mengidentifikasi, dan menghitung sumber sumber cacat dari hibrida-halogen perovskait. Dengan semua cara ini, kita pada akhirnya akan bisa membuat teknologi sel surya baru yang melebihi, dan mengurai keterbatasan dari teknologi yang ada sekarang.

Pada Bab 2 kami melaporkan hasil pengukuran seberapa jauh muatan listrik bisa mengalir di hibrida-halogen perovskait ini, dan menjelasakan bagaimana teknik pemrosesan, komposisi, penuaan, dan pelapisan permukaan mempengaruhi persepsi kita akan hasil penelitian. Walaupun hanya memiliki tiga jenis ion dalam struktur materialnya, namun kombinasi dari ketiganya mampu mengasilkan ratusan jenis kombinasi struktur yang berbeda-beda. Semua kombinasi ini akan mempengaruhi hasil pengukuran tersebut, terutama panjang muatan listrik yang mampu mengalir karena ini merupakan komponen penting untuk aplikasi sel surya. Kita mengajukan teknik pengukuran yang mampu mengukur parameter panjang muatan listrik ini dengan cara cepat dan tepat. Teknik ini menggunakan cahaya laser untuk membuat pola interferensi permukaan. Pertama, kita menemukan bahwa pada jenis material perovskait murni pun, $CH_3NH_3PbI_3$, pengukuran panjang muatan listrik bisa berbeda beda tergantung bagaimana kita membuatnya. Kemudian kita secara bertahap mengganti iodida (I) dengan bromida (Br) dan hasilnya panjang muatan listrik bisa bertambah setelah didiamkan selama 1 bulan di udara. Akhirnya, kami menggunakan lapisan tipis Al_2O_3 sebesar 4-nm (pembuatan dengan cara atom per atom) untuk mengisolasi permukaan, dan hasilnya panjang muatan listrik pertambah dari 201 nm menuju 532 nm. Korelasi penting ini akan menjadi panduan penting bagimana meningkatkan kualitas material untuk aplikasi yang dibutuhkan.

Pada Bab 3 kami menjelaskan penggunaan teknik elektron backsketering difraksi (EBSD) untuk mengidentifikasi dengen benar keberadaan dan lokasi dari kristal batas dari lapisan tipis hibrida halida perovskite. Pengetahuan akan kristal batas ini menjadi begitu penting mengingat perannya di hibrida halida perovskite sangatlah ambigu. Faktor penghalang utamanya yaitu ketidakjelasan akan konsensus yang digunakan dalam menentukan lokasi kristal batas ini. Konsensus standard seperti EBSD tidak mampu membantu karena biasanya langsung menghancurkan material ini ketika diterapkan. Kami menyelesaikan masalah ini dengan menggunakan detektor padat jenis baru yang memiliki sensitifitas 6000 kali detektor EBSD yang ada sekarang seperti kamera, dan jendela klasik phosporus. Kami menggunakan informasi dari misorientasi kristal untuk memodelkan dan mengkarakterisasi jenis kristal batas tersebut, dan kemudian total rugi-rugi energi yang ada di kristal batas tersebut. Kami menemukan kristal batas di $CH_3NH_3PbBr_3$ tidak memiliki kristal kembar seperti material pada umumnya, namun kristal batasnya memiliki karakteristik yang sangat tidak jelas sekaligus penting.

Pada Bab 4 kami mencoba untuk mencari hubungan antara ukuran kristal yang asli dari informasi EBSD dengan waktu hidup emisi cahaya, panjang, dan mobilitas dari muatan listrik yang dihasilkannya. Kami berkesimpulan bahwa kristal batas di hibrida-halida perovskait tidaklah bermanfaat, sebagaimana diklaim sebelumnya, namun memiliki kecepatan rugi rugi sebesar 1670 cm/s, yang hampir setara dengan rugi-rugi di tradisional material seperti silikon. Namun, sebagaimana silikon keberadaan

kristal batas yang sangat tidak jelas ini mampu mengisolasi material, dan menghasilkan emisi cahaya yang lebih lama, dan mobilitas muatan listrik yang lebih jauh. Hasil dari penelitian ini menjawab semua misteri yang pernah ada sejauh ini tentang emisi cahaya yang begitu lama yang kaitannya dengan sel surya berefisiensi tinggi dari material ini, walaupun ukuran kristalnya begitu kecil. Penelitian ini memberi panduan jelas bagaimana membuat material ini lebih baik lagi.

Pada Bab 5 kami menggunakan pengetahuan yang telah kami dapat sejauh ini untuk mendesain jenis arsitektur baru untuk sel surya. Arsitektur ini kami namakan sel surya dengan semua colokan dibelakan bersekala nano. Kami menggabungkan teori optik dan elektronik untukm memodelkan, dan mengoptimalkan arsitektur ini pada jenis sel surya perovskait-silikon berpermukaan datar, dengan menekankan pada peran colokan belakang berskala nano. Peran colokan nano ini adalah untuk mengurangi kriteria pengggunaan material murni. Terlebih desain kami mampu menghilangkan halangan yang ada pada desain yang ada sekarang (2-colokan atau 4-colokan). Faktor penting yang membuat desain ini menarik adalah permukaan atasnya yang kosong bisa dimanfaatkan untuk desain permukaan struktur penangkap cahaya, strategi pengisolasian permukaan, dan pelepasan emisi cahaya keluar permukaan.

Acknowledgements

During my sojourn in Holland, AMOLF has been the place providing helpful scientific exercises to raise myself to another level (you call it a PhD program). This section is dedicated to those who have helped me along that way.

My first thanks go to my advisor Erik Garnett. At the beginning I had little idea of what the group was really about, and I faced a hard time understanding his scientific approach. Nevertheless, he was still patient enough, both scientifically and personally, to bring me into sync. I have enjoyed the way he challenges me with problems: although to me it sounds noisy at first, it becomes clear at the end. I now realize after thinking about them very carefully, that in some cases the challenges were very visionary. The most important skill I learned from him is how to identify goals that are clear, important, and worth trying, and also how to demonstrate them in a convincing way. This is an important aspect that I will always carry in my future career. Therefore, I am truly honored.

Albert Polman, he is not only my PhD (co-)promotor, but also an inspiring leader connecting me with networks around him. Perhaps I only spent 1 % of my time during my PhD with him, but I find that this 1 % time has turned out to be productive experiences. One example is his sudden notification asking me to give a talk on the "COMPASS" project meeting. I found it overwhelming but at the end very useful sharpening my awareness of more details regarding surface passivation in Si PVs that eventually brought me in touch with some leading figures on this field in the Netherlands. I also thank for his help rectifying my Dutch summary, as well as what he provides for my future career.

I thank Prof. Rene Janssen, Prof. Jan Anton Koster, Prof Mark Golden, Prof. Wim Sinke, and Dr. Rene Williams for their time reading through my thesis draft carefully, providing comments for improvements, and serving as my committee members.

Members of the Nanoscale solar cell group: Jenny, Harshal, Biplab, Marc, Sven, Hongyu, Niels, Julia, and Forrest, I enjoyed your daily companion, and I am certainly going to miss this routine. Also the past members of the group, Sarah, Eric, Jia, Lai-Hung, Parisa, Haralds, Teo, Tade, and Shanti, thanks for sharing with me your similar mutual research interests. In particular to Sarah Brittman, and Eric Johlin, my extensive discussions with you were always very stimulating and helpful.

All AMOLF nanophotonics group members, especially the group leaders (Femius, Ewold, Bruno, Esther, and recently Said) who provided very useful and relevant questions to me over the last 4 years during colloquia, and poster seasons. In particular to Bruno Ehrler who consistently served as internal reviewer for my published works. Also members who are kind enough to provide direct help for my research: Sophie Meuret, and Nick Schilder for CL experiments, Benjamin Daiber, and Stefan Tabernig for troubleshooting bugs during my wide-field experiment, Jumin Lee for all detailed tips and tricks for material evaporation, Mark Aarts for AFM testing, Kevin Cognee for translating RCWA codes, Juha Muhonen for quite a discussion on measuring spin-diffusion. I have been pleased to share my research experience with Moritz Futscher, Lucie McGovern, and Loreta Muscarella on controlling perovskite grain sizes, David van der Flier for preparing samples for polariton lasing, and Jose Ocana for the CVD system. I was also supported in a friendly manner by amazing people from the nanoLab: Hans Zeijlemaker, Andries Lof, Dimitry Lamers, and Bob Drent on many projects. I also enjoyed the collaboration work with almost everyone in Wim Noorduin's group: Hans, Lukas, Iarik, and my superb paranymph Arno. In particular the work on converting their minerals into halide-perovskites using the CVD system - I am glad that it works, and has become a standard routine. I should thank many current (past) members in Huib Bakker's group who were being helpful during my first year adaptation, especially Simona, Liyuan, Konrad, Biplab, Niklas, Artem, and also Johannes, Reinout for helping me with the XPS measurement.

I would not be able to stay focused on my research without the help from our supporting staff. The HR team: Wouter, Roos, Valeska, and Reshma for securing all of my legal documents for working in Holland. The communication department: Grace, Petra, and Floortje for all of your encouragement to have fun during AMOLF events. The Inkoop department: Andre, Tatiana, and Angela for fast helps delivering/receiving my important samples. The financial team: Arnelli, and Sebastiaan for always being patient to guide me over and over again for through many mistakes I made filling out forms for my business trips. The Mechanical design team: Illiya, Henk-Jan, Marnix, and Ricardo, thanks for your help with all details designing in my setup and other drawings. The ICT team: Carl, Rutger, and my fav-friendly person Wiebe for all helps troubleshooting my PC/network/software licences. The electronic departement: I thank Jan Zomerdijk, Luc Blom, and Erik Clay for helping me to develop the SSPG setup. From the mechanical workshop department: I thank Jan van der Linden, Ricardo, Niels, Mark, and the specially friendly Tom Brouwer. The facility team: Clyde, and Karim for ensuring my office is comfortable enough all the time. Special thank to Silvia de Jong who amazingly managed to find every text book I requested to be available.

I also thank people outside of AMOLF, within the Netherlands and abroad, with whom I collaborated. From TU Eindhoven: Pim Veldhuizen, Yinghuan Kuang, and Dibya Koushik for tremendous help during my early years of the PhD. Pim introduced me to the SSPG world for the first time, something that fascinated me immediately and ever since. Yinghuan introduced me to the ALD method and magic recipes on it. Dibya helped me with fabricating the first solar cell device. From TU Delft: Ibadillah Digdaya, Bartek Trzesniewski, and Wilson Smith who consistently made my Friday

time extremely busy fabricating MIS samples for their water-splitting projects. I noticed that Digdaya has truly grown as scientist, and thanks for asking me a bunch of critical questions that surely deepened my understanding of silicon interfaces. From ECN: Piero Spinelli, and Paula Bronsveld who provide help and brainstorming ideas on fabricating the nanoscale back-contact tandem devices. From Maastricht University: Joel Keelor, and Sean Ellis for their help with mass-spec analysis of my samples, and I am happy that our frustration on the unexpected bad results turned out to be a supporting point in our other findings. From UC San Diego: Xueying Li, and David Fenning who provided helps with the nano-XRD on my samples, and confirmed the amorphous nature of grain boundaries. David thanks for your constructive questions on my analysis that I think hardly anyone could catch. From Washington University: Sarthak Jariwala, and David Ginger for an exciting proposal project on measuring carrier diffusion across different grain orientations. From Georgia Tech (USA) together with CSIRO (Australia): Giovanni DeLuca, Qicheng, Anthony Chesman, and Udo Bach on the theory project of microscale/hexagonal back-contact perovskite solar cells. I thank you for all of these encouraging and positive environments allowing me to really enrich my (limited) horizons across many disciplines.

My presence at AMOLF would not be possible without personal encouragement, and recommendations from my previous scientific mentors. In that regard, I thank Brian Yuliarto, Jeungku Kang, Jung-Yong Lee, and Omar Yaghi who have inspired me in their own ways.

I thank many Indonesian friends in Holland for their, somehow good, distraction which helped me to relax a little bit. I will spill out your names on other occasions, and thanks that I was having fun. Also my football teammates who really forced me to stay healthy even in snowy weather. I am going to miss you all!

I personally would dedicate this thesis to my late grandpa(s) who (to me) were truly great scholars and inspired me to be the one. Next to them, also my grandma(s) who keep reminding me of being genuine. Ayu, thank you for your patience and love. On top of everything, the spirit in this thesis always belongs to my Bapak, Ibu, and Indra.

Scientific portfolio

This thesis is based on the following publications:

1. *The expanding world of hybrid perovskites: materials properties and emerging applications*. S. Brittman, G.W.P. Adhyaksa, and E.C. Garnett. MRS Communications **5**, 7-26 (2015). (**Chapter 1**)

2. *Carrier diffusion lengths in hybrid perovskites: processing, composition, aging, and surface passivation*. G.W.P. Adhyaksa, L.W. Veldhuizen, Y. Kuang, S. Brittman, R.E.I. Schropp, and E.C. Garnett. Chemistry of Materials **28**, 5259-5263 (2016). (**Chapter 2**)

3. *Understanding detrimental and beneficial grain boundary effects in halide perovskites*. G.W.P. Adhyaksa, S. Brittman, H. Abolins, A. Lof, X. Li, J.D. Keelor, Y. Luo, T. Duevski, S.R. Ellis, D.P. Fenning, and E.C. Garnett. under review (2018). (**Chapter 3 and 4**)

4. *Nanoscale back contact perovskite solar cell design for improved tandem efficiency*. G.W.P. Adhyaksa, E. Johlin, and E.C. Garnett. Nano letters **17**, 5206-5212 (2017). (**Chapter 5**)

Patent applications:

1. *Multi-junction back contacts solar cell*. E.C. Garnett, G.W.P. Adhyaksa, and L.J. Geerligs. EU Patent Application P6062079NL (2017).

2. *Method for fabricating an efficient bio-photovoltaic*. J.K. Kang, G.W.P. Adhyaksa, D.K. Lee, I.W. Ock. US Patent 9293265 B1 (2016).

Other publications by the author:

1. *Anisotropic carrier diffusion across different grain orientations in lead-iodide perovskites*. S. Jariwala, D.W. deQuilettes, G.W.P. Adhyaksa, J.T. Wang, H.J. Snaith, E.C. Garnett, and D.S. Ginger. in prep (2018).

2. *Transparent quasi-interdigitated electrodes for back-contact solar cells*. G. DeLuca, A.N. Jumabekov, G.W.P. Adhyaksa, A.N. Simonov, J. Lu, B. Tan, E.C. Garnett, U. Bach, E. Reichmanis, and A.S.R. Chesman. submitted (2018).

3. *Converting rationally designed mineral architectures into semiconductors*. T. Holtus, L. Helmbrecht, H.C. Hendrikse, I. Baglai, S. Meuret, G.W.P. Adhyaksa, E.C. Garnett, and W.L. Noorduin. Nature Chemistry, accepted (2018).

4. *General considerations for improving photovoltage in metal-insulator-semiconductor photoanodes*. I.A. Digdaya, B.J. Trzesniewski, G.W.P. Adhyaksa, E.C. Garnett, and W.A. Smith. J.Phys. Chem. C. **9**, 17-36 (2018).

5. *Interfacial engineering of metal-insulator-semiconductor junctions for efficient and stable photoelectrochemical water oxidation*. I.A. Digdaya, G.W.P. Adhyaksa, B.J. Trzesniewski, E.C. Garnett, and W.A. Smith. Nature Communication. **8**, 15968 (2017).

6. *Benchmarking photoactive thin-film materials using a laser-induced steady-state photocarrier grating*. L.W. Veldhuizen, G.W.P. Adhyaksa, M. Theelen, E.C. Garnett, R.E.I. Schropp. Progress in Photovoltaics: Research and Application. **25**, 605-613 (2017).

7. *Engineering the kinetics and interfacial energetics of Ni/Ni-Mo catalyzed amorphous silicon carbide photocathodes in alkaline media*. I.A. Digdaya, P.P. Rodriguez, M. Ma, G.W.P. Adhyaksa, E.C. Garnett, A.H.M. Smets, W.A. Smith. J. Mater. Chem. A **4**, 6842-6852 (2016).

8. *A light harvesting antenna using natural extract graminoids coupled with plasmonic metal nanoparticles for bio-photovoltaic cells*. G.W.P. Adhyaksa, E.C. Prima, D.K. Lee, I. Ock, S. Yatman, B. Yuliarto, J.K. Kang. Advanced Energy Materials **4**, 18 (2014).

9. *Coupled near-and far-field scattering in silver nanoparticles for high-efficiency, stable, and thin plasmonic dye sensitized solar cells*. G.W.P. Adhyaksa, S.W. Baek, G.I. Lee, D.K. Lee, J-Y. Lee, J.K. Kang. ChemSusChem. **7**, 9 (2014).

10. *Broadband energy transfer to sensitizing dyes by mobile quantum dot mediators in solar cells*. G.W.P. Adhyaksa, G.I. Lee, S.W. Baek, J-Y. Lee, J.K. Kang. Scientifc Reports **3**, 2711 (2013).

Image galery:

1. self-assembly "*Perovskite heart template*" with plasmonic nanoparticles (2014)*.

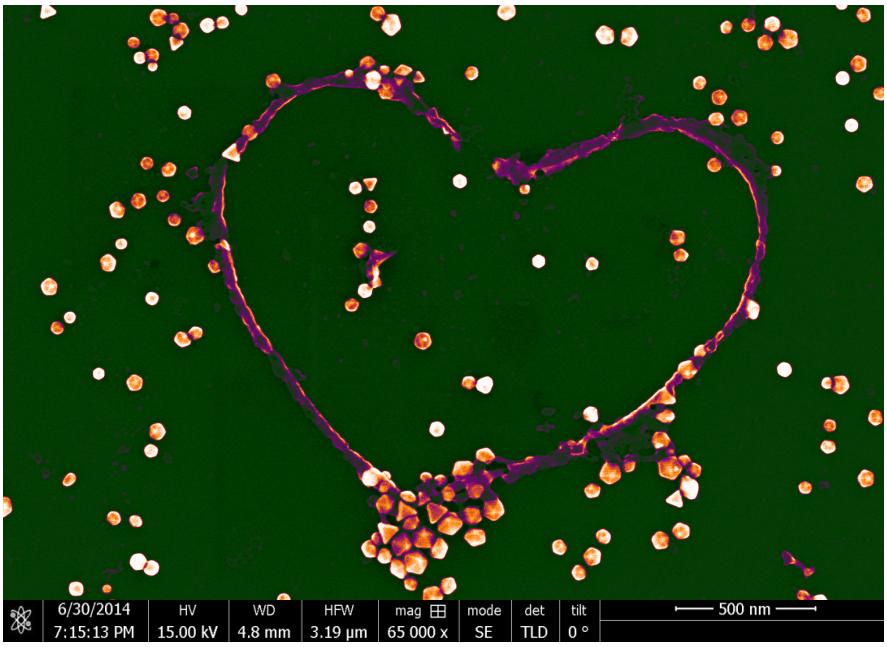

2. Plasmonic-perovskite core-shell nanowire (2014)*.

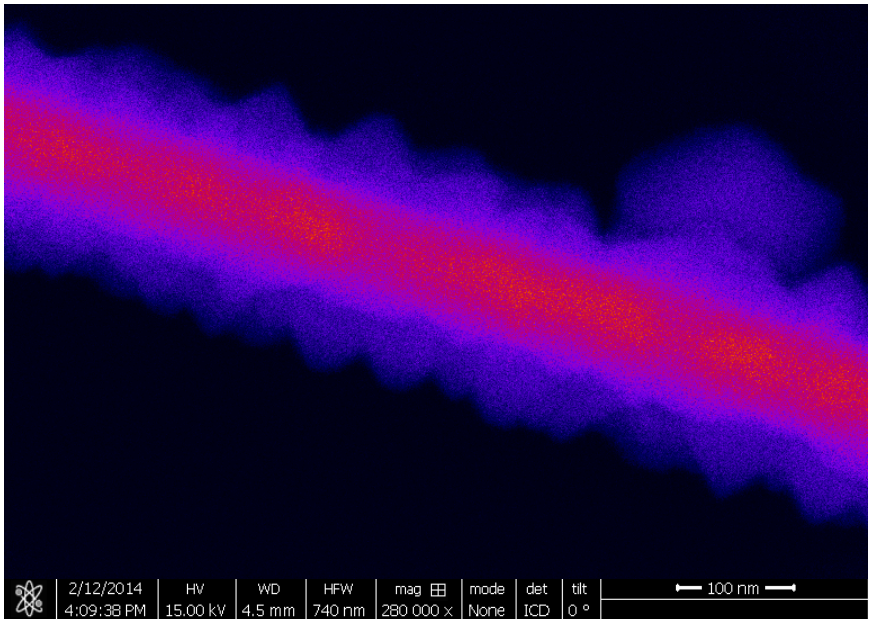

3. Vacancy defect inducing triple-plane boundaries in a hexagonal close packed structure (2015)*.

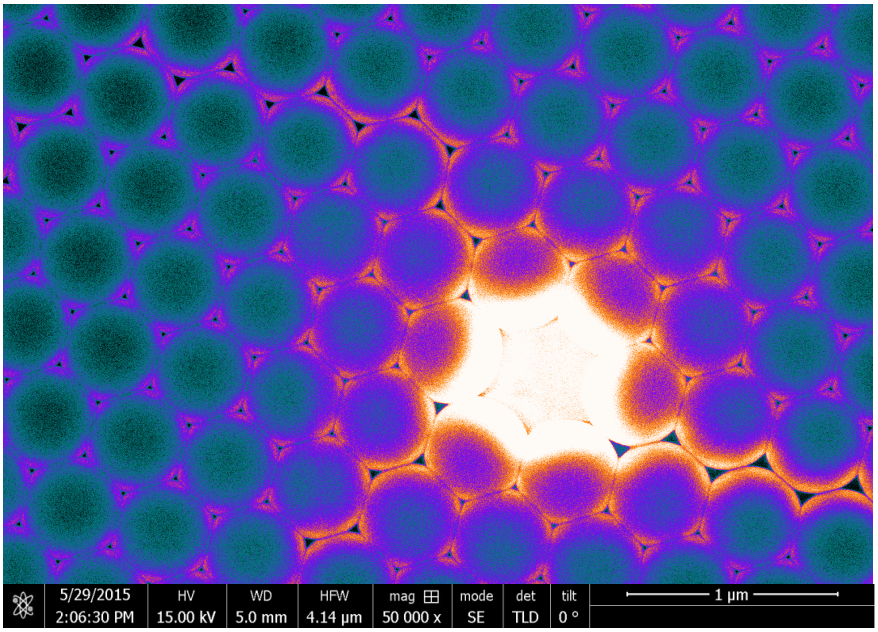

4. Selective area growth of perovskite crystals on "AMOLF" gold marker (2016).

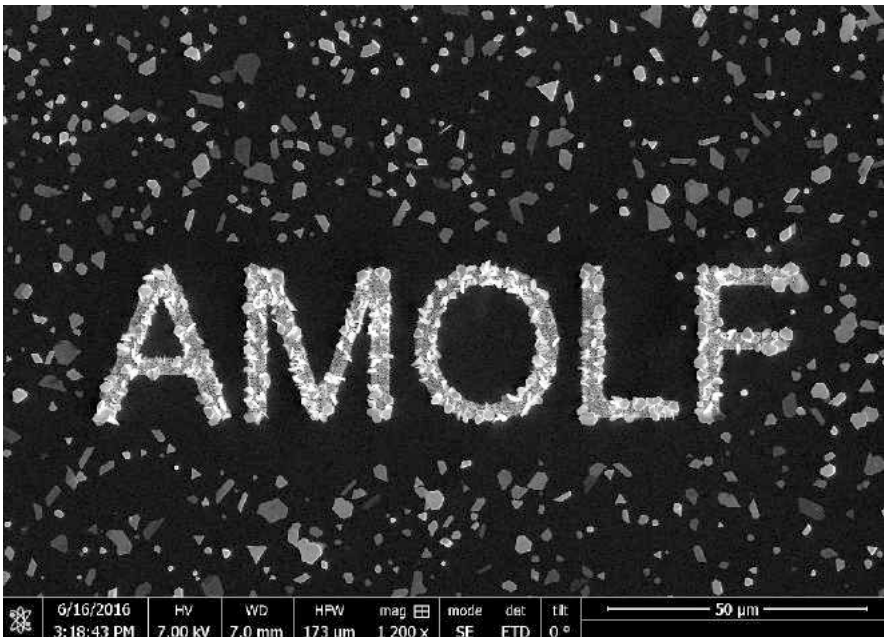

5. Cubic perovskites (2014)*.

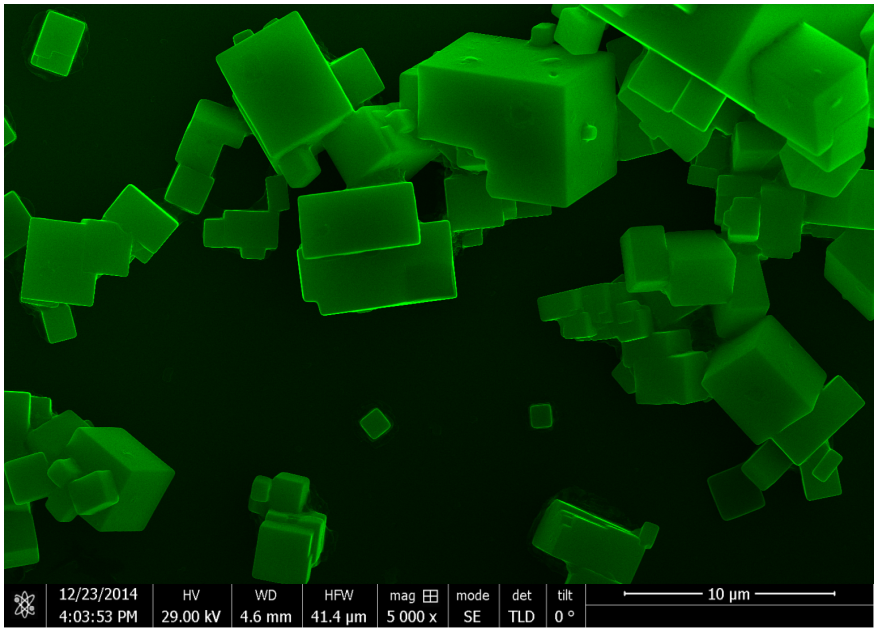

*false color image

About the author

Gede Adhyaksa was born in the island of Bali, Indonesia, on August 1, 1986. He studied Engineering Physics at Institut Teknologi Bandung in West Java, and graduated *Cum laude* (2008). Before starting his PhD at AMOLF (2014), during his master programs, he studied Engineering Physics at Technical University of Munich, Germany (2010), and Materials Science at Korea Advanced Institute of Science and Technology, Republic of Korea (2013). His research experience at AMOLF is presented in this book.

Besides research, he enjoys playing football, piano, traveling to unknown territories, and crafting aquatic plants at home.